Properties of Lightweight Fibrous Materials made using a Foam-Forming Technique

Steven Burke

School of Physics

Trinity College Dublin

A thesis submitted for the degree of

Doctor of Philosophy

March 10, 2021

Declaration

I declare that this thesis has not been submitted as an exercise for a degree at this or any other university and it is entirely my own work. I agree to deposit this thesis in the University's open access institutional repository or allow the Library to do so on my behalf, subject to Irish Copyright Legislation and Trinity College Library conditions of use and acknowledgement.

Steven Burke

Steven Burke .....

Acknowledgements

I would like to extend my gratitude and thanks to my supervisors; Stefan Hutzler and Matthias Möbius for providing guidance and support throughout the last four years and particularly for having faith in me and agreeing to take me on as a PhD student in the Foams and Complex Systems Group. I benefitted enormously by being involved with such a high-calibre group of individuals with diverse skills, experience and backgrounds.

I would also like to thank Jukka Ketoja and Tuomo Hjelt in the VTT Technical Research Centre of Finland, who kindly hosted me on several visits to VTT as well as collaborating with me on papers and providing support on a number of projects. They were always willing to help with any of my questions. My thanks also to Professor Denis Weaire, who regularly provided me with frank and useful commentary at our weekly group meetings.

It was a pleasure working with all the PhD students in the group, Gavin, Rob, David, Fritz, Jens, John, Ali and Jennifer, as well as all the undergraduate students who joined the Group to undertake fourth year projects, summer work and placement work. Thanks to DIT students Anthony Quinn and Sinead Lundberg for their help on a number of experimental projects. I particularly would like to say thank you to Fritz, for the laughs as well as the answers to numerous questions on science and life. A big thank you to the post-doctorate of the group, Benjamin Haffner. The research trips would not have been as exhilarating without you: minus 21 degrees, 01:00 and waiting for the hotel to let us in and you were still able to make me laugh! I nearly

died that night from frostbite. It was a pleasure working with you and thanks for the feedback on this thesis.

I also want to say thank you to two of this man's best friends whom I lost during my time in Trinity, Finn and Rosey. Thank you for the comfort, loyalty, entertainment and companionship you both provided to me over the years. I could not have asked for better, miss you both enormously. Hopefully we can go running through the forests of Valhalla when we next meet. My time at Trinity was cut short due to the lockdown arising from Covid-19. In early 2020, I was in the initial stages of a collaborative project with Professor Richard Duckworth of the Trinity School of Music. I enjoyed our discussions and it was a pity that we could not carry out the experimental work as planned.

I would also like to thank my parents and siblings for all their support over the last number of years. You were right Mam, I did enjoy it!

It goes without saying that I thank my wife, Roma, for all her support over the last number of years. Her theoretical physics background has kept me on my toes, I will always remember the oranges. There is no way I could have ever done this without you. Thank you for everything, I truly am a lucky man, love you forever. My beautiful little girl, Suki came along in my final year, just as the College went into lockdown. I got to spend a lot of time with her, although sometimes she just didn't seem to care that I was working on my thesis! She made all the hard work seem much easier. I dedicate this thesis to both my beautiful wife and beautiful daughter.

Summary

This thesis concerns the production and characterisation of foam-formed fibrous materials made from wood, peat fibres and spent grain. Such materials might find commercial applications for insulating purposes when produced at low density, or replace cardboard when produced at higher densities. The materials are produced by axially shearing a fibre-laden aqueous solution to which a surfactant has been added. The dispersion is then poured into a drainage vessel, where the liquid drains via gravity resulting in a lightweight fibrous sample.

The addition of fibres to an aqueous foam changes its properties. By adding fibres, a foam's lifetime can be greatly extended. Furthermore, the fibres place an upper limit on the average bubble size by arresting bubble growth during coarsening.

The influence of fibre concentration and liquid content of a foam-fibre dispersion is explored. We report a minimum fibre concentration required for sample stability. We show how both fibre concentration and the liquid content of the dispersion affects sample density. Uniaxial compression testing shows that the compressive modulus scales linearly with sample density. The liquid content of the dispersion can also be used to tune the sample compressive strength, when compressed in all three axial directions. The compressive modulus is increased by a factor of up to seven, just by changing the liquid content of the dispersion from 25% to 50% (with no change to sample density). The higher the sample density, the larger the range over which we can vary the compressive strength through the liquid content.

The role of liquid drainage is explored by comparing samples made using dispersions with the same volume of liquid, but varying the drainage rate. We find that the rate of liquid drainage has a larger impact on the compressive strength than the volume of liquid.

We image our samples using μCT scanning and relate the fibre orientation distributions to both the compressive strength of the material and the liquid content of the dispersions. Void size is shown to be similar to the average bubble size of the dispersion from which it was produced.

Our samples display an anisotropic response to uniaxial compression when compressed in different directions. We attribute this behaviour to a layering of fibres that occurs during sample production. Increasing the liquid content of the dispersion increases the number of fibres which orientate out of these layers, changing the material's compressive strength. Using Euler's formula for buckling we propose an explanation for the observed stress-strain response.

We present a case study in which we use the foam-forming technique to create beer coasters from brewers spent grain. We probe our samples for the key requirements of commercial beer coasters, such as the rate of liquid absorption, quantity of liquid absorbed and tensile strength. The experiments show that the spent grain coasters absorb liquid at a faster rate and absorb more liquid during a fixed period of time than the commercial coasters.

We conclude our results and, focusing on a theme in which we encourage industry to replace non-sustainable materials with foam-formed fibrous alternatives, we identify and propose a direction for the continuation of the project to further explore and improve typical key material requirements. Experiments on compressive strength, recovery and thermal conductivity are proposed. We also set out the preliminary results of an experiment to measure bubble size from the vibrational response emitted as it ruptures. This is a non-invasive method to measure coarsening and may be useful in an industrial setting.

List of publications

The list of publications has eminated from the research carried out in this thesis. The first two manuscripts listed have been peer reviewed and published. The third manuscript is currently under review with Springer journal SN Applied Sciences.

1. B. Haffner et al., *Ageing of fibre-laden aqueous foams*, Cellulose **24**, 231–239 (2016)

2. S. Burke et al., *Properties of lightweight fibrous structures made by a novel foam forming technique*, Cellulose. **26**, 2529–2539 (2019)

3. S. Burke et al., *Analysis of the foam-forming of non-woven lightweight fibrous materials using x-ray tomography*, SN Applied Sciences **192**, 10.1007/s42452-021-04172-9 (2021)

In addition the author contributed to following publication.

- A. Mughal et al., *Demonstration and interpretation of 'scutoid' cells formed in a quasi-2d soap froth*, Philosophical Magazine Letters **98**, 358–364 (2018)

Contents

Chapter 1

Foam-Forming and Lightweight Materials

"We are at a unique stage in our history.
Never before have we had such an awareness of what we are doing to the planet.
Surely we all have a responsibility to care for our Blue Planet.
The future of humanity and indeed, all life on earth,
now depends on us."

-Sir David Attenborough [5]

1.1 Introduction and Background

There has been a global shift towards using sustainable materials as well as developing more environmentally friendly production methods. For instance, Carlsberg, in collaboration with researchers from the Technical University of Denmark, recently unveiled what they claim is the first beer bottle made of sustainable and recyclable wood fibres (see figure 1.1). It is part of an initiative by Carlsberg to reach zero carbon emissions and a 30% reduction in its overall carbon footprint by 2030 [6].

While on the subject of beer, images of turtles, birds and fish trapped in plastic rings traditionally used to hold beer cans together is often portrayed in

Fig 1.1: Top left: Plant-based six-pack ring developed by Cerveceria Modelo to replace plastic beer can holders. Bottom left: A similar product developed by Saltwater Brewery made of brewers spent grain, a by-product of the brewing process. Right: A bottle made of wood fibres developed by Carlsberg as part of their pledge to reduce their carbon emissions. Image sources: [7–9]

the media. Saltwater Brewery in Florida has tackled this problem by creating a six-pack ring made of spent grains from the brewing process, which they claim is 100% biodegradable and can even be consumed by marine wildlife.

Encouraging industry to replace non-sustainable materials with renewable or recyclable alternatives is not always an easy task. To shift the focus to sustainability, several factors need to be taken into consideration such as the material's performance as well as the costs of production and of the raw materials themselves. The sustainable alternative should perform the same or better than its non-sustainable counterpart and meet relevant industry standards. Costs should ideally be equal to or less than that of the material it is replacing, thus incentivising its production.

Fig 1.2: A selection of sheet-like materials made using recycled and recyclable fibres by way of the foam-forming technique. The top left picture shows insulating coffee cup wraps, designed to keep the hand cool when holding a hot beverage. The wrap on the left was made with peat fibres, while the one on the right was made with brewers spent grain. The bottom left picture shows a beer mat (drinks coaster) prototype also made of brewers spent grain. On the right is a moulded funnel, designed to show how other structures can be made from foam-formed fibrous sheets. All the materials in the above picture were made as part of this PhD project in our laboratory in Trinity College, Dublin.

Foam-forming can be used to develop materials made of recyclable or renewable fibres such as wood fibres, brewers spent grain and peat (see figure 1.2). The technique was originally developed to produce paper sheets due to foam's ability to disperse both fibres and particles in suspension with less flocculation occurring than in water-borne methods [10]. Foam-forming uses less water than traditional paper-making methods, the air content of the foams being $\approx 50\%$, leading to a reduction in the energy costs to de-water and dry the foam-formed paper.

Dispersal of the fibres in a foam is usually achieved through axial shearing.

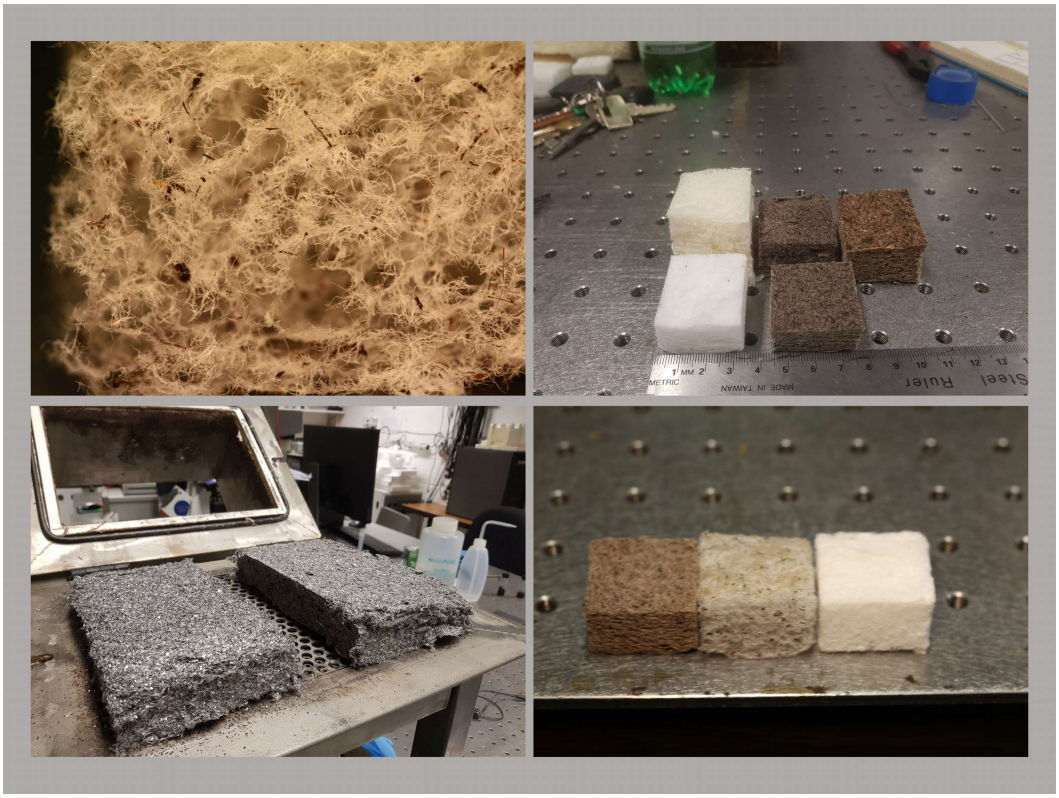

Fig 1.3: A selection of lightweight materials made by foam-forming. The top left picture shows a lightweight fibrous material made of a mixture of Kraft (a type of cellulose based fibre) and peat fibres (partially decayed vegetation). The sample contains no bonding agents. The bottom left picture shows two samples made of Kraft fibres, impregnated with graphene flakes. The lightweight materials shown in the top and bottom right pictures are all made from recycled and recyclable fibres including peat, brewers spent grain, Kraft and CTMP fibres.

The fibre-laden foam dispersion (referred to as a foam-fibre dispersion in this thesis) is then poured into a drainage vessel, where the liquid is extracted through a fine gauze base. When a vacuum is applied to the underside of the vessel, the result is a flat dense fibrous sheet left on the gauze. With no vacuum, the technique can be adapted to produce lightweight low-density highly porous materials (see figure 1.3).

The majority of the research carried out in the area of foam-forming has focused on the production and improvement of dense fibrous sheets [11–13].

Over the last number of years, research has started to shift focus to lightweight, low-density fibrous materials also produced by foam-forming [2, 14–16]. The existing research on lightweight fibrous materials has primarily dealt with the material properties and how they can be altered through the use of additives and modifications to the fibres, making them better suited to particular applications.

This thesis contributes to the existing research on lightweight fibrous materials by considering the influence of the properties of the foam in which the fibres are initially dispersed and in particular, the effect of the liquid content of the foam on the mechanical properties of the resulting fibrous material.

The potential range of industry applications for foam-formed lightweight fibrous materials is extensive. Applications include insulation, protective packaging, filtration and absorption devices among others.

Insulation and protective packaging: Within the insulating and protective packaging industries, petrochemically-derived materials such as expanded polystyrene, polyurethane and phenolic foam are in widespread use due to their thermal properties, high air content and compressibility. However, these materials are often made from non-sustainable resources and are not easily disposed of or recycled. Replacing these types of materials with renewable resources, may offer a better solution, provided we can match the relevant material properties and characteristics.

For a material to be effectively used for thermal insulation purposes, a primary consideration is its thermal conductivity value. While there have been only a few studies on the thermal properties of lightweight foam-formed fibrous materials, one study by Pöhler *et al.* made a comparison between several foam-formed low-density fibrous materials to that of commercially available insulation [17]. The study showed that foam-formed material made of cellulose fibres (Kraft) matched the thermal properties of commercially available glass wool insulation, for the same density of material.

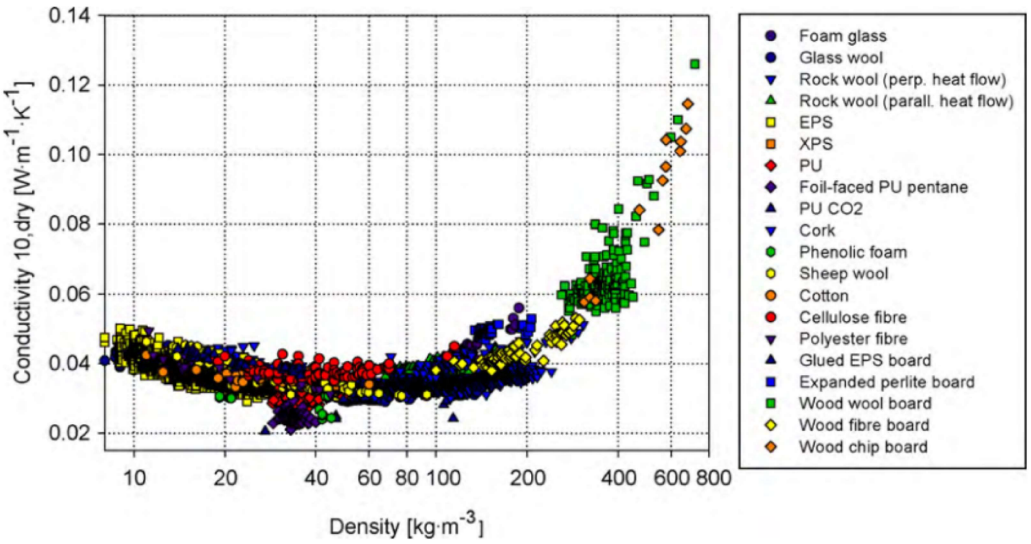

Fig 1.4: The above figure was published by Dominguez-Munoz *et al.* It shows the thermal conductivity as a function of sample density for a range of commercially available insulating materials. Two trends are apparent; at lower densities, thermal conductivity decreases with an increase in density. At higher densities, the conductivity increases with an increase in density.

Dominguez-Munoz *et al.* tested the thermal conductivity of a large range of commercially available insulating materials [18]. The materials included inorganic materials such as foamed glass, glass wool and rock wool, as well as organic-based materials such as polystyrene, polyurethane, sheep wool and cellulose fibres. The density of the material was found to greatly influence its thermal properties, with two distinct trends emerging (see figure 1.4). At low densities, the thermal conductivity of the material was observed to decrease with an increase in density. They attributed this to long-wave radiant exchange inside the pores. For higher densities, the opposite was observed; the thermal conductivity increased with an increase in material density, as the porosity of the material decreased.

The range of material densities studied in this thesis is in the lower density range (from 8 to $45 kg.m^{-3}$). Based on the work of Dominguez-Munoz *et al.*, the thermal conductivity of the material in this density range will decrease with an increase in sample density. Later we show how the liquid content and fibre concentration of the foam-fibre dispersion can be used to control sample density.

The thermal conductivity of a fibrous material is also influenced by its pore or void size [19]. Therefore, if we can vary the void size or the orientation of the voids within the material, we may be able to influence its thermal conductivity value.

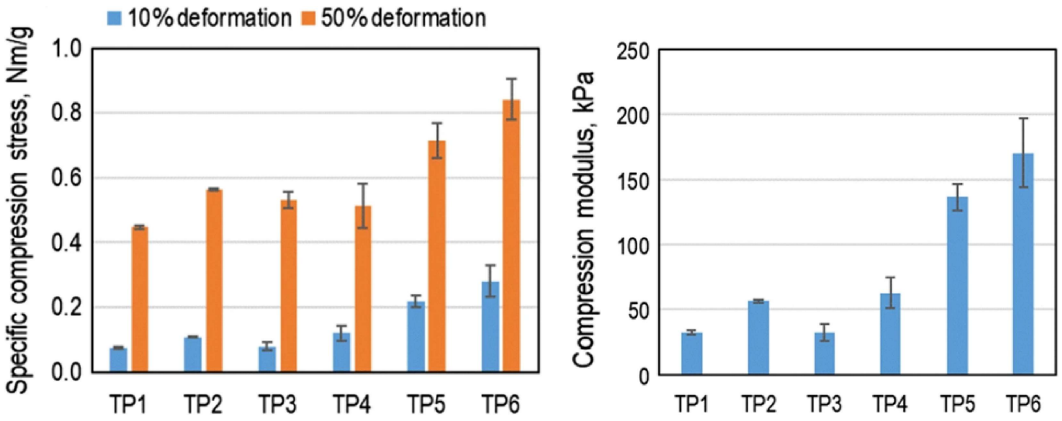

Fig 1.5: The compression strength of a range of materials made from natural fibres with the addition of the bonding agent Polyvinyl Alcohol (PVA). The work was carried out by Pöhler *et al.* The figure on the left shows the ratio of specific compression stress divided by sample density for a range of samples. The figure on the right shows the compressive moduli of the same samples. Sample TP5 contained bleached Kraft fibres with PVA. TP6 contained Kraft fibres, hemp fibres and PVA.

The material's compressive modulus is also important. For example, for a foam-formed material to be successfully used as wall insulation or as protective packaging, it must be able to withstand the impacts associated with its intended use. Pöhler *et al.* investigated the compressive strength of lightweight fibre networks and how they could be improved [20]. They made a number

of foam-formed fibre networks consisting of different types of natural cellulose fibres to which polymers, fibrils and fines were added during production (see figure 1.5). They reported a compressive modulus for a sample made of bleached Kraft fibres of 140kPa (TP5 in figure 1.5), when Polyvinyl Alcohol (PVA) was used as the foaming agent. By way of comparison, a typical compressive modulus for wall insulation is around 90kPa. Where a mixture of natural hemp and Kraft fibres (20:80 w/w) was used to form the network and PVA being the foaming agent, they achieved a sample compressive modulus of 170kPa (TP6). In this thesis we determine the compressive modulus of foam-formed materials without the addition of bonding agents such as polyvinyl acetate.

In addition to thermal and compressive properties, a material's ability to recover from deformation is important. For example, glass wool insulation (laid out between joists in roof spaces) is usually packaged by rolling a length of the material into a cylindrical shape and then unrolled during installation.

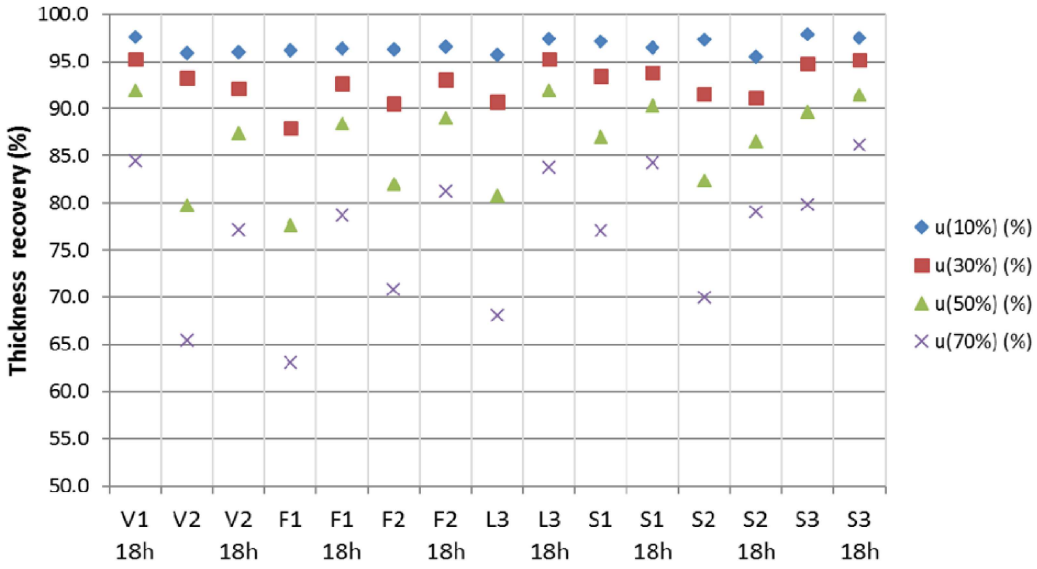

Fig 1.6: Creep recovery of a number of foam-formed low-density materials presented by Paunonen *et al.* The legend indicates the level of strain applied to the samples (10%, 30%, 50% and 70%) with a rest period of 18 hours between each test. The y-axis represents the % of recovery achieved by each sample. The x-axis represents the different composition of the samples (see [21] for further details). All of their samples contained a natural polymer to improve recovery after compression.

Paunonen *et al.* investigated the compression recovery of lightweight foam-formed fibrous materials made from Kraft fibres and how it could be improved. They added a natural polymer (rubber) to the dispersion and showed that it accumulated at the fibre-fibre intersections within the fibre network. Cyclical loading showed the samples to have a good recovery after the initial compression cycle (up to 97% creep recovery after 18 hours), with little hysteresis being displayed (see figure 1.6) [21].

In any industry, a material's fire retardancy rating will be important. This is particularly the case in the construction industry as all EU building products must meet the requirements as set out in the European Standard EN 13501 [22]. There have been several of studies showing that the flammability of wood fibres can be significantly reduced. One such study by Köklüikaya *et al.* showed extremely promising results [23]. They employed a layer-by-layer deposition technique to deposit thin films of cationic chitosan and vinyl phosphonic acid onto wood pulp fibres. Subsequent flame and flammability testing of the material demonstrated that not only did the thin film reduce the flammability of the fibres, it also self-extinguished the flame. The same technique could be used to treat the materials investigated in this thesis to improve upon their fire retardancy rating, as they too are made of wood pulp.

Filtration and absorption: Filtration and absorption are other areas in which foam-formed fibrous materials may offer novel alternatives to existing materials. Ottenhall *et al.* modified the surface of cellulose-based fibres enabling the absorption of harmful bacteria from water [24]. Their results showed that the modified fibres removed over 99% of the bacteria from non-turbid water. According to the authors, the fibre surface attracts the bacteria by forming bonds, thus trapping the bacteria on the fibres. Incorporating the modified fibres discussed by Ottenhall *et al.* into lightweight foam-formed materials could potentially allow for the filtration of bacteria from air as well as water.

There have also been several studies on the ability of natural fibres to absorb oil. Payne *et al.* showed that bleached softwood Kraft fibres absorb over six times their mass in crude oil [25], while, Cao *et al.* reported that fibre assemblies made from Kapok (a species of tree native to Africa) absorbed almost 26 times their own weight in oil [26]. Foam-formed fibrous materials could therefore play a useful role in the clean-up of crude oil spills and other areas where oil absorption is important.

1.2 Structure of the Thesis

In this thesis we create lightweight fibrous materials using the foam-forming technique. The foam-fibre dispersions are allowed to gravity drain (no vacuum applied) resulting in lightweight, highly porous, fibrous materials. The focus of the work presented here is to understand the fundamentals of the foam-forming technique, with particular emphasis placed on how the liquid content of the foam affects the material and mechanical properties of the resulting lightweight fibrous material. Our findings will enable us to incorporate the liquid fraction as a control parameter during the production process.

We begin in chapter 2 with an overview of aqueous foams, defining some of the key properties of foam that allow us to produce lightweight fibrous materials. We describe the method used to produce the foams as well as the method we use to obtain bubble size distributions.

In chapter 3 we set out the materials and methods used to produce low-density fibrous material. We discuss the composition of the fibres, their origin and how they are produced. We then explain how we make the lightweight material, setting out the steps of the foam-forming technique and the drying process.

Chapter 4 focuses on the properties of foam-fibre dispersions. We show how the fibres influence the typical coarsening behaviour and lifetime of a foam. Moreover, we identify the minimum concentration of fibres that will allow for a stable structure to be formed after the drainage and drying stages have concluded.

In chapter 5 we explore the material and mechanical properties of the foam-formed fibrous samples. We show how sample density scales with fibre concentration and the how liquid fraction of the dispersion used to create the material influences this scaling. The mechanical properties are investigated via uniaxial compression testing. We show that the initial liquid fraction of

the foam-fibre dispersion can be used to tune the compressive strength of the material, when compressed from all three axial directions.

Chapter 6 explores the relationship between the microstructure of the foam-fibre dispersions and the compressive strength of the resulting fibrous structures. We present image analysis results obtained by computed tomography scanning of several lightweight fibrous materials. Through fibre orientation distributions, obtained from the CT images, we relate the fibre orientation distributions to the material's compressive strength and show how the liquid fraction can be used as a control over the orientation distribution of the fibres.

In chapter 7 we present a case study where we produced an alternative to the traditional beer coaster made using brewers spent grain, a by-product of the brewing process. We compare some of the important properties of the foam-formed spent grain beer coaster to the traditional beer coaster, such as the rate at which the coaster absorbs water, the volume of water absorbed and its tensile strength.

In Chapter 8, we conclude our results and, focussing on a theme in which we replace non-sustainable materials with foam-formed fibrous alternatives, we identify and propose a direction for the continuation of the project to further explore and improve the key material requirements. The proposed direction includes: developing additional experiments to use the drainage rate as a control over compressive strength and researching the role of fibre length, fibre type and the addition of a biodegradable bonding agent on compressive strength. Lastly, we set out the preliminary results of the experiment discussed in Appendix A.

In Appendix A we demonstrate a new non-invasive technique developed to infer a bubble's size from its vibrational response, emitted during film rupture. We show how the technique can be used to monitor the coarsening of fibre-foams.

In Appendix B we present a set of experiments in which we used a bonding agent when making several different fibre type samples including fibres such as peat fibre, brewers spent grain and chemi-thermomechanical pulp fibres (CTMP). We show how the bonding agent polyvinyl acetate (PVA) can be used to increase the strength of the materials. We make a comparison between the materials made of different fibre types to that of samples made of purely Kraft fibres (no PVA).

Appendix C shows the workings of the fibre orientation analysis plugin OrientationJ. We show how the user settings can be used to filter "noise" from the images.

While the work carried out in this thesis may not save the planet, I sincerely hope that even in some small way it might contribute to a more sustainable way of producing materials from natural resources, ideally replacing petrochemically-derived products with more natural and sustainable ones.

Chapter 2

An Introduction to Aqueous Foams

In this chapter, we set out several methods that can be used to produce aqueous foams. We then define some of the key properties and characteristics such as structure, bubble size distributions and flow behaviour. This is important as later in the thesis, we take advantage of some of the key features of aqueous foams for the dispersal and transport of fibres, when producing low density fibrous materials.

2.1 Methods of Producing Aqueous Foams

An aqueous foam is a two-phase system, with gas dispersed as bubbles within a continuous liquid phase [27, 28]. There are many ways to produce an aqueous foam. For example, one may shake a bottle containing a small amount of surfactant solution or blow air through a narrow orifice submersed in a surfactant solution (bubbling). Flow focusing is a method commonly used to produce monodisperse bubbles. The continuous liquid phase is forced under pressure through a tube, inside which is a smaller capillary tube with a small orifice. The dispersed phase is injected through the capillary tube. As the gas exits

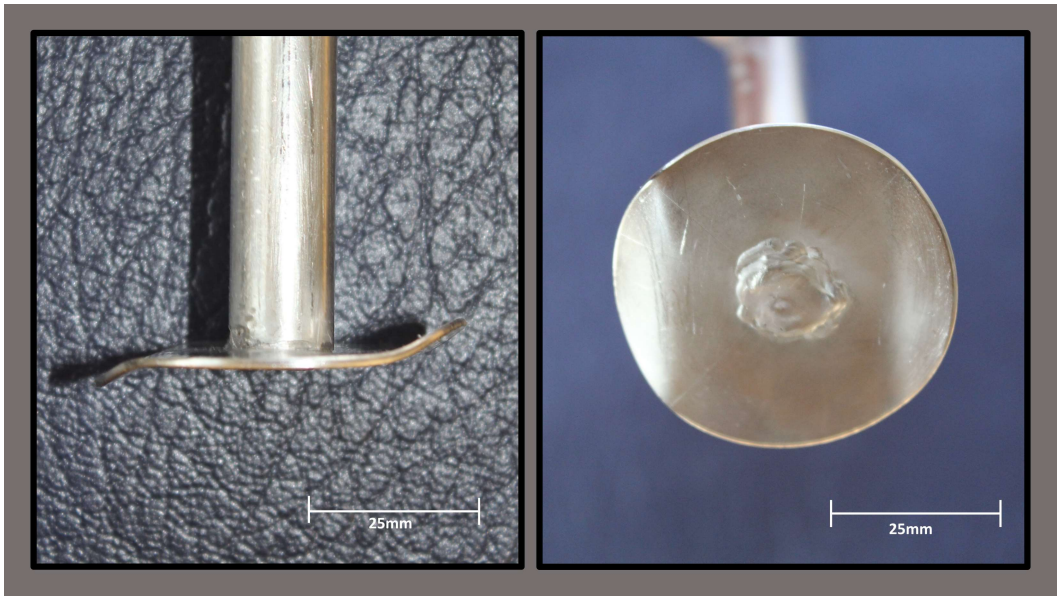

Fig 2.1: The mixing disk used to produce the aqueous foams discussed in this thesis. The image on the left shows the disk's two opposing 25^o bends, which entrains air into the aqueous solution by creating a turbulent flow thus producing foam of highly polydisperse bubbles. The image on the right shows a view of the disk from the underside.

the small orifice, capillary instability results in the dispersed phase breaking up, resulting in small homogeneous bubbles being formed. The bubble size and liquid fraction can be controlled via the flow rate and viscosity of the liquid. The range of bubble sizes produced by flow focusing is between 10μm and 1000μm [29].

Axial shearing is another method that can be used to produce an aqueous foam. The foam is created by rotating a mixing disk at a high rate of revolutions (typically between 3000 and 6000 revolutions per minute) in an aqueous solution. The design of the disk, which incorporates two opposing bends (see figure 2.1) creates a turbulent flow, allowing air to be entrained into the aqueous solution and produces a foam of highly polydisperse bubbles [30]. This method was used to produce the foams discussed in this thesis, as the turbulent flow created by axially shearing a surfactant solution also enables fibres to be randomly dispersed throughout the foam.

2.2 Foam Structure

2.2.1 Foam Stability

Foam stability relates to the lifetime of a foam, which may be characterised by several different measures. These include monitoring the volume of the foam, the total number of bubbles, or the height of a column of foam, as a function of time.

The viscosity of the continuous liquid phase, the pressure of the gas within the bubbles and ambient temperature are all factors which can influence the lifetime of a foam.

Foam stability is also dependent on the surface tension at the gas-liquid interfaces (the bubble films). Stability of a foam can be improved by adding surfactants [31], a type of molecule containing a hydrophobic tail and a hydrophilic head, meaning the surfactant molecules prefer to locate at gas-liquid interfaces. The forces of attraction between a surfactant molecule and a water molecule are less than that of water-water molecules thereby reducing surface tension [32].

When the concentration of surfactant is sufficiently high, there is insufficient free surface area available at the gas-liquid interfaces for the surfactant molecules to locate to and they form what are called micelles. Micelles are clusters of surfactant molecules in the bulk of the liquid. The molecules orientate with their tails toward the inside of the cluster and the polar heads toward the liquid [33]. The concentration at which micelles form is known as the critical micelle concentration (CMC).

When a liquid film is perturbed (such as by prodding or stretching), an imbalance in the film's surface tension is created. This is caused by the slow diffusion time of the surfactant molecules. It results in a gradient in the surface tension, with the thinner section of the film having a higher local surface tension. The gradient acts as a restoring force, causing the liquid

phase to flow from the areas of the film with a lower surface tension (thicker area of the film) to the area with a higher surface tension (thinner area), restoring the uniform surface tension and thickness of the film [34].

Having a surfactant concentration at or above the CMC ensures the gas-liquid interface has the lowest possible value of surface tension (for the particular surfactant), producing the most stable foam [35, 36]. The aqueous foams discussed in this thesis were all produced with surfactant concentrations well above the CMC.

2.2.2 Liquid Fraction

An important quantity for the characterisation of a foam is its liquid fraction, ϕ. This is a measure of the foam's liquid content. It is generally non-uniformly distributed throughout the foam and can also depend on time. In a column of foam, gravity-driven liquid drainage sets a vertical gradient in the liquid fraction profile; the gradient increases along the direction of gravity. The liquid fraction also reduces over time as the liquid drains from the foam. The liquid fraction of a column of foam can therefore generally be expressed as a function of vertical position and time, $\phi = \phi(z, t)$ [37].

A key parameter in this thesis is the initial liquid fraction ϕ_i of a foam immediately after its production using the mixing disk in figure 2.1. As mixing redistributes the liquid in the foam, we may approximate it as constant throughout the foam. Its value is given by the ratio of the volume of the liquid used for its production to the total volume of the foam.

$$\phi = \frac{\text{Volume of Liquid Phase}}{\text{Volume of Foam}} \tag{2.1}$$

The liquid fraction of a foam gives an indication to the overall shape of its bubbles. Foams having a liquid fraction of $\phi \geq 0.15$ are considered

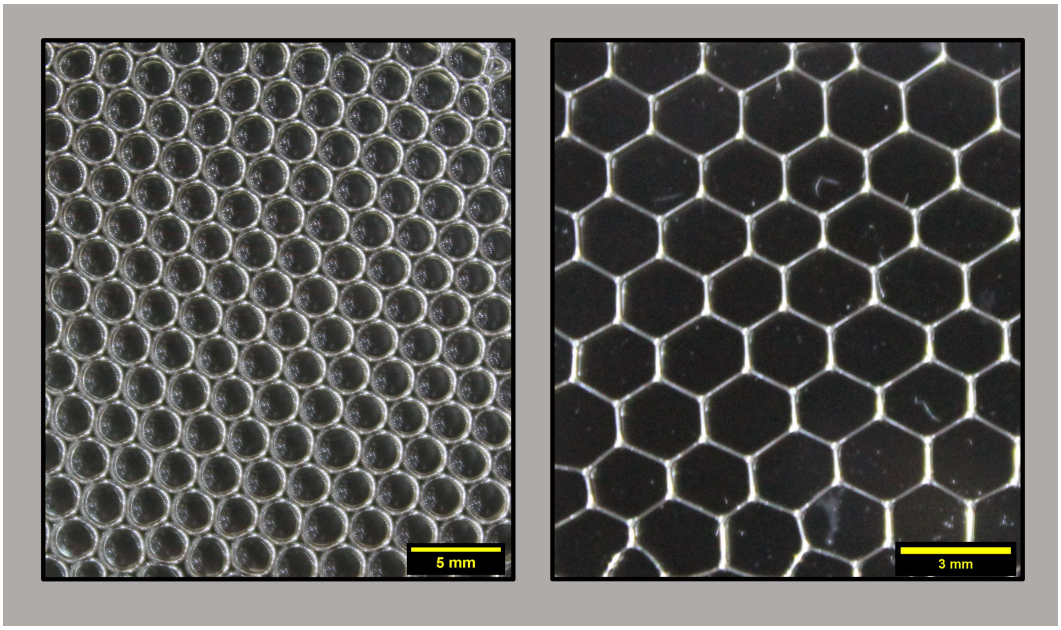

Fig 2.2: Samples of two aqueous foams placed between two microscope slides (spacing 1mm). The foams were made by bubbling an aqueous solution containing sodium dodecyl sulfate as the surfactant, resulting in equal volume bubbles. The foam on the left is a wet foam, as indicated by the almost circular bubbles. On the right is a dry foam with thin liquid films separating the bubbles, which display polygonal shapes.

"wet" foams. When $\phi \geq 0.36$, there is enough space within the foam for the bubbles to be near-spherical, as they are no longer confined by neighbouring bubbles [37]. In the dry limit bubbles are approximately polyhedral. The foams discussed in this thesis are wet foams with ϕ_i ranging from 0.25 to 0.50. Figure 2.2 shows different bubble shapes for quasi 2D foams, i.e foams confined between two plates.

2.2.3 Coarsening and Coalescence

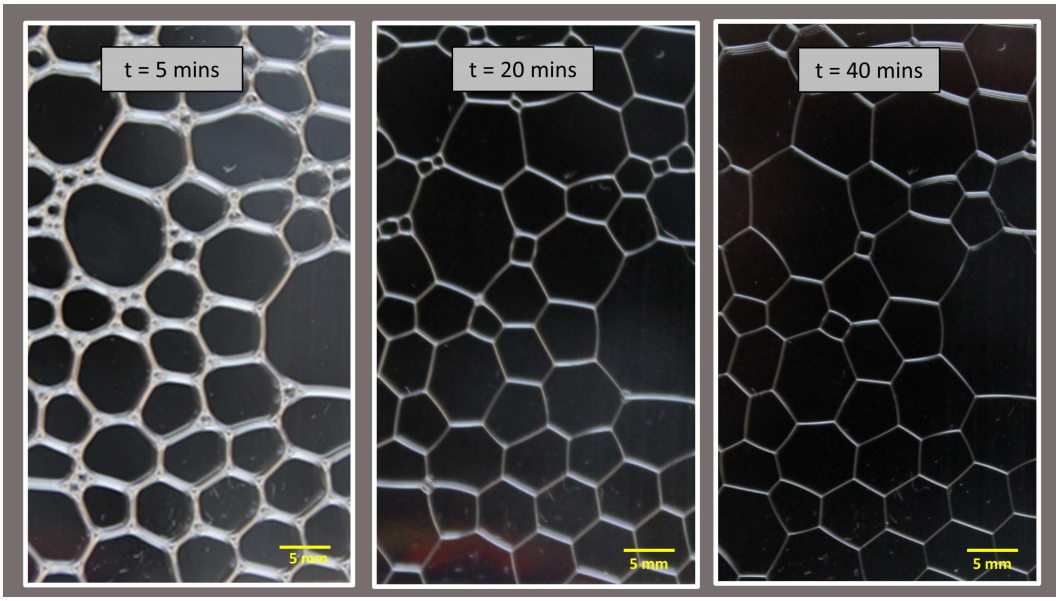

Fig 2.3: Coarsening and coalescence of a (quasi) 2D aqueous foam between two microscope slides. The bubbles transition from a wet foam (left image) to a dry foam (right image) by way of coarsening and coalescence. The films separating the bubbles become thinner with time as the foam dries. A number of the smaller bubbles disappear as the gas inside diffuses into the larger neighbouring bubbles (coarsening). The total number of bubbles is also reduced by the rupture of films between bubbles (coalescence).

The pressure difference ΔP across the gas-liquid interface of a bubble is given by the Young-Laplace equation [27, 38]:

$$\Delta P = \gamma \left(\frac{1}{R_1} + \frac{1}{R_2} \right) \tag{2.2}$$

R_1 and R_2 are the radii of curvature of the bubble's film. γ is the surface tension. In the case of a spherical gas bubble submerged in a liquid, there is one interface (gas-liquid) and $R_1 = R_2$. The Laplace pressure thus reduces to

$$\Delta P = \frac{2\gamma}{R} \tag{2.3}$$

Where a bubble is surrounded by a gas, there are two interfaces. One inside the bubble (gas-liquid) and one on the outside (liquid-gas). In this case, taking account of the two interfaces, the Young-Laplace equation becomes [27]:

$$\Delta P = \frac{4\gamma}{R} \tag{2.4}$$

Equation 2.4 tells us that smaller bubbles have a higher pressure. Coarsening is a dynamic process in which gas within the smaller, higher pressure bubbles, diffuses through the films into larger neighbouring bubbles. Thus, the number of bubbles within a foam decreases with time, while the average bubble size increases (see figure 2.3).

The rate at which coarsening occurs is dependent on several factors such as the solubility of the gas, the type of surfactant used and the liquid content of the foam [39–41]. Several studies have shown that the bubble growth of an aqueous foam is governed by an asymptotic scaling law [42–44]. The average bubble radius, $\bar{r}_b$, as a function of time t can be expressed as:

$$\bar{r}_b \propto (t - t_0)^{1/2} \tag{2.5}$$

As well as coarsening, another contributing factor to the reduction in the number of bubbles in a foam with time is the process of coalescence. Coalescence is the abrupt rupturing of the thin film between two adjacent bubbles, resulting in one larger bubble. It is a poorly understood phenomenon due to the difficulty in probing coalescence experimentally.

The diffusion time of the surfactant molecules is thought to play a role in coalescence. Ghosh and Juvekar derived a model describing the coalescence of a film between two bubbles in their 2002 study [46]. They showed that when two bubbles are brought into contact, the adjoining film has a thinner outer ring, with the centre of the film being the thickest part (see figure 2.4). When the bubbles are first brought into contact, the surfactant molecules accumulate at the outer ring and then begin to diffuse towards the centre of the film due to the surfactant concentration gradient. Fewer surfactant molecules in the ring results in the depletion of the repulsive forces. As the repulsive forces diminish the ring becomes thinner. Coalescence is brought on by the repulsive

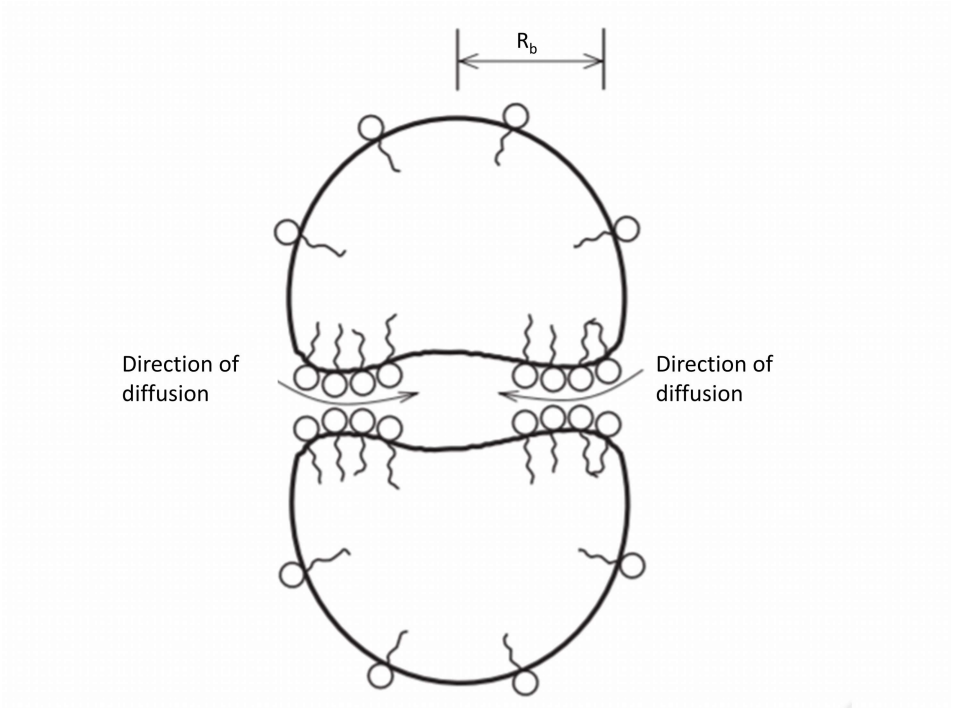

Fig 2.4: Schematic of surfactant molecules diffusing through a thin film separating two bubbles. The thickness of the adjoining film has been exaggerated for illustrative purposes. R_b is the bubble radius. Image source [45].

forces being less than the Van der Waals attraction between the two bubble surfaces resulting in the abrupt rupture of the film.

2.2.4 Gravity-Driven Drainage

One of the ways in which an aqueous foam ages is by the thinning of the liquid films, brought on by gravity-driven liquid drainage. In a very wet foam ($\phi \geq 0.36$) the bubbles are near spherical, separated by the liquid medium. As the liquid drains, the bubbles come closer to each other, leading to the formation of thin liquid films between them. In the dry limit, $\phi \rightarrow 0$, a foam may be described as a cellular structure. Three film edges meet together at 120^o, forming channels known as Plateau borders. The Plateau borders meet at intersections in groups of four separated by an angle of approximately

109^o. They form a continuous network throughout the foam structure, through which further drainage occurs (see figure 2.5). The relationship between the

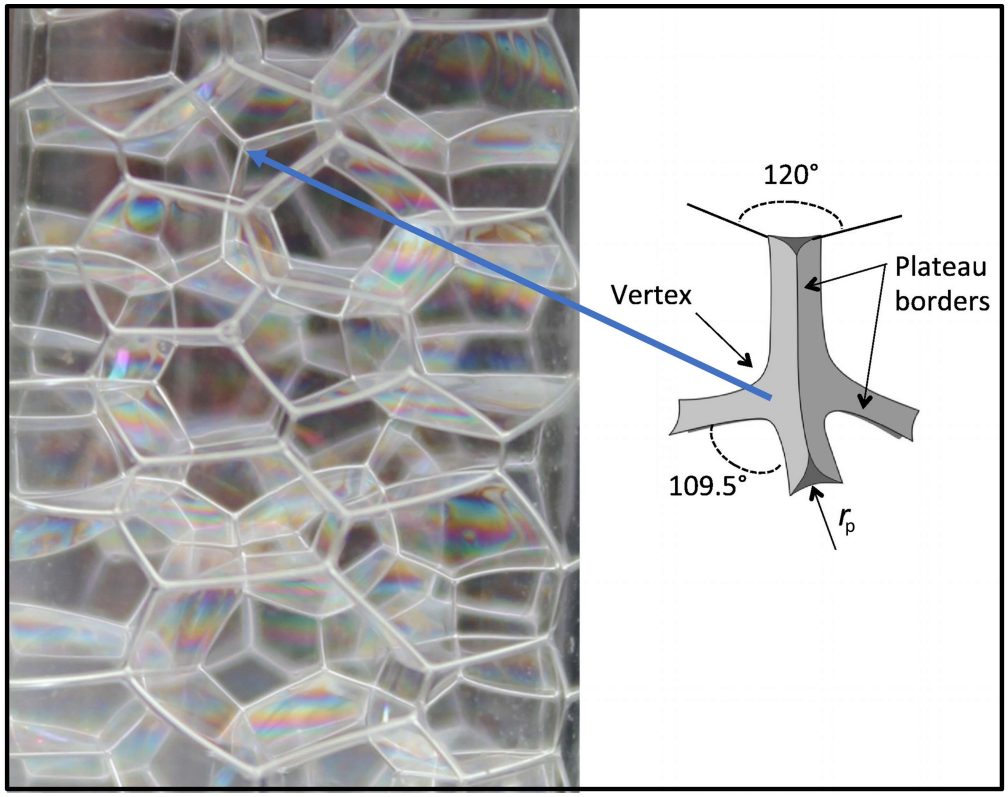

Fig 2.5: On the left is a photograph of a polydisperse aqueous foam. The Plateau border network of the foam, through which liquid drains, can be seen. The schematic on the right shows the angles at which the Plateau borders meet.

liquid fraction of a foam and the ratio of the average bubble radius to that of the Plateau border radius can be expressed as

$$\phi = C(r_p^2/r_b^2) \tag{2.6}$$

Here, r_b and r_p is the average bubble radius and the average Plateau border radius respectively. C is a constant, dependent on the structure of the foam [27].

The drainage rate, Q, through a cross sectional area of the foam can be described as:

$$Q = \left(\frac{\rho g}{\eta^*}\right) \phi^2 A L_v^{-1} \tag{2.7}$$

ρ is the liquid density, g the gravitational constant, η^* is the effective viscosity of the foam, A is the cross-sectional area of the foam and L_v is the length of the Plateau border network per unit volume [27]. η^* is related to the viscosity of the liquid phase by the following

$$\eta^* = 3f\eta_L \simeq 150\eta_L \tag{2.8}$$

η_L is the viscosity of the liquid phase and f is a dimensionless factor whose value reflects both geometry and flow resistance of a Plateau border. In the simplest drainage theory it is given by $f \simeq 50$ [27].

The liquid fraction changes with time due to drainage through the Plateau border network. Foam drainage can be describe by a non-linear partial differential equation [28, 47, 48]. It is useful to derive the drainage equation to show the physical phenomena that affect drainage and how these phenomena relate to the drainage equation.

Consider a Plateau border with cross section area $A(z,t)$, where z is the vertical coordinate and t is the time. The Plateau border is the channel between three bubbles (see figure 2.5). The Young-Laplace equation (equation 2.2) describes the curvature of the Plateau border as a function of the pressure difference between the liquid in the Plateau border and the gas in the bubble. Rearranging to find an expression for the radius of curvature R gives

$$R = \frac{\gamma}{P_g - P_l} \tag{2.9}$$

where P_g and P_l are the pressure in the gas and liquid respectively.

Assuming all three bubbles have equal pressure and therefore the cross section has a symmetrical shape, we can then relate R to its cross section area $A(z,t)$ by the following expression:

$$A = \left(\sqrt{3} - \frac{\pi}{2}\right) R^2 = C^2 R^2 \tag{2.10}$$

The main forces acting upon a volume element $A(z,t)\ dz$ of the plateau border are

gravity (ρg)

capillarity (-($\frac{\partial}{\partial z}$)$P_l$) where $P_l = P_g$ - $\frac{\gamma}{R} = P_g$ - $C\frac{\gamma}{\sqrt{A}}$

dissipation (-$\frac{\eta^* u}{A}$)

If the inertial effects are neglected, and we assume a Poiseuille type dissipation, having zero velocity at the boundaries, we can see that the dissipation is proportional to the mean liquid velocity $u(z,t)$ in the Plateau border.

The velocity of the liquid flow through the Plateau border as a function of the cross section can be expressed by the following

$$u = \frac{1}{\eta^*}\left(\rho g A - \frac{C\gamma}{2} A^{-1/2}\frac{\partial A}{\partial z}\right) \tag{2.11}$$

and substituting into the continuity equation

$$\frac{\partial A}{\partial t} + \frac{\partial}{\partial z}(Au) = 0 \tag{2.12}$$

we can obtain the drainage equation that describes the foam density as a function of time and height.

$$\frac{\partial A}{\partial t} + \frac{1}{\eta^*}\frac{\partial}{\partial z}\left(\rho g A^2 - \frac{C\gamma}{2}\sqrt{A}\frac{\partial A}{\partial z}\right) = 0 \tag{2.13}$$

Replacing the variables in the above equation with their non-dimensional counterparts produces a partial differential equation for the liquid fraction as a function of height and time $\phi(z,t)$.

$$\frac{\partial \sigma}{\partial \tau} + \frac{\partial}{\partial \xi}\left(\sigma^2 - \frac{\sqrt{\sigma}}{2}\frac{\partial \sigma}{\partial \xi}\right) = 0 \tag{2.14}$$

here, $\phi \rightarrow \sigma$, $z \rightarrow \xi$ and t $\rightarrow \tau t_0$.

This derivation is for a single vertical Plateau border. When we consider a network of randomly orientated Plateau borders and the effect of gravity acting along the direction of the liquid flow, it leads to the conclusion that the dimensionless equation for a single vertical Plateau border is the same as for a random network [49].

The equation also demonstrates the interplay between the physical phenomena that affect liquid drainage in a foam. Gravity makes the fluid flow downward throught the network of Plateau borders, setting up a liquid fraction gradient as the bottom of the foam becomes wetter than at the top. Where the foam is wetter, the Plateau border cross sectional area is larger (due to the Laplace pressure). The capillary pressure in the wetter part of the foam is therefore higher than the drier part, inducing a capillary flow. The direction of capillary flow is from areas with higher ϕ to areas of lower ϕ. Capilliarity is also influenced surface tension (capillary flow will be lower if surface tension is higher), which in turn is dependent on the type and concentration of surfactant.

Steady state flow in the Plateau borders is established where there is a balance between gravity and capillarity forces. Viscous dissipation (or hydrostatic resistance) also occurs in the Plateau borders. Dissipation is higher when the mean liquid velocity or the viscosity of the liquid phase is higher. As we saw in equation 2.11, the mean liquid velocity is influenced by the surface tension. As surface tension increases, the velocity decreases [50].

2.3 Bubble Size Distributions

The average bubble size as well as the distribution of bubble sizes depends on the method used to produce the bubbles. Flow focusing and bubbling at a low rate produce small, monodisperse bubbles. As a result, a distribution of their bubble sizes will be narrow. The method of producing a foam by axially shearing produces small polydisperse bubbles which have wide distributions. In this section we show how we obtain samples of the foam and how we measure their bubble size distributions.

2.3.1 The Microscope Slide Method

Figure 2.6 illustrates the experimental method used to measure bubble size distributions of an aqueous foam, which we have called the "microscope slide method". Two microscope slides, attached to the jaws of an adjustable wrench were inserted into the foam in an open position and then closed, trapping a small amount of foam between them (figure 2.6a). The slides were separated by spacers of a known spacing (0.1mm). An image of the foam was taken with a Canon 50D camera and processed using ImageJ's binary function and particle analysis function (figure 2.6 b, c and d). ImageJ is an open source image processing and analysis software [51]. Bubbles at the edge of the image were excluded from the analysis. The volume of each bubble was calculated using the area measurements and the known spacing between the microscope slides, from which a distribution of radii was then inferred.

Aqueous foams have produced via flow focusing or by bubbling at a low rate, where the bubble sizes have narrow distributions (monodisperse) [52]. Foams produced by axial shearing are highly polydisperse. We therefore express the average bubble size of a foam using the Sauter Mean Radius (SMR).

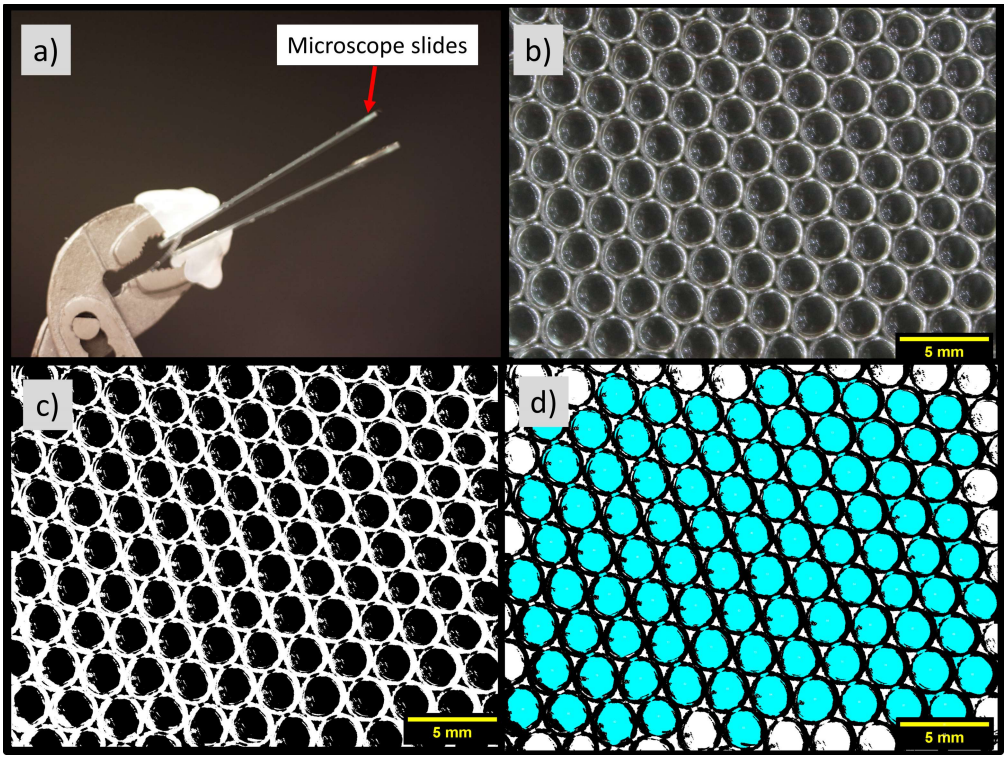

Fig 2.6: Experimental method used to measure bubble size distributions of an aqueous foam. a) Two microscope slides are attached to the jaws of an adjustable wrench. The slides are inserted into the foam in the open position, then closed, trapping a small amount of foam between the slides. Two spacers of a known thickness are attached at either end of one slide allow space for the bubbles. b) An image of a set of monodispersed bubbles trapped between the microscope slides. c) Binarised image of the trapped bubbles. d) Image after ImageJ's particle detection function was used to measure the bubble areas. ImageJ is an open source image processing and analysis software. The blue overlay represents the areas that were measured.

The SMR, r_{32}, is defined as

$$r_{32} = \frac{\sum r^3}{\sum r^2} \tag{2.15}$$

Where $\sum r^2$ and $\sum r^3$ are the sums of the radii over all the bubbles in an image. The SMR is equivalent to the mean radius of a set of monodisperse bubbles that have the same total volume and surface area as that of bubbles within a polydisperse foam. It is particularly useful where surface area is important, such as foam coarsening, where the gas inside the smaller bubbles diffuses through the bubbles films into larger adjoining bubbles (section 2.2.3).

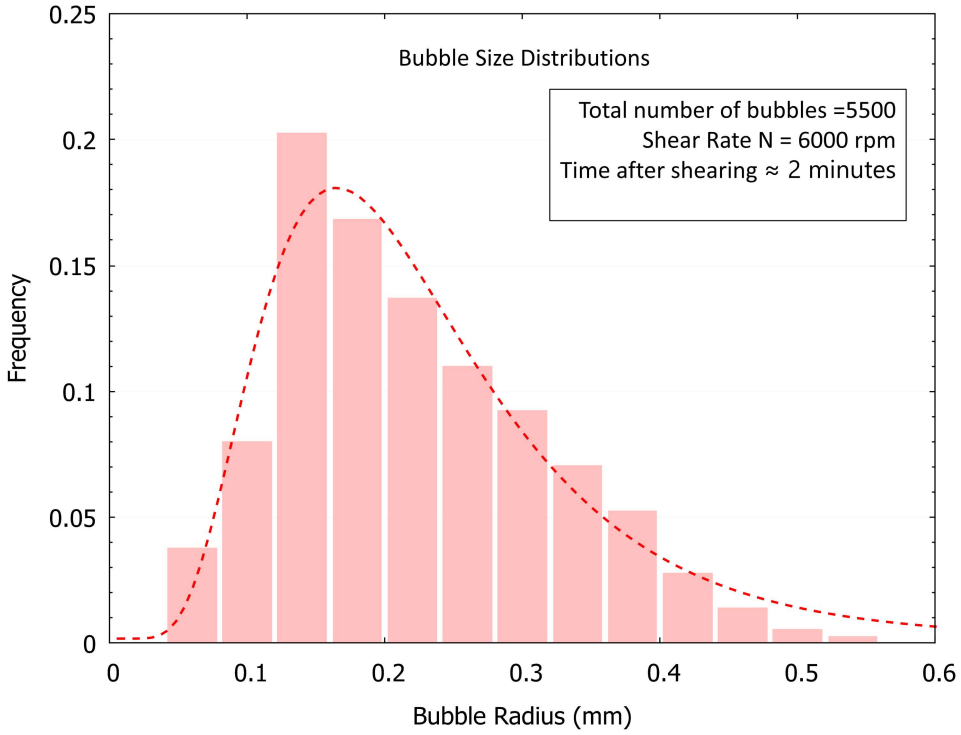

Fig 2.7: A distribution of bubble sizes obtained using the microscope slide method for foams produced via axial shearing. A log-normal fit describes the distribution, represented by the red dashed line. Bin size is given in increments of 0.04mm, ranging from 0 to 0.6mm.

The bubble size distribution of an aqueous foam is presented in figure 2.7. The foam was produced by axially shearing a surfactant solution (sodium dodecyl sulfate) at a rate of 6,000 revolutions per minute for a duration of

approximately 3 minutes, leading to an initial liquid fraction of $\phi_i = 0.25$. A sample of the foam was taken soon after the shearing ceased. The bubble sizes of between 1,000 and 1,500 bubbles per slide were then obtained by the method set out above. We repeated the process four times, giving a total of over 5,500 measurements and plotted the results. The probability density function $P(r)$ is given by the expression [53]

$$P(r) = \frac{1}{\sqrt{2\pi}wr} \exp \frac{-|\ln(\frac{r}{r_c})|^2}{2w^2} \tag{2.16}$$

Where r_c is the center of the distribution, w is the log standard deviation.

The log-normal distribution provides the most reasonable approximation for the distribution of bubble sizes in a polydisperse foam [54]. We therefore fitted the probability density function to a log-normal distribution, see figure 2.7 (red dashed line). The wide distribution is representative of the polydispersity of a foam produced by axial shearing [55].

2.3.2 The Influence of Shear Rate

Bubble sizes within a foam produced by axial shearing are determined by several factors including the average liquid fraction, surfactant concentration, the diameter ratio of the mixing disk to the mixing vessel, the rotational speed of the mixing disk, viscosity of the foam and ambient temperature. To determine how the shear rate affects the mean bubble size, we carried out a series of experiments in which we held all variables mentioned above constant, while varying only the rotational speed of the mixing disk in the surfactant solution.

The rotational speed of the mixing disk is controlled via a dial, with increments marked from 0-10. We first calibrated the dial to the actual revolutions of the disk per increment using a digital stroboscope (Extech 461831). First, a mark was drawn onto the mixing disk, then the mixer was set rotating while the stroboscope frequency was varied. The mark appeared to cease rotating

when the frequency of the stroboscope matched that of the mixer, giving the revolutions per minute of the mixing disk. This was repeated for each of the increments on the speed dial of the mixer.

The Sauter Mean Radius of a foam as a function of the rotational shear rate of the mixing disk is shown in figure 2.8. As the rotational shear rate is increased, the higher shear forces imparted on the bubble results in a reduction in the average bubble size. The range of shear rates produced by our mixer have the effect of maximally decreasing r_{32} by a factor of two. Al-Qararah *et al.* have shown r_{32} to decrease further when a number of disks or impellers are used to shear the foam [56].

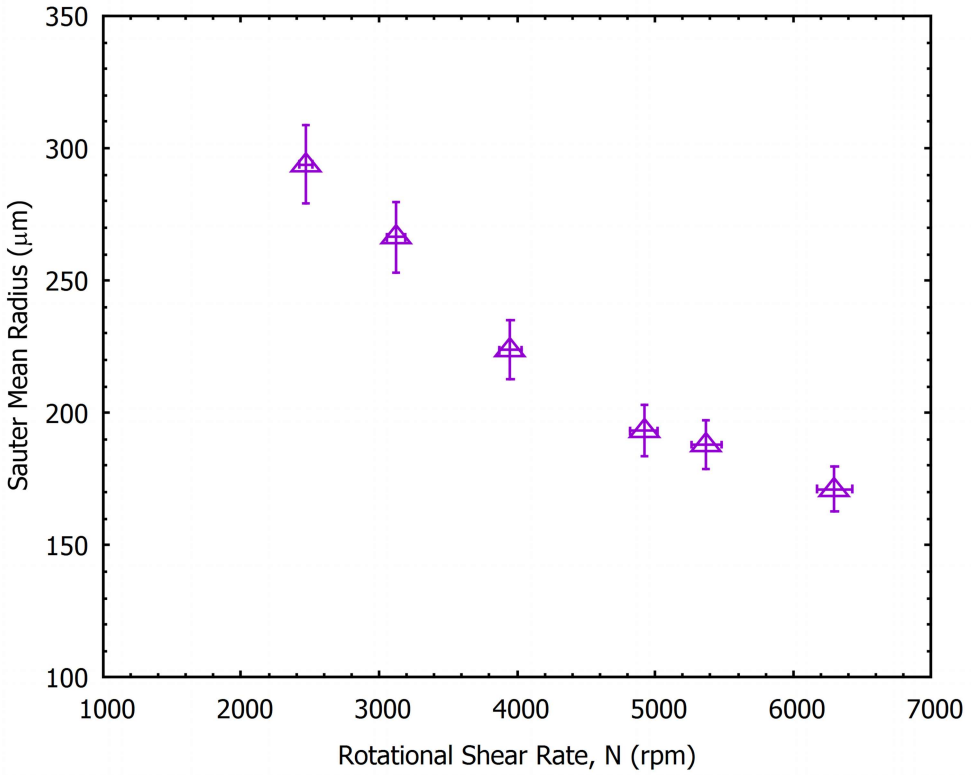

Fig 2.8: Sauter Mean Radius of an aqueous foam as a function of the rotational shear rate of the mixing disk. As the rotational shear rate is increased, the higher shear forces imparted on the bubble films results in a reduction in the average bubble size.

2.4 Flow Behaviour

When a small strain is applied to a foam, bubbles deform in an elastic-like manner, returning to their original position within the foam when the stress is removed. Increasing the applied stress beyond the elastic limit (yield stress), results in bubble rearrangements, as the foam begins to flow, exhibiting plastic-like behaviour [57] (see figure 2.9).

Aqueous foams consist of two Newtonian fluids, water and air. When either of these fluids are subjected to an increasing shear rate, the viscosity remains constant. However, when one fluid (air) is dispersed into the other (liquid) creating an aqueous foam, the resulting flow behaviour exhibits a non-Newtonian response to an increasing shear rate. Foams are shear thinning, meaning the effective viscosity of the foam decreases with an increase in the applied shear rate.

When high shear rates are applied to the foam, this results in continual bubble rearrangements as the foam flows. The flow behaviour of non-Newtonian fluids can be described by the Herschel-Bulkley equation [58–60]

$$\tau = \tau_y + k\dot{\gamma}^n \tag{2.17}$$

Where τ is the shear stress, τ_y, and $\dot{\gamma}$ are the yield stress (above which the foam enters plastic flow) and the strain rate. k is the effective viscosity of the liquid. The exponent n is less than 1 for shear thinning fluids such as aqueous foams [61].

The foams produced in this study were created by way of axial shearing. When pouring the foam from the mixing vessel into a container we found the foam was at first resistant to flow. To overcome this, we simply increased the angle of incline until flow was achieved.

In the following chapters, we will show that some of the properties of aqueous foam, enable us to produce lightweight fibrous materials when cellulose-based fibres are dispersed into the foams. We will show how the fibres can

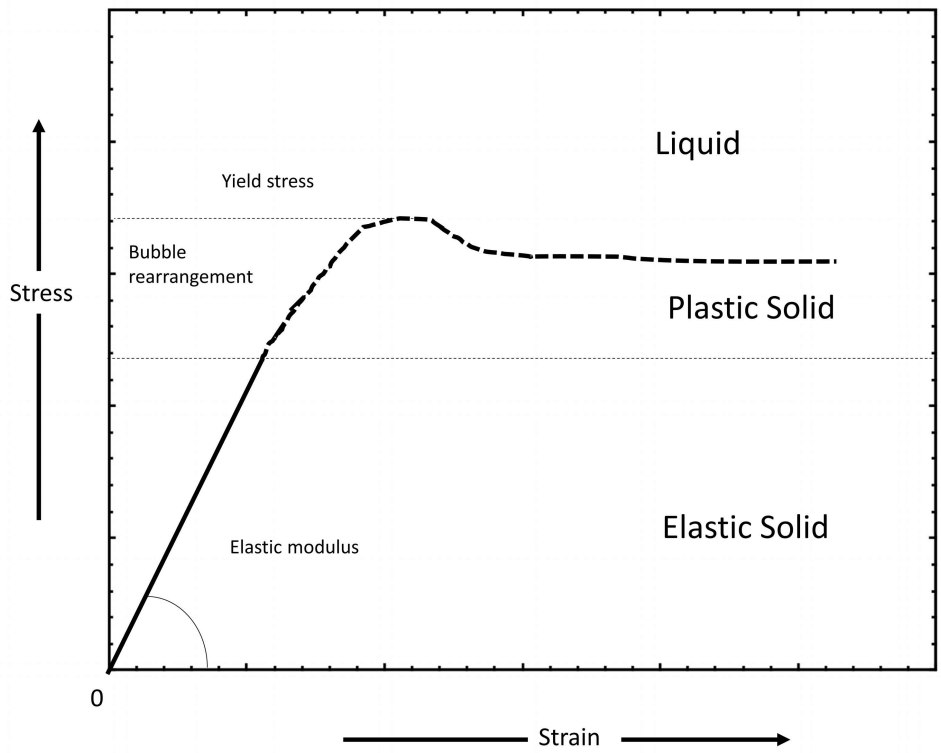

Fig 2.9: A sketch of the flow behaviour of an aqueous foam to an applied stress. Before the foam flows it behaves in a solid-like manner, exhibiting recoverable elastic deformation. Increasing the stress further results in bubble rearrangements, after which the foam begins to flow in a liquid-like manner.

alter some of the typical characteristics of a foam, such as the average bubble size, coarsening and lifetime. We also show how some of the key properties of foam can be taken advantage of to allow us gain a control over both the material and mechanical properties of these lightweight structures.

Chapter 3

Materials and Methods

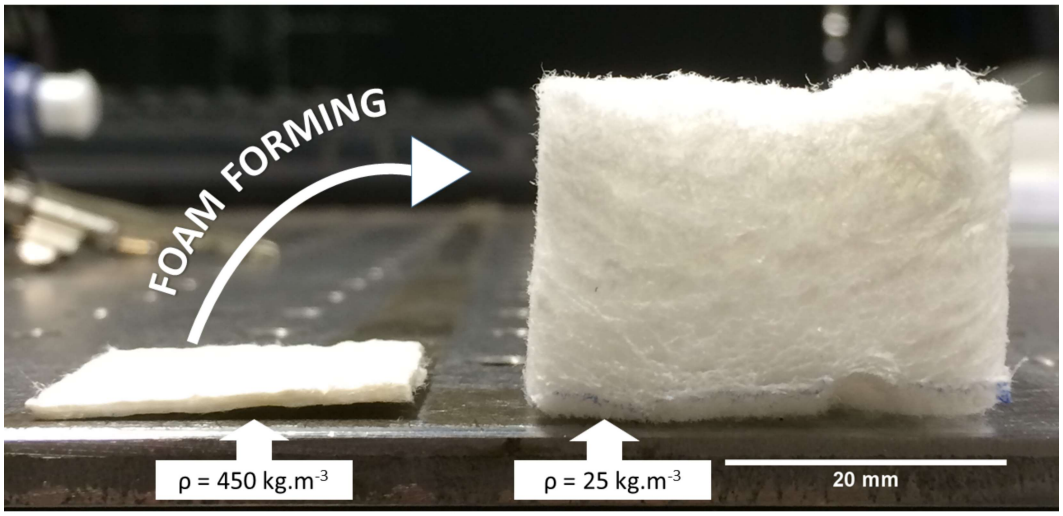

Fig 3.1: Low density fibrous structure (right) produced using the foam-forming technique. The sample was produced from a thin sheet of compressed Kraft fibres, as shown on the left. Both the sheet and lightweight sample contained the same mass of fibres. The sheet on the left has a density of 450 kg.m^{-3}, while the density of the foam-formed structure on the right is 25 kg.m^{-3}. Later we will show how the porosity of the lightweight sample can be attributed to the bubbles within the foam-fibre dispersions.

In this chapter we discuss how we use the foam-forming technique to produce foam-fibre dispersions and lightweight fibrous materials as well as

discussing the properties of the fibres that we use. Figure 3.1 shows a thin sheet of compressed Kraft fibres alongside a foam-formed three-dimensional fibre structure. Both samples contain the same type and mass of fibres. However, there is a large difference between the densities of both; the sheet on the left has a density of 450 kg.m^{-3}, while the density of the foam-formed structure on the right is 25 kg.m^{-3}.

3.1 Materials

Most of the fibrous materials investigated in this thesis are made purely of cellulose-based Kraft fibres. They contain no bonding agents (with the exception of the samples discussed in appendix B, where we investigate how a bonding agent can increase a fibrous structure's compressive strength). The reasoning was to thoroughly investigate the role of the foam over the properties of the materials without any additional influences. We chose to use cellulose fibres due to their ability to form strong fibre-fibre bonds, enabling a stable lightweight structure to be formed. According to Hirn and Schennach [62] the material strength these fibres offer arises from several different bonding mechanisms: mechanical interlocking of fibrils, capillary forces, hydrogen bonding and Van der Waal forces.

3.1.1 Fibre Properties

Kraft Fibres:

Kraft is a type of chemical process used to extract cellulose fibres from wood. It was invented in 1879 by Carl F. Dahl in Germany [64]. The word "Kraft" comes from the German word for strength, due to the process being renowned for making superior-strength paper.

The wood used to produce Kraft fibres comes from softwood needle-bearing evergreen trees such as pine. The components of wood can be classified into

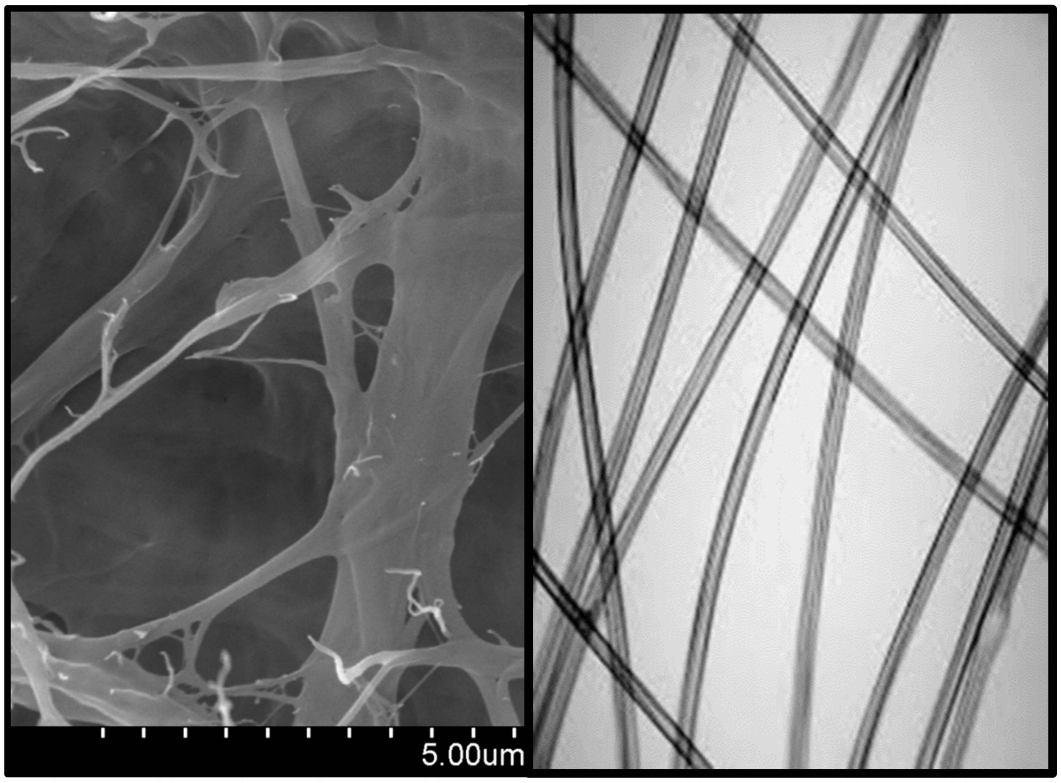

Fig 3.2: On the left is a SEM image of cellulose fibres (hardwood bleached Kraft fibres). The fibrils responsible for the mechanical interlocking of the fibres are visible. Image source: Gao *et al.* [63]. On the right is a picture of viscose rayon fibres. Note their smooth walls and lack of any fibrils, making them difficult to bond while producing lightweight structures.

four main groups; cellulose, hemicellulose, lignin and extractives. Cellulose is a long-chained carbohydrate, one of the main components in papermaking. Hemicellulose is a shorter chained carbohydrate. Lignin is a polymer that aids in binding the cellulose, hemicellulose and other plant constituents together [65–67].

Lignin is removed from the final product as its hydrophobic nature interferes with the hydrogen bonding between the cellulose fibres [68].

The Kraft process converts raw wood chips into wood pulp by chemical means. The wood chips are first screened, removing the larger chips and fines (such as sawdust). The chips are then "cooked" in a mixture of water, sodium hydroxide and sodium sulfide, to break the bonds between the lignin and the

other plant materials. The lignin and other unwanted materials are removed during this part of the process. The pulp is then bleached, resulting in the distinctive white colour of Kraft fibres.

Cellulose is the main component left after the wood is refined through the Kraft process. Cellulose fibres, being made of thread-like structures called fibrils, aid in the fibre-fibre bonding by mechanically interlocking with each other [69, 70] (see figure 3.2). Cellulose also forms chemical bonds when changed from a wet to dry state [71–73] , making it ideal for papermaking and also for our lightweight structures.

CTMP Fibres:

Chemi-thermomechanical pulp (CTMP) is another method of extracting fibres from wood. It is a mixture of both a chemical and a mechanical process. The wood chips are first chemically treated with sodium hydroxide, sodium sulfate and sodium carbonate. The chemicals soften the lignin binding the fibres together, facilitating in the extraction of the fibres. After being chemically treated, the wood chips are mechanically refined [74]. Mechanical refinement involves grinding the wood chips between two rotating metal disks at high pressure and temperature, breaking the fibre-fibre bonds. The chemical pre-treatment means less energy is required during the mechanical process to refine the fibres [75]. CTMP fibres are longer on average than fibres refined purely by mechanical means. They are also stiffer due to the higher levels of lignin left on the fibres from the process [76]. However, due to the higher levels of lignin, they form weaker fibre-fibre bonds than Kraft fibres for example.

In chapter 5 we compare the mechanical strength of two lightweight samples. One was made of Kraft fibres, while the other was made of CTMP. The CTMP sample had a higher compressive strength than the Kraft sample.

Viscose Rayon Fibres:

Rayon fibres are man-made fibres created as a substitute for silk. The process of producing the fibres involves dissolving cellulose (obtained from wood pulp) in a caustic soda solution. The excess liquid is removed from the solution and the resulting material is then shredded. Further processing, through a series of chemical reactions, lead to a viscose solution being formed. The viscose solution is then extruded through small holes, into a bath of sulfuric acid, resulting in the formation of rayon fibres [77]. The fibres are produced with well defined diameters and lengths. Being smooth-walled and not containing any fibrils, means the fibres do not mechanically interlock to each other (see figure 3.2). Later, we use viscose rayon fibres of varying lengths to establish the effect of fibre length on the compressive strength of the lightweight structures.

Other fibre types we explored with the foam-forming technique include peat fibres from the Irish peatlands and spent grain from the Guinness Breery in Dublin. Peat is partially decomposed vegetation and contains a wide range of fibre types and lengths. The peat fibres were given to us by Bord na Mona, a state-owned company that was set up to develop the peatlands of Ireland. Spent grains are a by-product of the brewing industry.

3.2 The Foam-Forming Technique and Apparatus

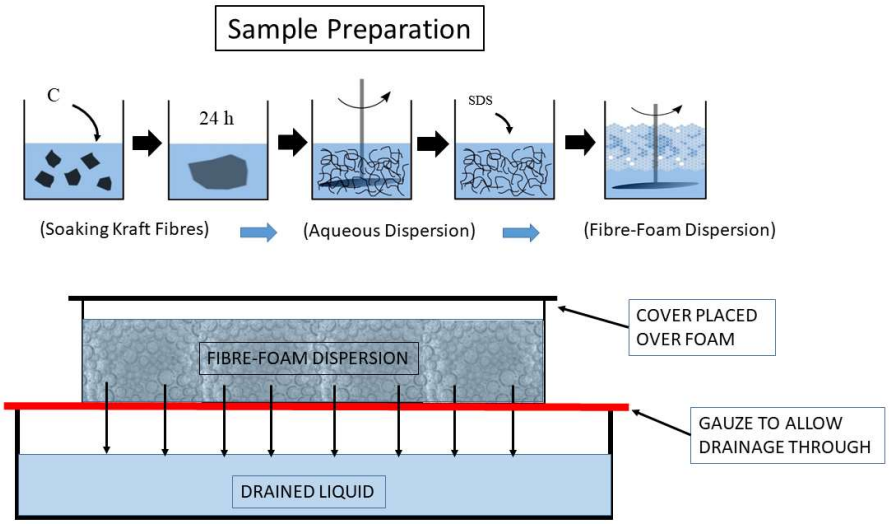

Fig 3.3: A schematic of the foam-forming technique used to create lightweight fibrous materials. The top schematic shows the steps taken to produce the foam-fibre dispersions, while the bottom is a schematic of the drainage vessel that the foam-fibre dispersions are poured into.

3.2.1 Producing a Foam-Fibre Dispersion

Foam is an ideal medium from which to create lightweight fibrous structures. Foam's ability to trap and hold fibres in suspension for an extended period of time, along with the bubbles acting as spacer particles, allows the fibres within the foam to form strong fibre-fibre bonds, resulting in a highly porous, stable fibre network remaining after all the foam has decayed [2, 78, 79].

The majority of the samples described in this thesis were made from bleached and dried softwood Kraft fibres with average length 2.0±0.1mm and diameter of 35±5μm, and thus an aspect ratio of approximately 60 [80]. The Kraft fibres were supplied in the form of a A4 sized sheets by Stora Enso,

Imatra, Finland. For a surfactant, we used sodium dodecyl sulfate (SDS) from Sigma-Aldrich with a purity of 98.5%. Sample preparation is illustrated in figure 3.3. Disintegration of dry pulp fibre sheets was achieved by first tearing the sheets into smaller pieces (approximately 5 x $5mm$) and soaking them in water for 24 hours. This allowed for the fibre-fibre bonds within the sheet to be easily broken when sheared.

Following this, the aqueous fibre suspension was placed into a vessel and sheared with a mixing disk at a constant speed (5000 RPM) for three minutes.

We define the fibre concentration c as the weight ratio of fibres in an aqueous solution, given by:

$$c = m_f / m_{aq} \tag{3.1}$$

Where m_f and m_{aq} are the mass of fibres and the mass of the aqueous solution respectively.

SDS was then added at a weight to weight (w/w) concentration of 0.67%, (1g of SDS per 150ml of water) and thus well above the CMC of 2.3g/L. The use of such a high surfactant concentration is necessary to create foams which are stable for a longer time period than the few seconds that is required for the foam forming of paper sheets [81]. In the case of paper sheets, the foam is only required for the dispersal of the fibres. We require the foam to last longer, enabling fibre-fibre bonds to form before the foam decays.

The aqueous dispersion was foamed by shearing again for three minutes. The samples described in this thesis were produced with fibre concentrations ranging from 1% to 7%. The initial volume of the aqueous fibre dispersions varied from 300ml to 600ml; this resulted in a final volume of fibre-laden foam of 1200ml, corresponding to liquid fractions ϕ_i of 0.25, 0.33, 0.42 and 0.50.

3.2.2 Producing Lightweight Fibrous Materials

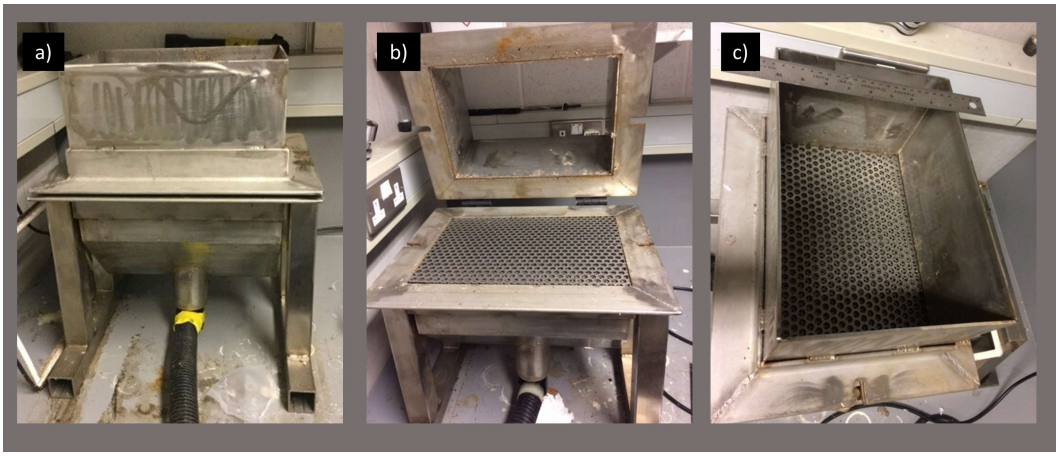

Fig 3.4: The photographs show the vessel in which the foam-fibre dispersions were placed. To create sheet-like materials, a vacuum is attached to the black hose to extract the liquid from the dispersions. When producing the lightweight materials, liquid from the foam is allowed to gravity-drain into the base of the vessel. a) Side view with the upper portion in the closed position. b) The top half is open to allow for the removal of the material after the foam has been extracted. c) Top view looking inside the vessel. A fine wire gauze is placed on top of the metal grating (metal sheet with large holes) to stop the fibres from draining through (not shown in photographs).

After generating the foam-fibre dispersion it was then poured into a vessel (width 125mm, length 200mm, depth 50mm) with a wire mesh (50μm hole size) as a base to allow the liquid to drain from the dispersion (figure 3.4).

A rigid plastic sheet was placed on top of the container during the drying process. The plastic sheet did not touch the foam-fibre dispersion, nor did it make an airtight seal. However, we found through initial experiments that the sheet plays a crucial role, particularly for samples with lower fibre concentrations, which would collapse completely without its presence. The sheet reduces the evaporation of the liquid; the resulting extension of the drying time may contribute to a better bonding of the fibres, enabling us to reduce the minimum fibre concentrations required for mechanically stable structures. Furthermore, it may slow drainage by slowing air pressure equalisation between the top and bottom of the dispersion.

3.3 Drying the Lightweight Fibrous Materials

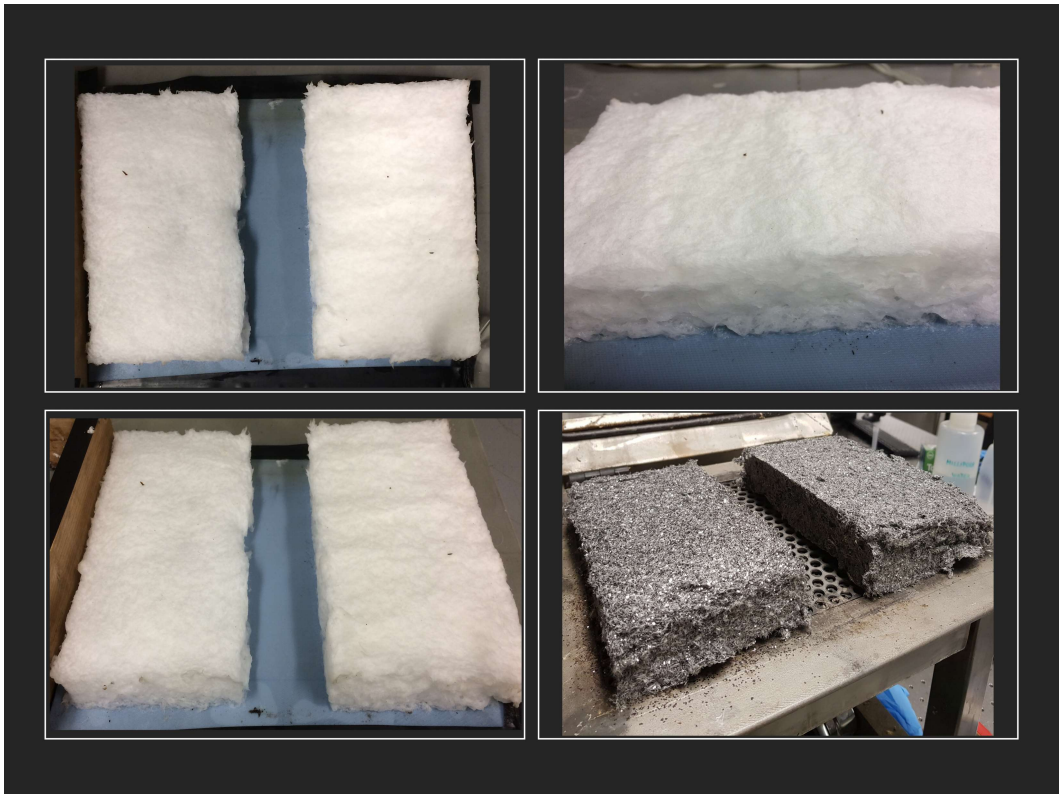

Fig 3.5: Samples left to dry on the bench in our laboratory. All samples contained Kraft fibres. The samples on the bottom right contained graphene flakes as well as Kraft fibres.

All of the lightweight fibrous structures discussed in this thesis were allowed to dry at room temperature via liquid drainage and evaporative mass loss. Initially the samples were allowed to dry in-situ in the drainage vessel. After approximately 12 hours, we removed the plastic sheet and the sample, together with the mesh that supports it from the vessel. The sample was placed onto a bench in the laboratory until fully dry (see figure 3.5). We found this approach sped up the drying time by exposing more of the surface area to air. However, at this point there was still a significant volume of liquid contained within the fibrous structure. We therefore monitored its weight at regular intervals until drying had effectively ceased. The samples were considered dry when

the mass of the sample returned to the same mass as the fibres used to create the dispersion ($\pm$ 5%). Later, we discuss the effect of fibre concentration on the drying times of the lightweight materials.

The dried samples were then carefully removed from the mesh and cut into equal sized pieces using a surgical scalpel. The dimensions of each piece were 33mm by 33mm, with a height that was dependent on fibre concentration.

We use these samples to investigate the material and mechanical properties of the samples, such as how sample density scales with fibre concentration, the effect of sample density on mechanical strength, void size and fibre orientation distributions within the samples.

Chapter 4

Foam-Fibre Dispersions

In this chapter we examine how the addition of fibres to a foam affects its properties, by making comparisons with the properties of a pure foam. We then vary the fibre concentration and report on the minimum concentration required to form stable fibrous structures, its effect on the volume of foam produced (for a fixed shear rate) and its influence on the drying times of the lightweight materials.

Bubble size distributions are controlled by certain aspects of the experimental set up. For instance, the relationship between the diameter of the mixing disk and that of the container the dispersion is sheared in, which controls the effective shear rate of the mixing disk, as well as surfactant concentration all have an influence on the bubble size within a foam.

Lappalainen *et al.* and Al-Qararah *et al.* have shown surfactant concentration and the type of fibres dispersed in the foam both have an influence over the average bubble size in foam-fibre dispersions [82, 83].

For the purpose of our investigations, we hold the following parameters of our system constant: the surfactant concentration (kept above the CMC to allow for the production of a stable foam), the volume of foam-fibre dispersion produced, the speed of the mixing disk (rpm) and the diameter ratio of the mixing disk to the container, therfore producing a constant shear rate. Holding these parameters constant allows us to determine how the variation in fibre concentration impacts on the properties of the foam-fibre dispersions.

Generating a foam by axial shearing requires the liquid to flow sufficiently as to entrain air into the aqueous dispersion, creating the bubbles. The addition of fibres to a foam has the effect of increasing its effective viscosity [84, 85], making the foam more resistant to flow. We explore the effect of fibre concentration on the volume of foam produced for a constant shear rate. We find that as we increase the fibre concentration, c , the volume of foam produced decreases. We attribute this to the increasing viscosity of the foam with c.

We show the addition of fibres have a remarkable effect of arresting coarsening and significantly extending the lifetime of the bubbles within the foam-fibre dispersions. The initial liquid fraction of the dispersion appears to have little or no effect on either coarsening or the lifetime of the bubbles.

We establish the bubble size distributions of two foam-fibre dispersions with a view to understanding how they are related to the voids in the resulting lightweight fibrous structures come to be formed. Later, in chapter 6, we make a comparison between these bubble size distributions and the void sizes of the foam-formed fibrous structures.

Finally, as the fibrous structures air dry in the lab, we monitor the mass lost due to both drainage and evaporation and determine the influence of fibre concentration.

4.1 Experimental Setup and Method

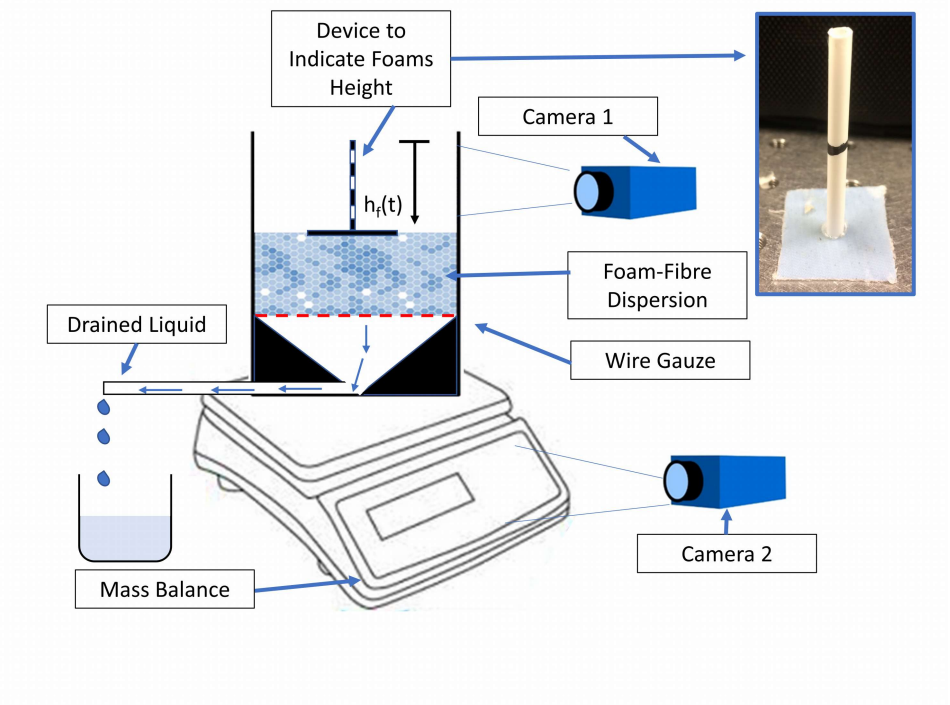

Fig 4.1: A schematic of the experimental setup used to measure the mass loss from the dispersion as well as the change in height as a function of time. Camera 1 recorded the change in height of the foam and foam-fibre dispersions, while at the same time, camera 2 recorded the mass loss from the dispersions. The inset (top right) shows the "floater" we placed on top of the foam/foam-fibre dispersion to measure the change in height as it decayed.

Figure 4.1 shows a schematic of the experimental setup used to measure the mass loss and change in height of the foam-fibre dispersions as they dried. The drainage vessel was placed on a mass balance with the top aperature left open. After the dispersion was poured into the drainage vessel, liquid from the foam-fibre dispersion drained through a fine wire gauze, with the liquid exiting through a funnel and away from the scale. The cameras recorded the height of the dispersion as it drained as well as the mass that was lost from the dispersion due to drainage and evaporation.

As the foam decreased in height, we observed that bubbles adhering to the sides of the container could block the view of the camera. To overcome this, we made a light "floater" from a thin plastic tube with a small piece of gauze as its base, and placed it on top of the foam (top right of figure 4.1). This device moved down as the foam decayed. The camera was focused on the tube and its height was monitored over time. All experiments were carried out in our laboratory at room temperature (approx 21 ^{0}C $\pm$ 2 ^{0}C).

4.2 Minimum Fibre Concentration for Producing a Stable Fibre Network

In this section we determine the minimum fibre concentration in an aqueous dispersion that will lead to a stable fibre network being formed after the foam has completely decayed.

Below a minimum concentration, an insufficient number of fibre-fibre contacts are formed leaving the network of fibres unstable, resulting in the network collapsing. All the foam-fibre dispersions in this section had an initial liquid fraction of 0.25, while the fibre concentrations ranged from 0% to 1%.

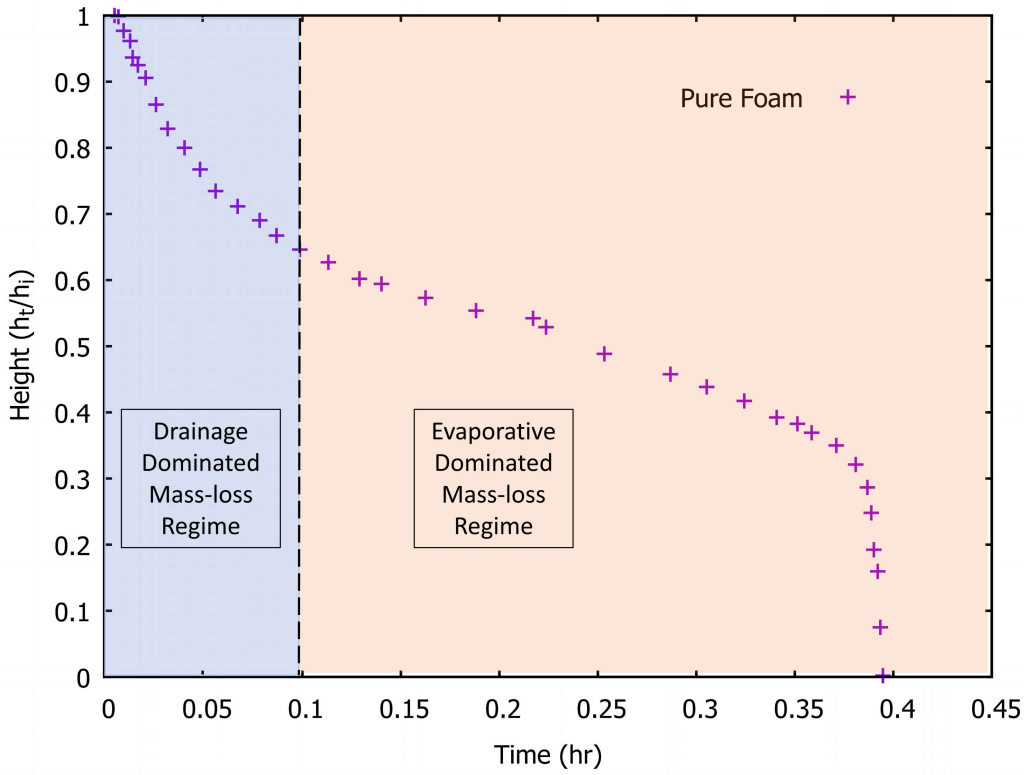

Fig 4.2: The height of a pure foam (no fibres added) as a function of time. The initial sharp decrease occurs during the drainage-dominated mass-loss regime, followed by a slower rate of decrease in the evaporative regime. The sharp decrease at around 0.4 hours is due to the weight of the measuring device collapsing the foam.

Figure 4.2 shows the height of a pure foam (no fibres added) as it decays over time. Two mass-loss regimes are evident. In the first regime, liquid drainage is the dominant mass-loss mechanism. The foam's height decreases rapidly. In the second regime, evaporation takes over as the dominant mass-loss mechanism, where the bubble films become thinner and eventually burst as the liquid evaporates from the foam. In this regime, the height of the foam continues to decrease but at a much slower rate, until no foam remains. The sharp drop-off towards the end is due to the weight of the floater causing the foam to collapse.

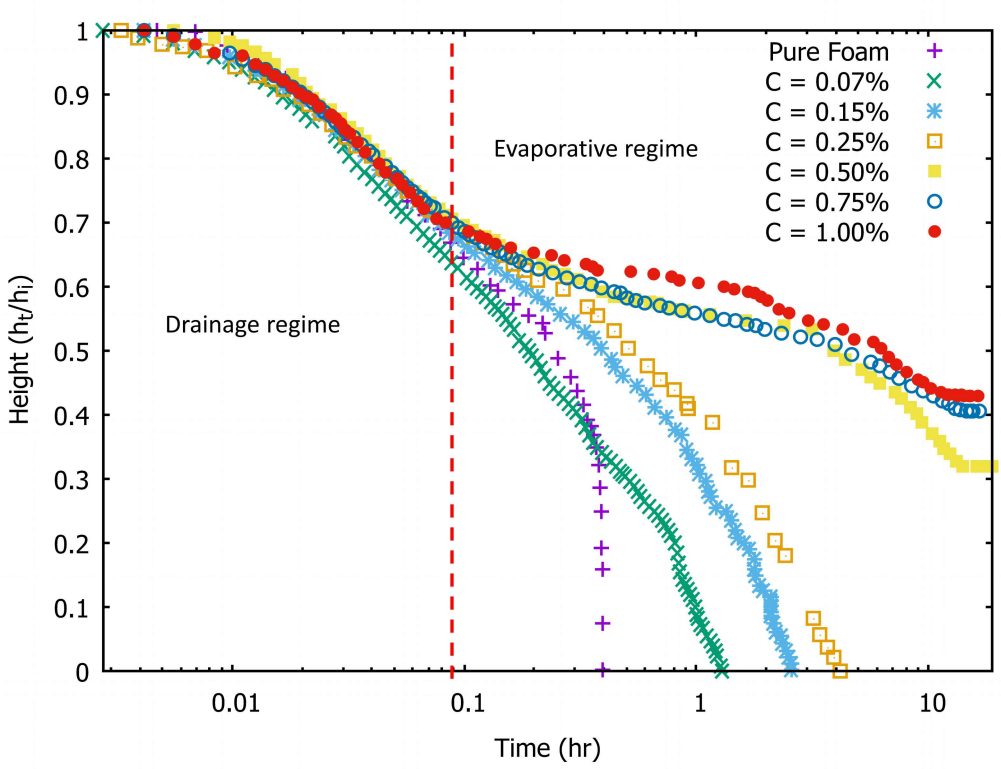

Fig 4.3: A semi-log plot of the height of several foam-fibre dispersions as a function of time. The fibre concentration ranged from 0% to 1%, while ϕ_i was 0.25 for all samples. The initial liquid fraction for all dispersions was 0.25. Samples with a fibre concentration of 0.25% and below, all collapsed.

Figure 4.3 shows the heights of a range of foam-fibre dispersions, with varying fibre concentrations, as a function of time plotted on a semi-log scale. ϕ_i was 0.25 in all cases. All data sets followed a similar trend during the drainage regime, but deviated in the evaporative regime. Dispersions with an insufficient fibre concentration collapsed fully, represented by $\frac{h(t)}{h(t=0)} \rightarrow 0$, where h is the height and t is time. This was due to an insufficient number of fibre-fibre contacts being formed to produce a stable fibre network after the foam had decayed. Where the fibre concentration was sufficient to produce stable samples, the height of the dispersion remained constant, indicated by a plateau region. The plateaus of the stable samples are more evident in figure 4.4.

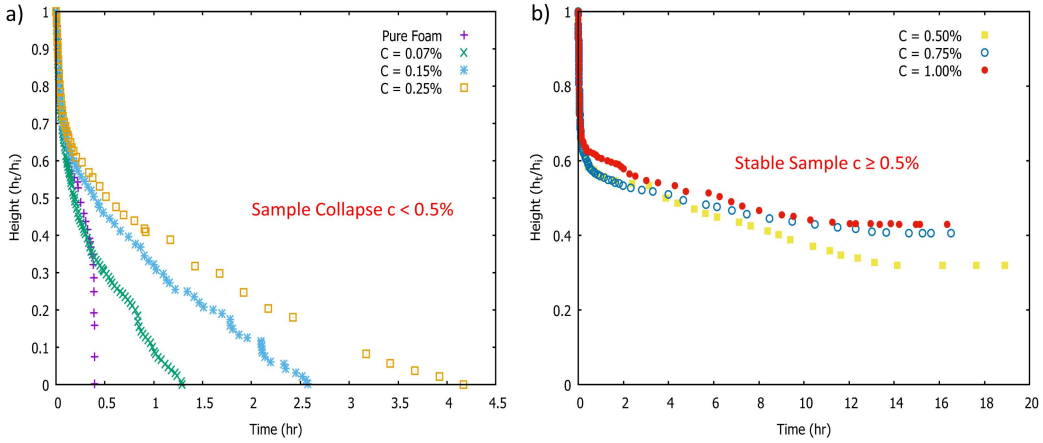

Fig 4.4: The figure on the left shows the samples that fully collapsed. Fibre concentrations ranged from 0 to 0.25%. The figure on the right shows the stable samples i.e. samples that did not fully collapse. The final height of the samples is dependent on fibre concentration, a higher concentration leads to a thicker sample (as seen in the plateau regions in the figure on the right). This only holds true for low concentrations (below $\approx 1\%$), above this concentration the final height of the sample is independent of c.

The heights of the foam-fibre dispersions as a function of time are shown in figure 4.4. We have separated the data into two figures, figure 4.4a shows the dispersions which resulted in a full structural collapse ($c \leq 0.25\%$), while above this threshold (figure 4.4b) all the dispersions displayed only a partial collapse. Both figures are shown on a linear time scale, making the plateaus in the stable samples more apparent. In section 4.5 we explore the drying times of the dispersions where c is above this minimum requirement.

4.3 The Effect of Fibre Concentration on Foam Production

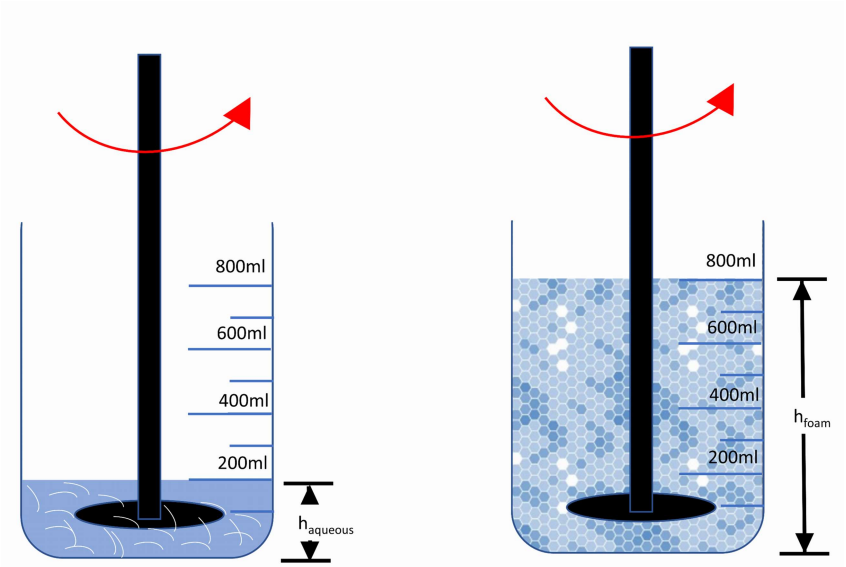

Fig 4.5: Schematic of the shearing disk and mixing vessel used to create the foam and foam-fibre dispersions. The rotational shear rate was kept at a constant 4500 RPM.

The minimum fibre concentration required to form a stable low-density structure was explored in section 4.2. Dispersions at or below a fibre concentration of 0.25% led to a full sample collapse during the drying phase. We investigated whether an increase in the fibre content of the dispersion would change the volume of foam-fibre that is produced. For this experiment, we held the rotational shear rate of the mixing disk (4500 RPM) and the volume of the aqueous fibre dispersions (200ml) constant, see figure 4.5. The mixing disk was lowered into the container to a height that coincided with 800ml of pure foam being generated at a shear rate of 4500 RPM.

We then increased the fibre concentration in subsequent aqueous dispersions and measured the resulting volume of the foam-fibre dispersions produced.

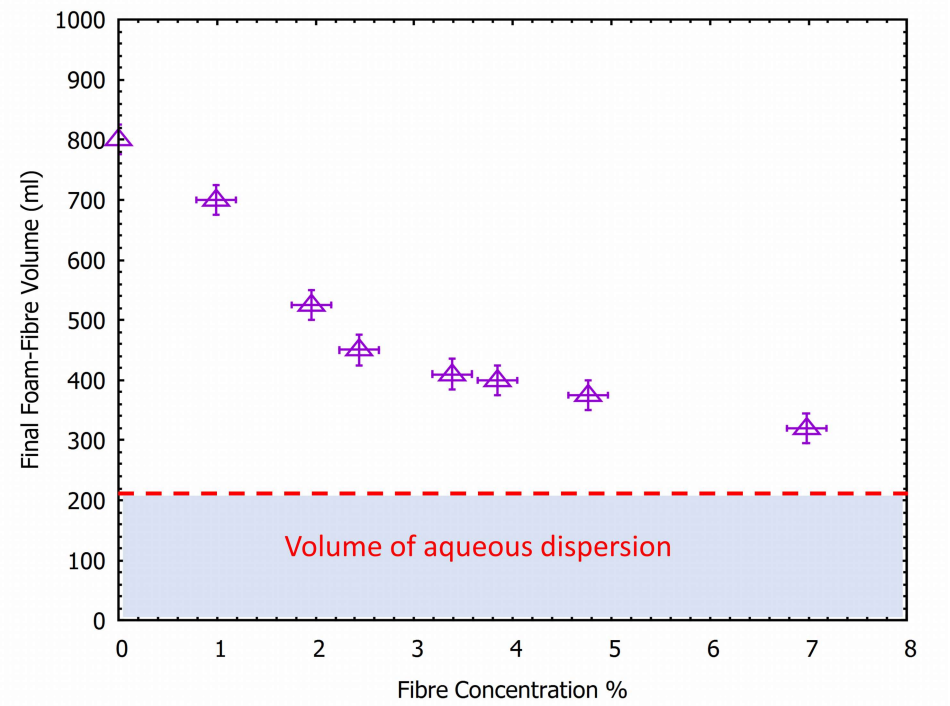

Fig 4.6: Final volume of the foam-fibre dispersions as a function of fibre concentration in the aqueous dispersion. Increasing the fibre concentration leads to a reduced volume of foam-fibre dispersion being produced for a fixed shear rate.

Figure 4.6 shows that as the fibre concentration is increased, the volume of the resulting foam-fibre dispersion decreases. Being a non-Newtonian fluid, the shear stress imparted by the rotational mixing of the foam can be described by the Herschel-Bulkley equation 2.17.

Hou and Wang have shown that the effective viscocity of a foam increases with the addition of fibres [86]. Therefore, the shear stresses imparted on the foam-fibre dispersions during the mixing process are increased by the addition of more fibres. However, even with an increase in shear stress, the volume of the foam is reduced. This could be because the increased effective viscosity of the foam makes air entrainment more difficult to achieve, which may be responsible for the reduction in the final volume of foam produced.

4.4 Coarsening and Bubble Size of Foam-Fibre Dispersions

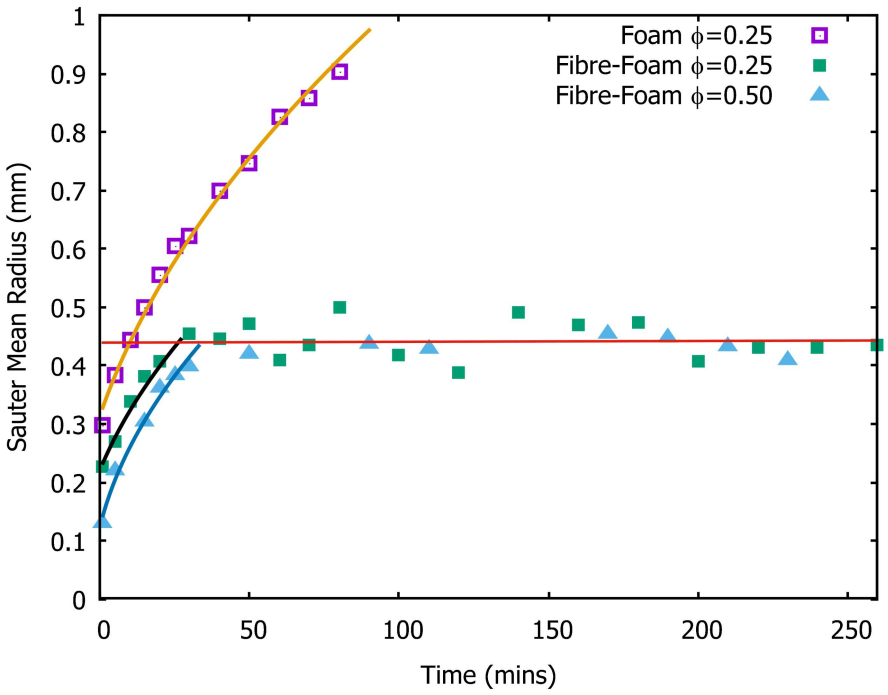

Fig 4.7: Coarsening behaviour of a pure foam and two foam-fibre dispersions. The fits represent the typical bubble radius scaling of $t^{1/2}$, fitted through the full lifetime of the pure foam and for up to 30 minutes for the foam-fibre dispersions. The dispersions display a plateau region after approximately 30 minutes. The dispersions (ϕ_i = 0.25 and 0.50) contained fibre concentrations of 2.3% and 1.1% respectively.

We now make a comparison of the coarsening behaviour between a pure foam ($\phi_i = 0.25$) and two foam-fibre dispersions with different initial liquid fractions (ϕ_i = 0.25 and 0.50). Each of the dispersions contained 7g of Kraft fibres, equating to fibre concentrations of 2.3% and 1.1% respectively.

The Sauter Mean Radius of the bubbles in the pure foam was seen to follow the typical scaling of $t^{1/2}$, as the average bubble size within the foam continually increased [87]. However, when fibres were added, we observed that they had the effect of arresting coarsening after approximately 30-40 minutes.

The results are shown in figure 4.7. Interestingly, the initial liquid fraction of the dispersions appeared to play no role in the bubble size at which coarsening ceased, suggesting that it is the fibre content rather than the liquid fraction which determines the bubble size at which bubble growth is arrested.

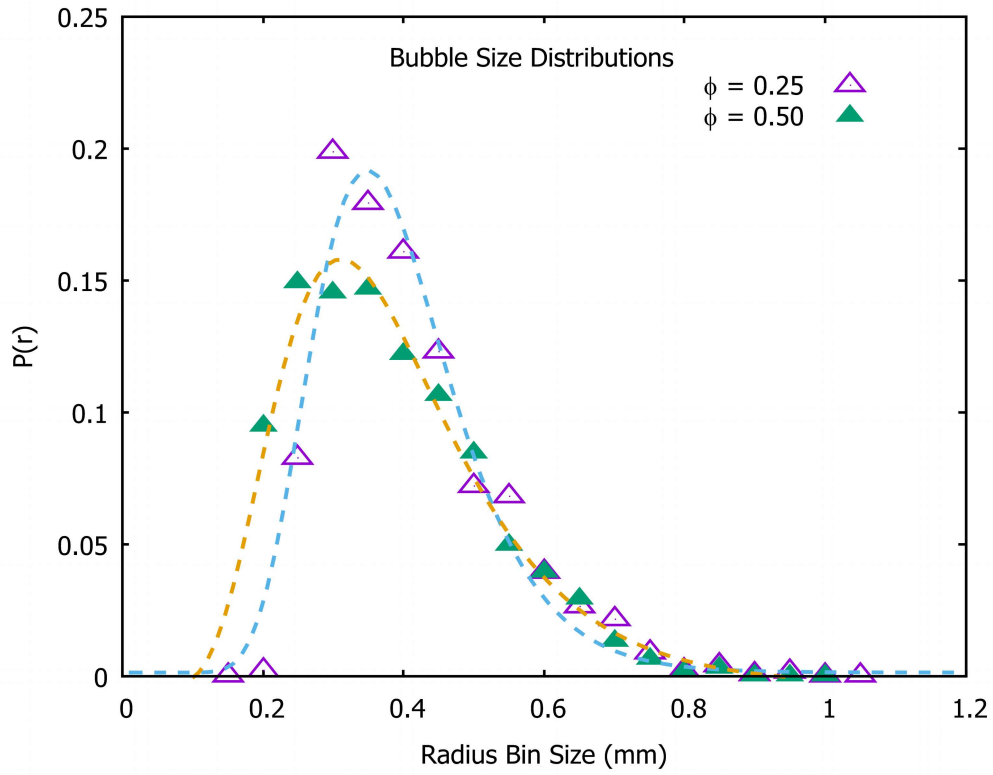

Fig 4.8: Bubble radius distributions for two foam-fibre dispersions in the plateau region of the data show in figure 4.7. The distributions are described by log-normal fits with both dispersions displaying very similar characteristics, despite the different initial liquid fractions.

Figure 4.8 shows the distribution of bubble radii in the plateau region of figure 4.7 for the two dispersions. The distributions display very similar characteristics, and both are described by log-normal fits equation. The probability density function $P(r)$ fitted to the data in figure 4.8 is given by equation 2.16

We will refer to these distributions later in chapter 5, where we will make a comparison between the bubble size distributions of the foam-fibre dispersions

and the distributions of void sizes found in the lightweight fibrous structures, after the foam has decayed and the material has dried. The distributions are similar to those of the pure foam presented in figure 2.7, also described by a log-normal fit. The range of bubble sizes in the pure foam (figure 2.7) were smaller than those presented here as they were obtained as soon as shearing of the foam ceased, while the distributions presented here are measured at $t \approx 40$ mins.

4.5 Drying times: Drainage and Evaporation

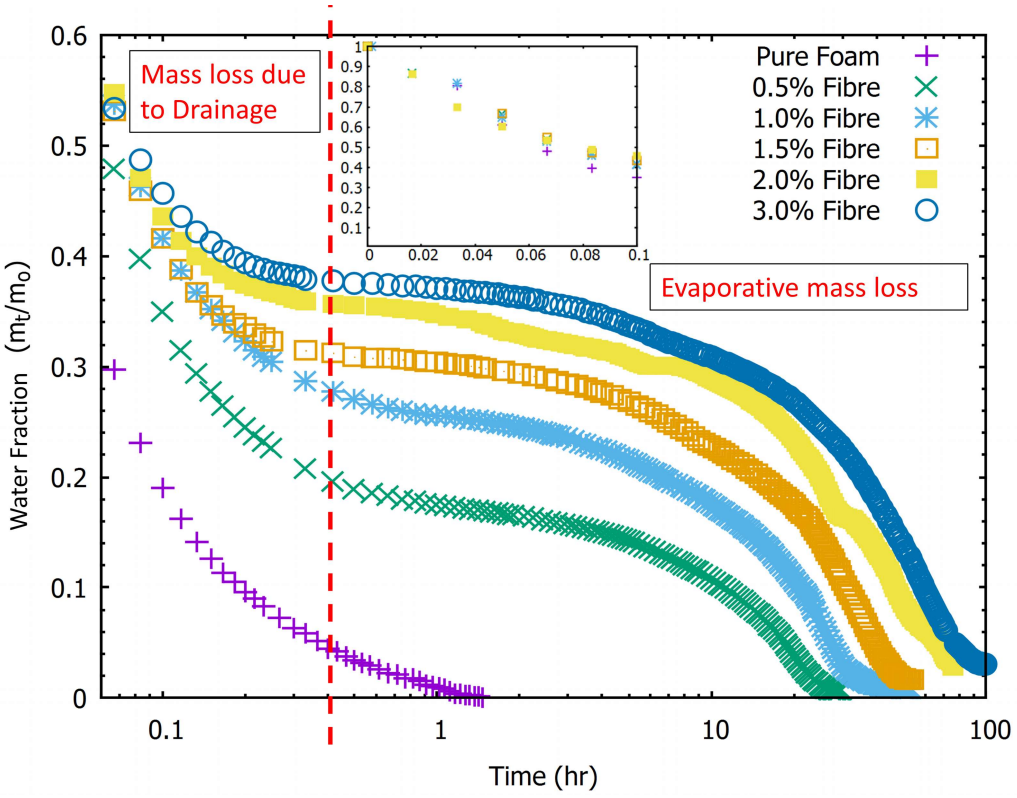

Fig 4.9: Mass loss due to drainage and evaporation for a pure foam and several foam-fibre dispersions. The x-axis (time) is displayed on a log scale up to 100 hours. Increasing the fibre concentration results in an extension of the required drying time. Two regimes are apparent, the first being a rapid mass loss due to drainage, the second regime is not as steep as mass is lost at a mcuh slower rate by way of evaporation. The inset show the first few minutes of rapid mass loss, presented on a linear scale. Over half the mass is lost due to drainage in the first five minutes.

The drying times of the resulting fibrous structures made from foam-fibre dispersions with concentrations above the critical fibre concentration of 0.25% were analysed. Fibrous structures dry by way of liquid drainage and evaporation (see figure 4.9). The experimental setup was the same as outlined earlier (figure 4.1). The liquid draining from the dispersion was directed away from the mass balance by a funnel and tubing, allowing us to measure the mass lost due to drainage and also evaporation.

We define the sample to be dry when it returns to the same mass as that of the fibres added to the original dispersion within ±5%. The effect of increasing the fibre content on the drying times is apparent in figure 4.9; an increase in fibre concentration requires an extended period of time before the sample is fully dry.

Fibrous structures can can be dried in several ways. Impingement drying is suited to drying highly porous material as it involves circulating a warm air current through the porous network, with the moisture content being removed as the air is recycled back through the material [88]. However, impingment drying or any drying technique that forces air through the porous structure can have a detrimental effect on the material if the fibres are still being supported by the bubbles in the foam. To dry the fibrous materials in this study we opted to allow the material to naturally dry at room temperature, thus reducing the impact that drying methods may have on the structures.

After a period of time (dependent on fibre concentration and ambient temperature), the evaporative mass loss from the dispersions reached a continuous rate, as indicated by the linear sections in figure 4.10 a and b. The point at which the rate of mass loss became linear increased with fibre concentration. The height collapse of the two dispersions is also plotted in figure 4.10. We observed that each reached a stable height long before evaporation had ceased, represented by the plateau in the green data sets.

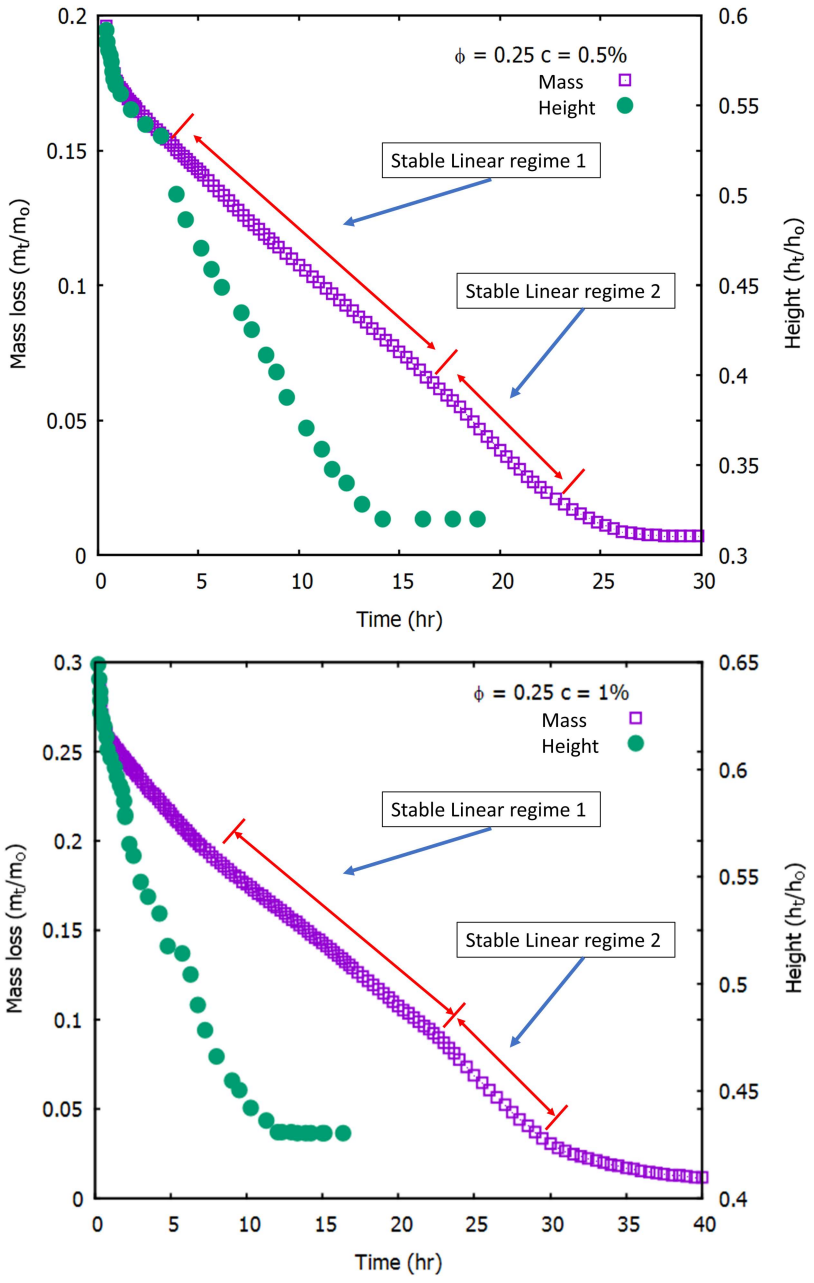

Fig 4.10: Drying times and height collapse of two of the foam-fibre dispersions. a) $c = 0.5\%$ and b) $c = 1\%$. Both samples reach a stable regime (no change in height) long before drying has finished. Increasing the fibre concentration results in an extension in the drying time due to an increase in the volume of liquid being retained on the fibres. Both data sets displayed two distinct linear regimes. The second regime shows an increase in the evaporative mass loss, presumably due to the bubbles rupturing, exposing more fibres from which evaporation can occur. All the data displayed these two linear regimes.

Interestingly, all the dispersions displayed two distinct linear regimes (highlighted in figure 4.10). The first regime displayed a lower rate of evaporative mass loss than the second regime. Both regimes appeared in all the data sets, with the onset of the second regime starting later as the fibre concentration was increased (the start of the second regime takes place at approx. $t = 18$ hours where $c = 0.5\%$ and $t = 24$ hours where $c = 1\%$).

The second linear regime we find with all data sets indicates an increased rate of mass loss from the dispersions. This may be due to the bubbles at the surface and within the foam rupturing, exposing a larger number of wet fibres (from which evaporation occurs) to the outside environment. An increased exposed surface area would result in an increase in the evaporative mass being lost.

The onset of the second regime is seen to increase in time as c is increased. Dispersions that have a higher fibre concentration retain more liquid. It may be that this liquid and the fibres acting as pinning sites for the films, are prolonging the onset of the second regime by keeping the bubble films wetted for longer, thereby extending the bubbles' lifetimes [89].

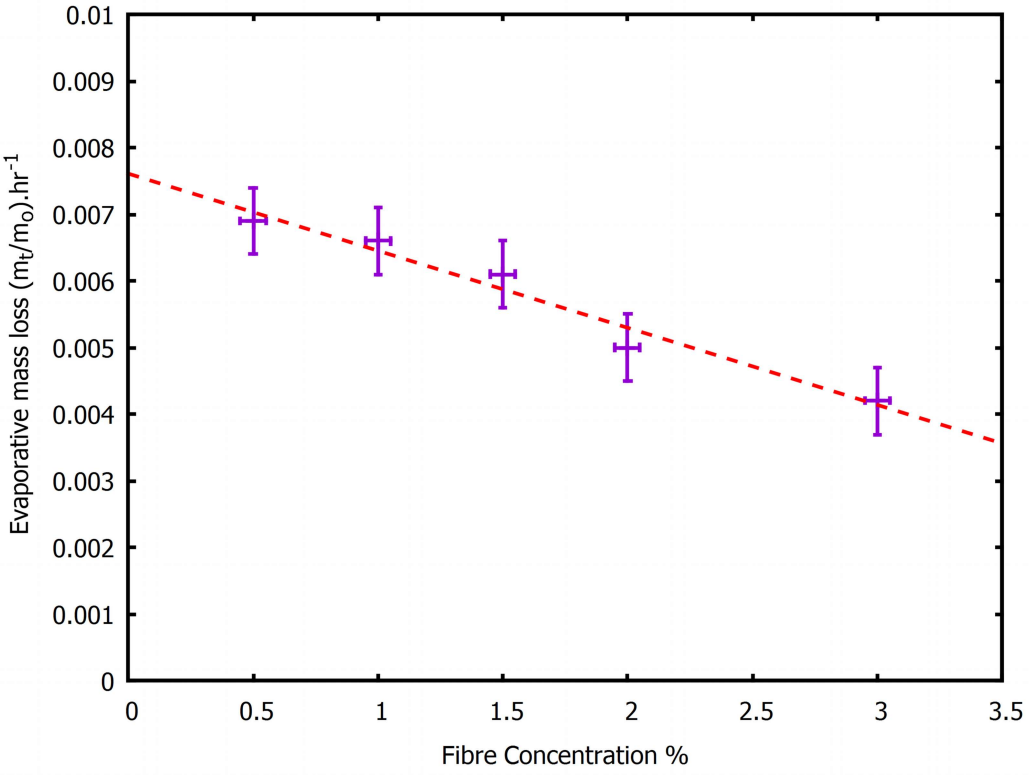

Fig 4.11: Rate of evaporative mass loss in the first linear regime as a function of fibre concentration for the data sets plotted in figure 4.9. An increase in fibre concentration leads to a lower rate of evaporative mass loss.

Figure 4.11 shows the slopes of the first linear regimes of the data sets plotted in figure 4.9. The rate of evaporative mass loss can be seen to decrease linearly as c is increased.

4.6 Conclusions

The addition of fibres to a foam changes its properties. Adding fibres greatly extends the lifetime of the foam. In fact, while measuring the coarsening of a foam-fibre dispersion we found that after 14 hours, the dispersion still contained bubbles, while the lifetime of a pure foam was around 90 minutes. The fibres were found to alter the typical coarsening behaviour of the foam by arresting the growth of the bubbles. After a short period of time (approximately 30 minutes), bubble growth ceased, while the bubbles remained in the dispersion for a long time after. The upper limit of growth of the bubbles was found to be independent of the liquid fraction.

Exploring the minimum fibre concentrations to create low density structures we found the fibre concentration must be above a minimum of 0.25% (when ϕ_i =0.25), below this concentration all the dispersions collapsed due to an insufficient number of fibre-fibre contacts being made. As fibre concentration was increased, the maximum volume of foam produced decreased (for a fixed shear rate).

We have shown that the mass loss from the dispersions, after the foam has been poured into a drainage vessel, is by liquid drainage and evaporation. The majority of the mass being lost in the initial few minutes is due to liquid draining from the dispersion through the plateau borders of the foam. After the initial rapid drainage, drying of the dispersions is dominated by evaporative mass loss. The duration of the evaporative regime increases with fibre concentration, while the rate of mass loss in this regime decreases with an increase in fibre concentration. We also identified two linear regimes during the evaporative mass loss phase. The rate of mass loss in the second regime was larger than the first. We speculate that this may be due to the bubbles within the foam rupturing, exposing an increased number of fibres (and area) from which evaporation can occur.

Chapter 5

Properties of Lightweight Fibrous Materials made using the Foam-Forming Technique

Our work so far has shown that a variation in the liquid fraction of a foam-fibre dispersion has very little effect on the bubble size distributions or coarsening, but what about the resulting foam-formed fibrous structure itself? In this chapter, we investigate the material and mechanical properties of these lightweight fibrous structures. We begin by looking at how the density of the samples scale with fibre concentration and the influence of the liquid fraction of the foam-fibre dispersions used to produce the structures. Then we explore the mechanical properties of the structures through uniaxial compression testing. From the stress-strain response, we determine how the compressive modulus scales with sample density and how the initial liquid fraction influences this scaling.

Finally, we eliminate sample density as a variable, producing four similar density samples while varying the initial liquid fraction of the foam-fibre dispersions during production. Through compression testing, we show a broad

variation in the relative strengths of each, which we attribute to the initial liquid fraction of the dispersions.

All of the samples discussed in this chapter were allowed to air dry and contained no foam or liquid. Where we refer to the liquid fraction ϕ_i, we are referring to the initial liquid fraction of the foam-fibre dispersion used during sample production.

5.1 Density, Fibre Concentration and Liquid Fractions

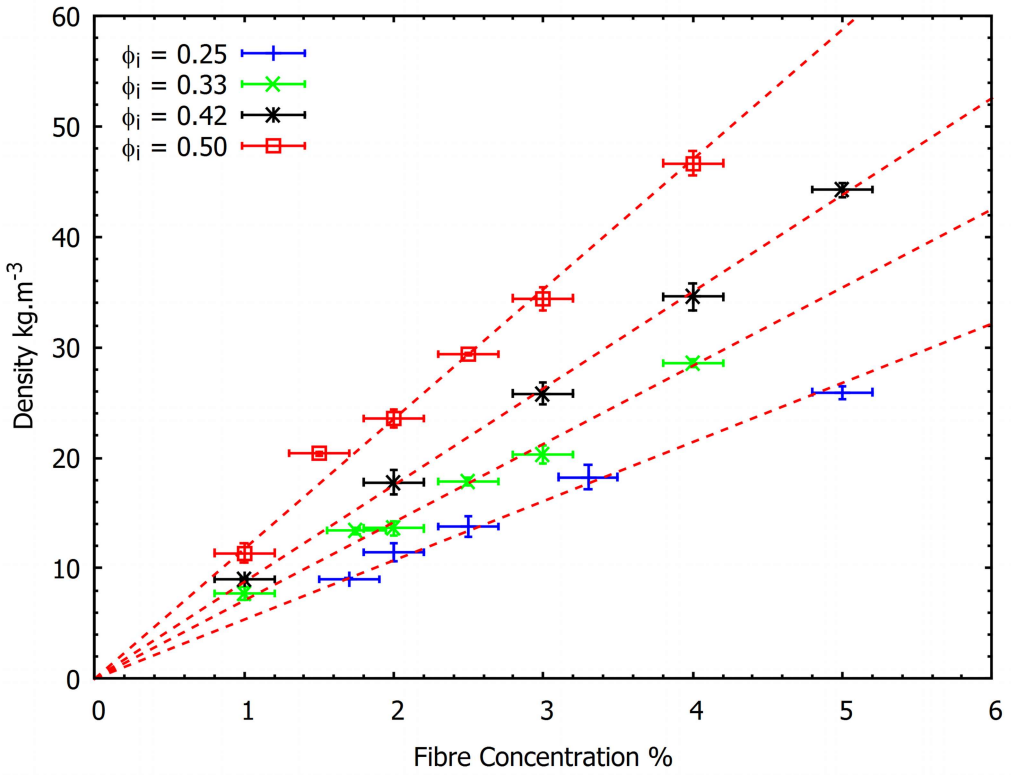

Fig 5.1: Sample density varies linearly with fibre concentration. Each data point represents an average of five samples. The minimum fibre concentration required to produce stable samples was found to be 0.5%, where ϕ_i is 0.25.

The samples were produced as outlined in chapter 3 by varying c and ϕ_i. c ranged from 0% to 5% and ϕ_i ranged from 0.25 to 0.50 as shown in figure 5.1.

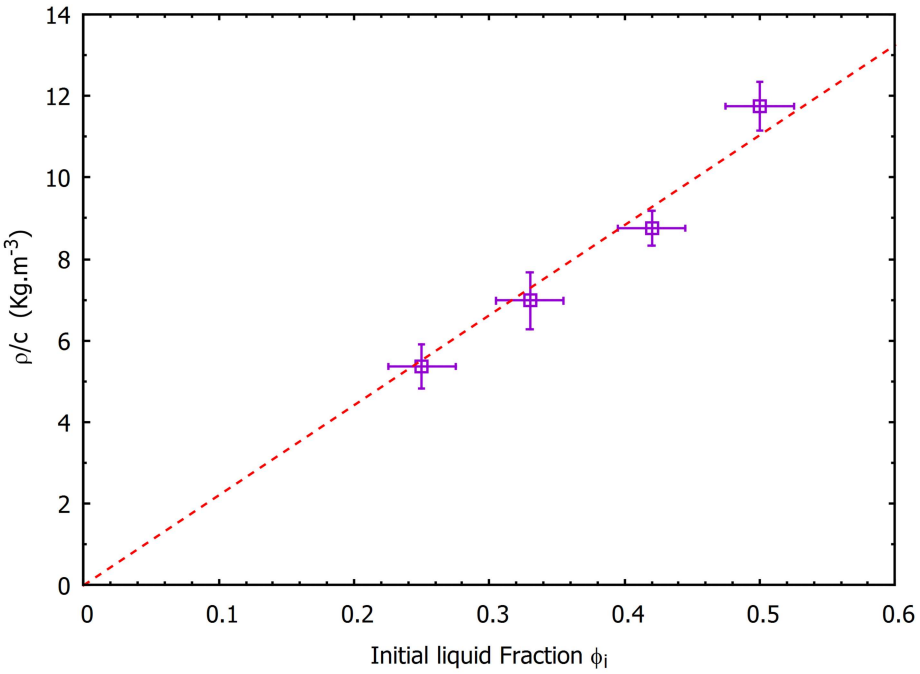

Fig 5.2: An increase in the initial liquid fraction of the dispersions, used to produce the samples, can be seen to increase the linear scaling of sample density with fibre concentration (slopes of plots in figure 5.1).

Sample density was determined prior to performing any mechanical testing by weighing and measuring the dimensions of each of the dry samples. The density ρ was controlled via the fibre concentration c in the aqueous dispersions during sample production, as shown in figure 5.1. The increase is linear in c once above the minimum concentration $c_{crit} \sim 0.25\%$ required for sample stability, found in chapter 4. Each data point is an average of five samples per fibre concentration.

The scaling of sample density with fibre concentration is linearly dependent on ϕ_i, as shown in figure 5.2. The data suggests that if we hold c constant, sample density can be varied by the initial liquid fraction of the dispersions. We can now produce a range of samples with densities that can be controlled via the fibre concentration and liquid fractions of the foam-fibre dispersions. Next, we will investigate the mechanical properties of the samples.

5.2 Compression Testing Method

Fig 5.3: On the left is an image of the rheometer (Anton Paar Physica MCR301) used to measure the compressive response of the samples. The image on the right is a close up of one of the samples placed between the two plates of the rheometer.

The mechanical strength of each of the dry samples was ascertained by subjecting it to uni-axial compression, see figure 5.3. The samples were placed in a rheometer (Anton Paar Physica MCR301) in a plate-plate configuration (plate diameter $50mm$). The upper plate was lowered at a rate of 1mm/min and the resulting stress and strain was measured. All the samples had a contact area of $33x33mm$. Stress-strain curves were obtained by applying an increasing load to the sample and measuring the resulting deformation up to a maximum strain of 0.6. The direction of compression was the same in which the liquid had gravity-drained from the samples during their production (later in section 5.5 we will discuss the results when the samples are compressed from all three axial directions). For each sample density, the tests were carried out four times and the results averaged.

5.3 Stress-Strain Behaviour

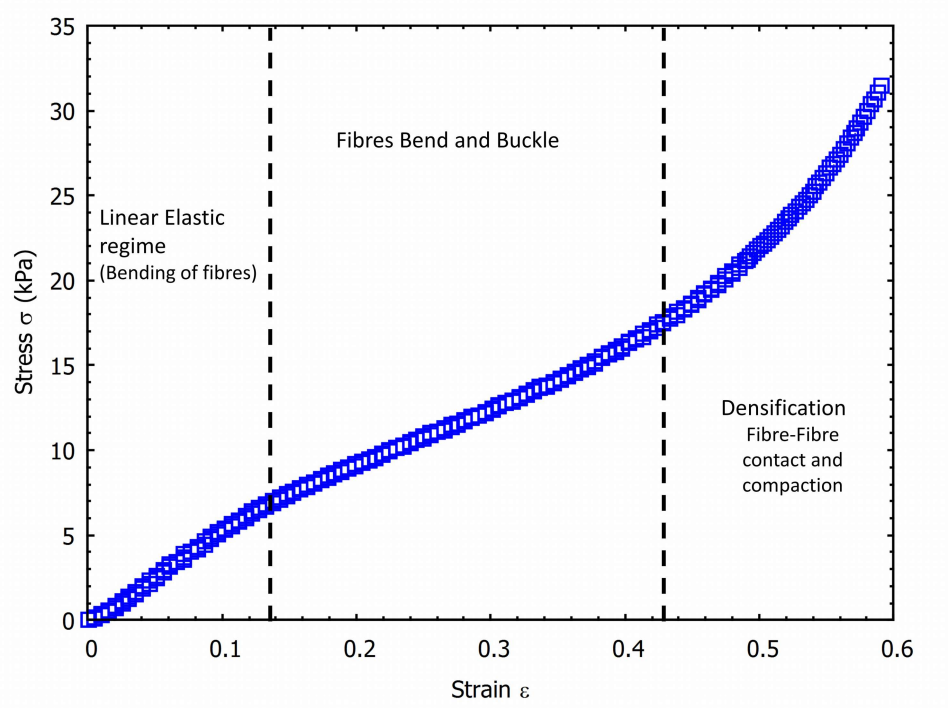

Fig 5.4: Stress-strain behaviour of a lightweight fibrous structure under uniaxial compression. We obtain the compressive modulus of each sample from the initial linear slope. Beyond the initial linear regime, the sample transitions into the plastic, non-recoverable regime, where the fibres begin to buckle. Compressing the sample further leads to the densification regime, represented by the sharp rise in the stress-strain curve. In this regime, the sample becomes compacted and the pores/voids of the structure ultimately close.

Stress, σ, is defined as:

$$\sigma = \frac{F_n}{A} \tag{5.1}$$

Where F_n and A are the normal force and contact area respectively.

As a stress is applied, the resulting strain ε of the sample is defined as:

$$\varepsilon = \frac{\Delta L}{L_o} \tag{5.2}$$

Where ΔL is the change in height and L_o is the initial height of the material.

The compressive modulus of elasticity, E_c is defined as the ratio of the applied stress to the resulting strain. It is a mechanical property, telling

us how the material deforms under compressive loading while in the elastic regime. E_c is defined as

$$E_c = \frac{\sigma}{\varepsilon} \tag{5.3}$$

Figure 5.4 shows the stress-strain curve for one of the samples, produced from a foam-fibre dispersion with ϕ_i= 0.25. Initially, as the sample is compressed, elastic bending of the fibres occurs and the stress-strain response is linear. E_c is given by the slope of this initial linear increase.

Compressing the sample further results in the non-recoverable buckling of fibres. Due to less force being required to initiate their buckling, the longer fibres are the first to buckle. An increasing force is then required to compress the sample further as the remaining non-buckled fibres are shorter and shorter. Euler's formula for the critical force, F_c, required to initiate columnar buckling (equation 5.4) has been applied to fibrous networks to describe their buckling behaviour [90].

$$F_c = \mu \frac{\pi^2 E_c I}{a^2} \tag{5.4}$$

I is the cross-sectional moment of inertia, a is the free-span length of the column and μ is a pre-factor which depends on the boundary conditions at the column ends.

After bending and buckling, the stress-strain response transitions into a densification regime, where an increase in fibre-fibre contacts occur. As a result, a sharp increase in the stress-strain curve can be seen as the sample becomes compacted and the pores/voids of the structure ultimately close.

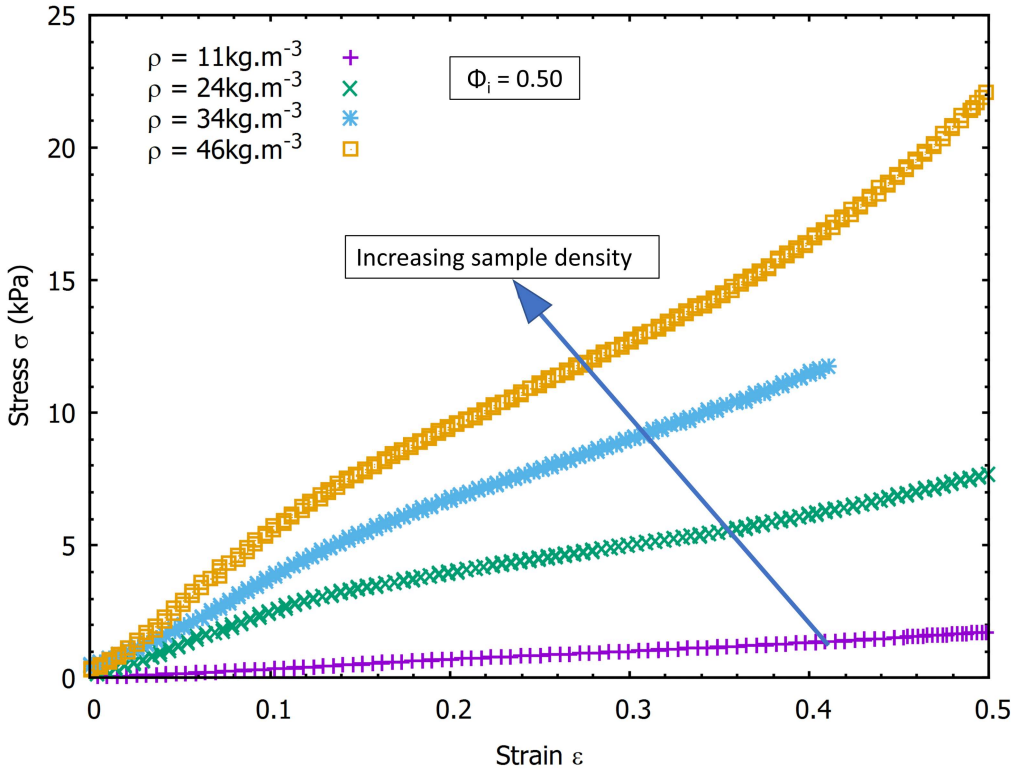

Fig 5.5: The stress-strain behaviour of several samples produced by varying the fibre concentration in the aqueous dispersions. The samples were produced from foam-fibre dispersions with initial liquid fractions of 0.50. The density can be seen to influence the stress-strain response of the samples. The plot above shows one measurement per sample density. We carried out a minimum of four stress-strain tests per sample density.

Figure 5.5 shows the effect of fibre concentration on the stress-strain response of a range of samples. The samples were all made from foam-fibre dispersions where $\phi_i = 0.50$. Increasing c leads to the samples requiring a higher level of stress to reach the same level of strain as those made from a lower fibre concentration.

5.4 Compressive Modulus, Sample Density and Liquid Fraction

s

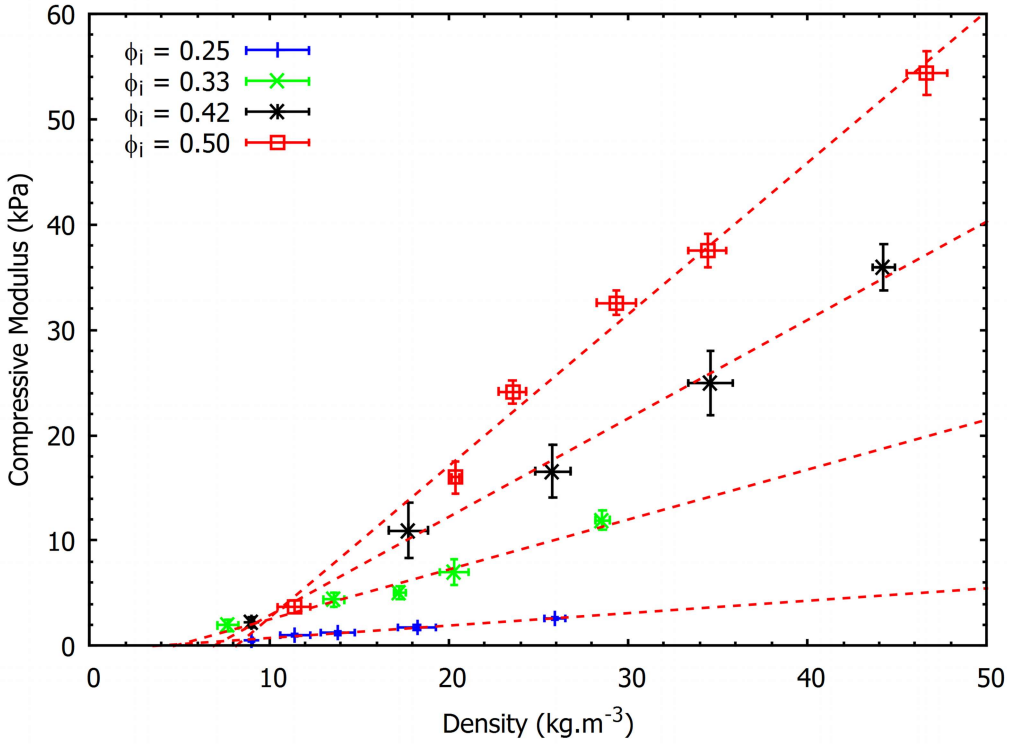

Fig 5.6: The averaged compressive modulus as a function of the average sample density for the samples referred to in figure 5.1. The scaling of E_c with ρ can be seen to be influenced by the initial liquid fraction of the foam-fibre dispersion.

The averaged compressive modulus E_c per sample density ρ for each of the samples referred to in figure 5.1 is shown is figure 5.6. E_c was obtained from the initial linear increase in the stress-strain curves, up to a maximum strain of 0.15. The values of ϕ_i during sample preparation were 0.25, 0.33, 0.42 and 0.50. The contrast in the scaling of E_c with ρ is apparent. A higher ϕ_i, used when producing the samples, can be seen to increase the scaling. An interesting observation that we can draw from this plot, is that it suggests that we can have samples of the same density, but with a variation in E_c. The

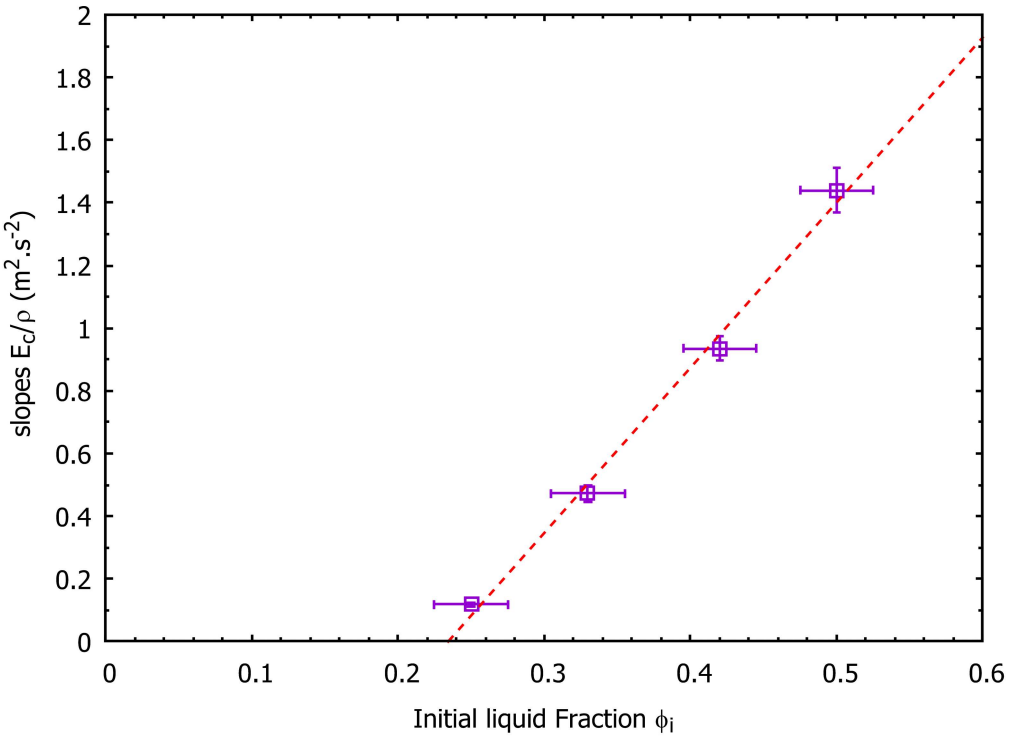

Fig 5.7: The scaling of E_c with sample density as a function of the initial liquid fraction of the foam-fibre dispersions. A higher initial liquid fraction increases the scaling of the samples compressive strength with density.

greater the sample density, the wider the range we can vary E_c through the initial liquid fractions of the foam-fibre dispersions.

The compressive moduli of the samples shown in figure 5.6 ranged from 1 to 55kPa. All the samples were made using Kraft fibres and contained no bonding agents. This contrasts with the values reported by Pohler *et al.* (see figure 1.5) which ranged from 30 to 170kPa. However, Pohler *et al.* used bonding agents and other natural fibre types demonstrating that the compressive strength of the samples can be significantly increased. For instance, their TP5 sample made of Kraft fibres and Polyvinyl Alcohol had a density of 45 $kg.m^{-3}$ and a compressive modulus of 140kPa, while our sample (density of 48$kg.m^{-3}$) had a modulus of just 55kPa.

The scaling of E_c with sample density can be seen to be influenced by the initial liquid fractions, as shown in figure 5.7. Increasing ϕ_i results in an increased slope of E_c with ρ.

5.5 Holding Sample Density Constant

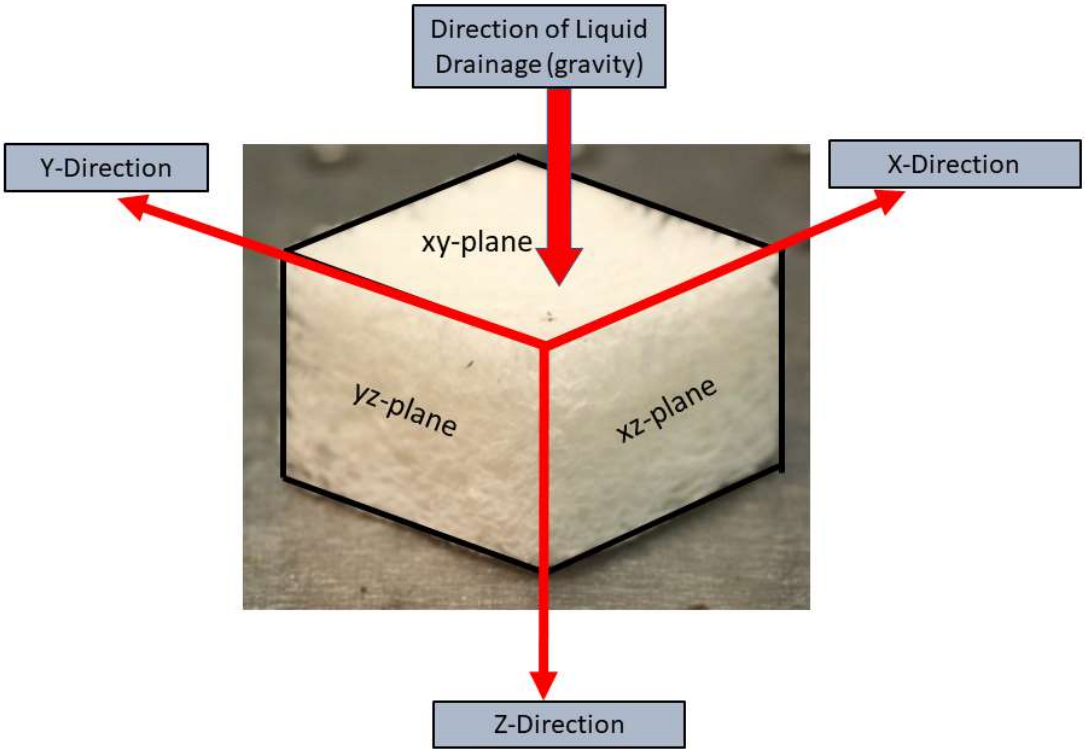

Fig 5.8: The coordinate system referred to in this chapter. The z-direction is the direction in which the liquid drained from the dispersion due to gravity.

In this section we hold sample density at a constant 13 $kg.m^{-3}$ while varying the initial liquid fraction of the foam-fibre dispersions used to produce the lightweight material. Holding ρ contant allows us to focus on the influence of ϕ_i on E_c. Each sample was subjected to uniaxial compression. From the stress-strain response we obtained a value for the compressive modulus of each sample. We also explored the anisotropy of the four samples by measuring

the compressive response from three axial directions. Figure 5.8 shows the co-ordinate system we refer to in the following sections. The z-direction is the direction in which the liquid drained from the precursor foam-fibre dispersion during sample preparation.

5.5.1 Stress-Strain Response Under Uniaxial Compression

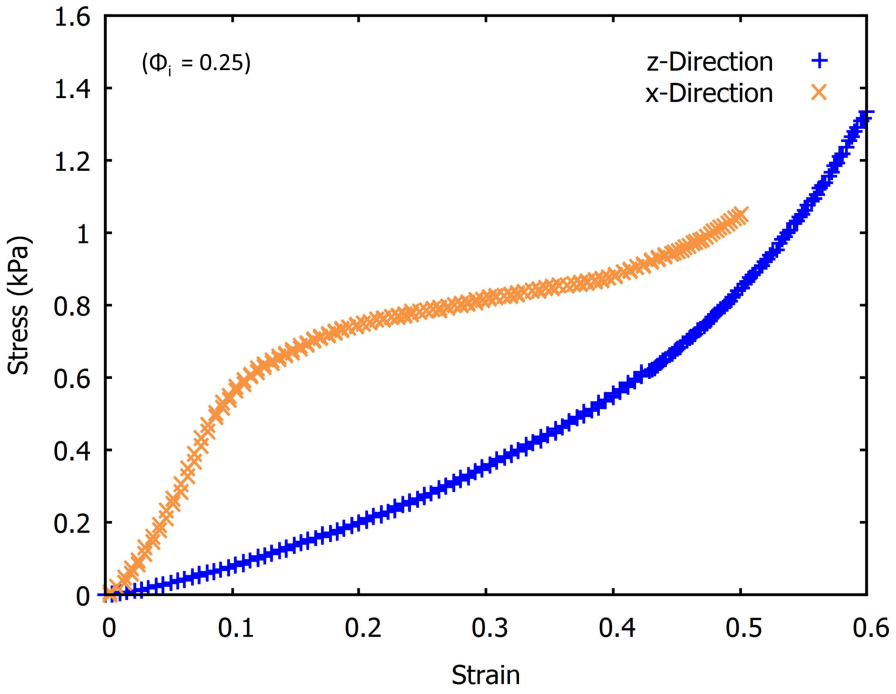

Fig 5.9: The stress-strain response of a sample when compressed from the z and x directions. The sample displays differing stress-strain responses, dependent on the direction of compression. An increased level of stress is required in the x-direction to reach the same level of strain when compressed from the z-direction.

We subjected each sample to uniaxial compression from all three axial directions. A load was applied to the sample and we measured the resulting deformation. Sample size was $33x3x16mm$. When a load was applied in the z-direction (direction of drainage) the contact area was $33x33mm$. When a

load was applied orthogonal to the direction of drainage, the sample was cut beforehand to a height of $16mm$, giving a contact area of $16x33mm$. This was done to ensure the maximum compressible height of all samples was the same (i.e. all samples had a height of $16mm$, regardless of the direction of compression).

Figure 5.9 shows that the stress-strain response of our samples depends crucially on the direction of compression, i.e. the samples are highly anisotropic. Compression from the z-direction features a short initial linear regime (more evident in figure 5.10a), followed by a superlinear increase in stress, leading to densification. When the sample is compressed along the x-direction, the stress-strain curves display three distinct regimes. The first is the linear elastic regime which has a higher modulus compared to the z-direction. Between strains of 0.1 and 0.4, the stress increases more slowly with strain. This is followed by sample densification with an increasing number of fibre-fibre contacts being formed.

The stress-strain curves of four fibrous structures of similar density, but produced with different values of ϕ_i are shown in figure 5.10. For the samples in figure 5.10a, the load was applied in the z-direction (direction in which the liquid drained from the samples during production) and for the samples in figure 5.10b, the load was applied in the x-direction. Applying the load in the x-direction results in a higher value of stress for a given strain when compared to the z-direction.

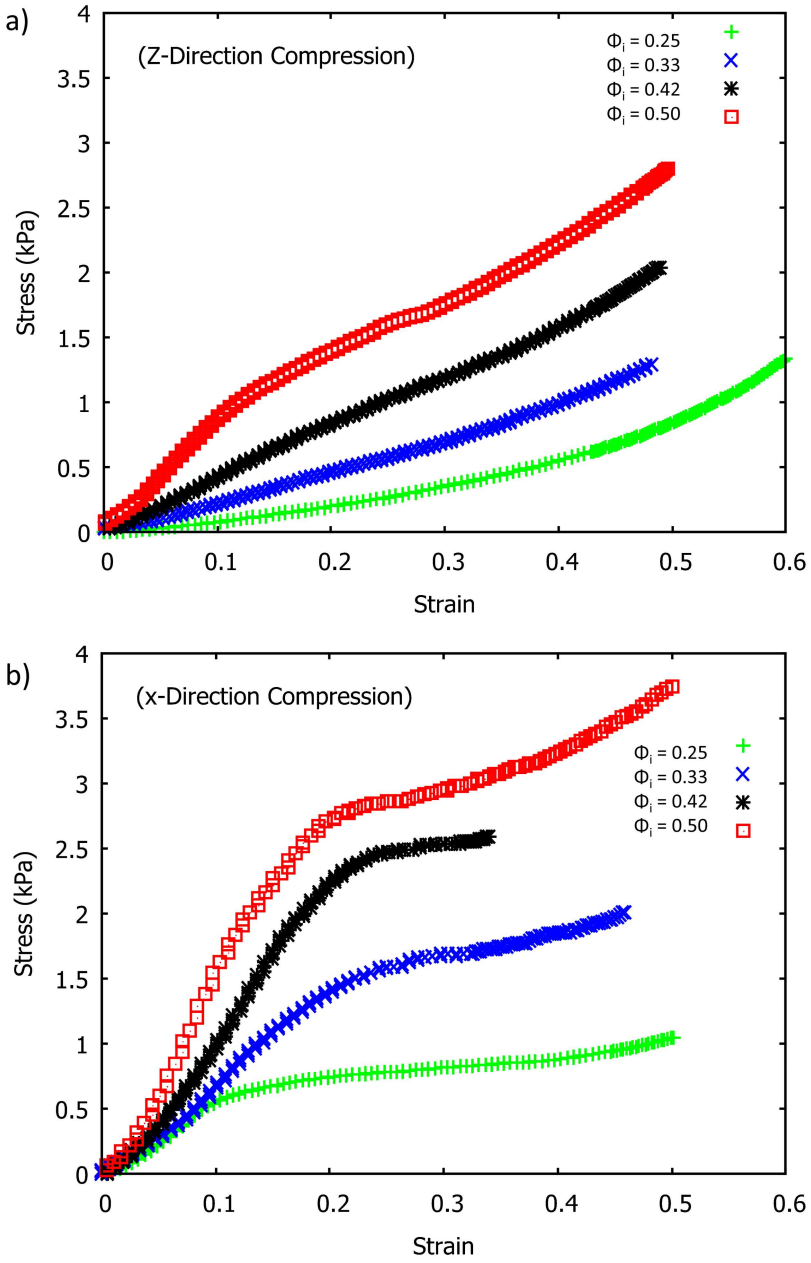

Fig 5.10: Stress-strain response of four fibrous samples to uniaxial compression. All samples had the same density but were made with different values of ϕ_i. a) Application of load in the z-direction (direction of drainage). b) Application of load in the x-direction, orthogonal to drainage. Applying the load in the x-direction results in a higher value of stress for a given strain when compared to the z-direction.

5.5.2 Directional Compression: Exploring Anisotropy

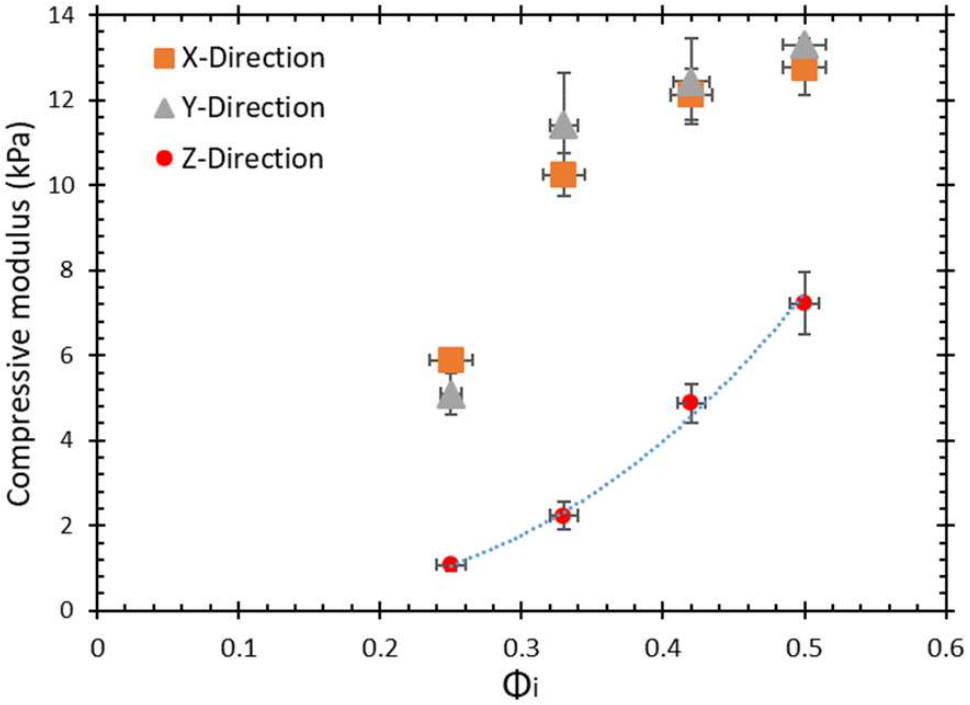

Fig 5.11: Compressive modulus, E_c, obtained from the initial linear regime of figures 5.10a and b. E_c increases with ϕ_i in all three directions. A seven fold increase in E_c with ϕ_i is seen when compressed from the z-direction.

The compressive modulus of elasticity, E_c, was obtained from the initial linear part of the stress-strain curves, up to a maximum deformation of 0.15. Figure 5.11 shows that E_c increased with ϕ_i for all samples, irrespective of the direction of compression. The z-direction shows an increase in E_c by a factor of seven for the same value of ρ. It also shows that E_c is higher in the x and y-directions than the z-direction for each value of ϕ_i. The x and y directions display very similar results, which we will probe further in chapter 6.

5.6 Compressive Modulus and Forced Drainage

Based on our work so far, it is clear that when the volume of liquid that drains through the foam-fibre dispersion is increased (via increasing ϕ_i), this leads to an increase in E_c (figure 5.6). This now raises the question; is it the volume of liquid or the duration over which this volume drains from the foam-fibre dispersions that has the larger effect on E_c? In this section we explore what happens to E_c when we extend the duration of drainage for a fixed liquid fraction and fixed density during the production phase.

Foam drainage occurs along the Plateau borders between the bubbles within the foam (see section 2.2.4). The relationship between liquid fraction and the ratio of the average bubble radius r_b to Plateau border size r_p is described by equation 2.6 in chapter 2 as

$$\phi = c(r_p^2/r_b^2). \tag{2.6}$$

Our bubble size analysis in chapter 4 showed that two foam-fibre dispersions had very similar average bubble sizes, despite having significantly different liquid fractions (ϕ_i of 0.25 and 0.50 respectively). If we assume their size to be identical, we can then hold the bubble radius constant in the equation above, indicating that it is the cross-section of the plateau borders which widen when we increase the liquid fraction of the foam-fibre dispersion. The drainage rate Q is given by equation 2.7, presented in chapter 2 as

$$Q = (\rho g/\eta^*)\phi^2 A l_v^{-1} \tag{2.7}$$

From the above expression we can see that Q is proportional to the square of ϕ. Combining equation 2.6 with 2.7, we see that as ϕ increases, the width of the plateau borders increase to allow for a higher flow rate of liquid to drain through the network, assuming the bubble sizes are unchanged.

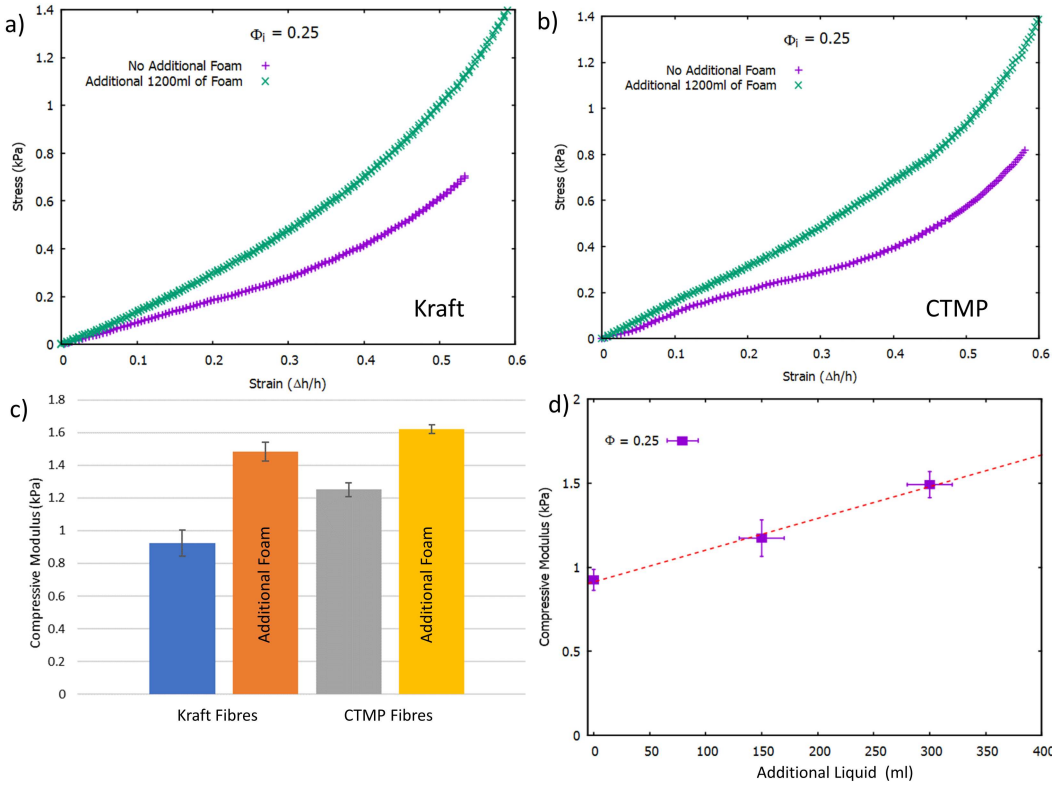

Fig 5.12: a) The stress-strain response of two samples made from Kraft fibres. One sample was made by adding 1200ml of pure foam to the top of the foam-fibre dispersion to increase the duration of drainage. When the duration of drainage was increased, the resulting fibrous sample required an additional level of stress to reach the same level of strain compared to the sample that was made without the additional foam. b) The stress-strain response of two samples made from CTMP. The extra volume of pure foam is also seen to alter the response in a similar manner to the sample made of Kraft fibres. c) Shows the compressive moduli of the samples presented in a and b. The extension of the drainage time can be seen to increase the compressive moduli of the samples. d) The compressive modulus of three samples made of Kraft fibres, extending the duration of liquid drainage through the foam-fibre dispersions can be seen to increase their compressive moduli.

We now look at how extending the duration of drainage affects the fibrous structures by measuring the stress-strain response and determining E_c of the resulting fibrous samples. To increase the drainage time without changing the average liquid fraction, drainage rate or the number of fibres in the dispersion, we poured the foam-fibre dispersion into the drainage vessel and then poured

a pure foam on top, both the foam and foam-fibre dispersion had the same initial liquid fraction. The sample was allowed to drain and dry as previously described. For comparison purposes we also made a fibrous sample without the addition of the extra foam.

Figures 5.12a and b show the stress strain curves of four samples, all made with an initial liquid fraction of 0.25. The samples in the top left figure (a) were made using Kraft fibres while those in the top right figure (b) were made with CTMP fibres. Plots (a) and (b) show the stress-strain behaviour for a sample made with no additional foam added and the behaviour of a sample when 1200ml of foam (300ml of liquid) was immediately poured on top of the foam-fibre dispersion during sample production.

The samples made from CTMP fibres are seen to require an additional level of force to reach the same level of strain as the samples made from Kraft fibres. This can be attributed to the increased lignin content of the CTMP fibres, resulting in a stiffer fibre as well as the average length of the CTMP fibre being shorter (1.6mm) [12] than the Kraft fibres (2.0mm), thereby reducing the mean free span of the network.

However, in both cases (Kraft and CTMP fibres) the data sets show that where the duration of drainage was extended (green data sets), the stress required to reach a given level of strain was greater than when the duration was not extended (purple data sets). For instance, when the drainage was extended in both the CTMP and Kraft samples, an additional $\approx 60\%$ increase in the applied stress was required to reach a strain of 0.3. Figure 5.12c shows that the compressive modulus increased when the duration of drainage was increased during the production of the fibrous samples.

Figure 5.12d shows the average compressive modulus of three Kraft samples as a function of additional liquid volume that drained through the dispersions. The x-axis represents the additional volume of liquid that drained through the dispersions. The increase in the compressive modulus is clearly

visible (y-axis).

We have shown that we can increase compression strength by extending the duration of the drainage. However, we found it was not as effective as increasing the initial liquid fraction of the foam-fibre dispersion. For instance, the sample that had the largest volume of liquid draining through the dispersion (300ml + an additional 300ml) had a compressive modulus of $1.5kPa$. However, the total volume of liquid that drained from this dispersion was the same as that of samples made with initial liquid fractions of 0.50. From the fits to the data in figure 5.6, if we make a sample of the same density as those in figure 5.12d ($13kg.m^{-3}$) using a foam-fibre dispersion of $\phi_i = 0.50$, it would have a compressive modulus of almost $8kPa$ (more than 5 times the compressive strength), indicating that the volume of liquid that drains through the sample is not the only contributing factor to the structure's compressive strength. Another, more important contributing factor could be that the plateau borders are initially much wider when ϕ_i is increased, allowing for a higher rate of drainage, this in turn may orientate more fibres in the direction of liquid drainage. This is explored in chapter 6.

5.7 Compressive Modulus and Fibre Length

The mean free span in a fibre network is defined as the mean distance between fibre-fibre contacts, per fibre length. We explored the average fibre length and the effect this might have on the mean free span and ultimately the compressive strength of the fibrous materials made from foam-fibre dispersions.

An expression for the mean free span of random fibre networks was derived by Van Wyke in 1946 , when he investigated the compressibility of wool [91] and again by Komori and Makishima in 1977 [92]. Both arrived at very similar expressions, demonstrating that it is the total fibre length in the volume under investigation and not the individual fibre length, that influences the mean free

span, a_o.

Van Wyke arrived at the following expression for the mean free span for a single fibre:

$$a_o = 2V/(\pi DL) \tag{5.5}$$

Where V is the volume of the network, D is the fibre diameter and L is the total fibre length in the volume.

Komori and Makishima derived the following:

$$a_o = V/(2DLI) \tag{5.6}$$

Where I is a constant that takes into account the spatial arrangement of the fibres.

As we can see, both expressions are very similar. The total fibre length, fibre diameter and the volume under consideration determines the mean free span of the network.

We produced a range of samples from a mixture of Kraft and viscose fibres in a 1:2 ratio respectively. Viscose fibres were used as they are supplied in well defined lengths allowing us to control the average fibre length in the samples. The viscose fibres contain no fibrils to interlock (see figure 3.2 in chapter 3), nor do they form fibre-fibre bonds. As a result, fibrous samples made purely of viscose and without a bonding agent were prone to collapse. As the Kraft fibres have already been shown to form strong fibre-fibre bonds, we included them to aid in bonding the fibre network together. We varied the length of the viscose fibres while holding the total mass and volume of fibres constant.

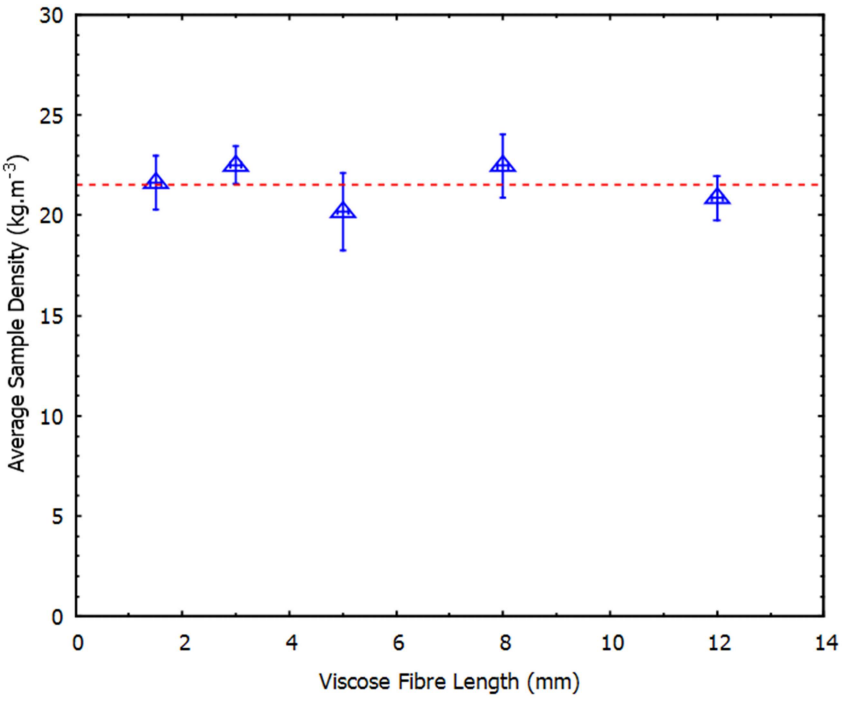

Fig 5.13: The average density of five samples made from a mixture of Kraft and viscose fibres in the ratio of 1:2. Viscose fibre length ranged from 1.5 to 12 mm. The average length of the Kraft fibres was $\approx 2mm$. All samples were of a similar density.

Five different lengths of viscose fibres (1.5, 3, 5, 8 and 12 mm respectively) were used during preparation to create the fibrous samples. We then measured the density of each sample and all were found to be in the region of 20-22$kg.m^{-3}$(see figure 5.13). The samples were subjected to uniaxial compression testing in the z-direction (direction of drainage). From their stress-strain response we evaluated the compressive modulus of each sample and took an average of four results per sample. Figure 5.14 shows that as the average fibre length was increased, the compressive strength of the samples decreased. The trend of the decrease of E_c with fibre length is described by an exponential decay function, indicated by the red dashed line.

An explanation for the decrease in E_c with fibre length may come from a study that was carried out by Heindel and Garner [93]. They investigated the effect of fibre length on the bubble size in aqueous fibre suspensions and

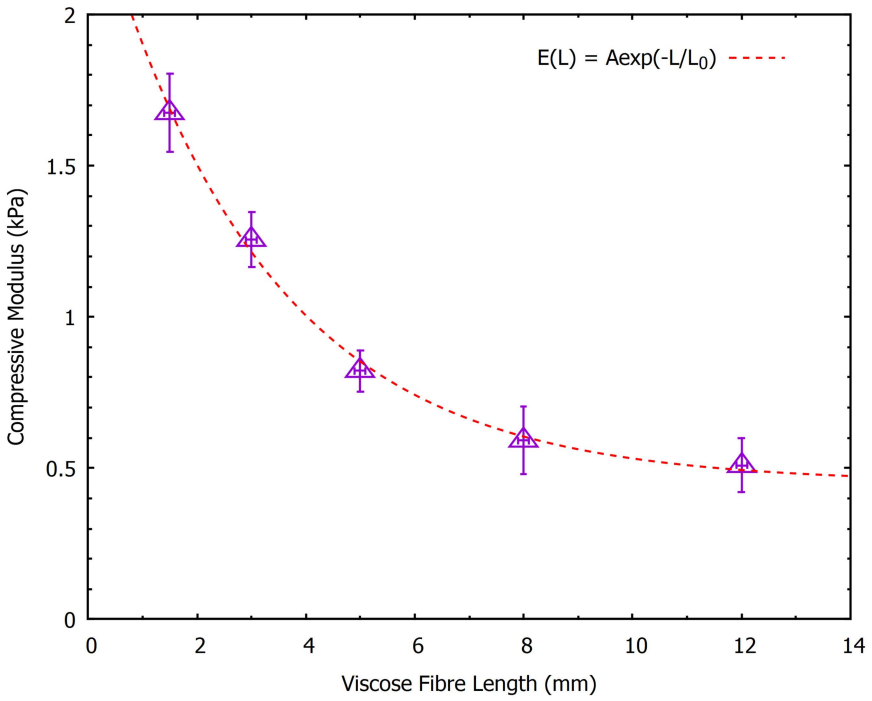

Fig 5.14: Compressive modulus as a function of viscose fibre length. Each data point is an average of four compression tests. The trend of E_c is described by an exponential decay function as indicated by the red dashed line.

found that where longer fibres are used, there is an increased number of larger bubbles. While their method of creating bubbles (blowing air from the bottom of a cylinder through small orifices) is not the same as the shearing method employed in this thesis, assuming the outcome to be similar, it provides an explanation for the observed behaviour. If the average bubble size increases with fibre length, then the resulting voids in the lightweight material will be larger. This could have the effect of increasing the mean free span of the network, which decreases the structure's compressive strength.

5.8 Conclusions

Our material and mechanical analysis of the samples shows just how versatile the foam-forming technique can be when creating lightweight fibrous struc-

tures. The sample density and compressive strength of the material can be controlled via the fibre concentrations and liquid fractions of the dispersions during production. Fibre length and duration of drainage were also found to influence the compressive modulus of the material. Increasing the duration of drainage leads to an increase in E_c. However, this is not as effective as increasing ϕ_i, suggesting the Plateau border to bubble size ratio have a greater influence on E_c. The increased flow rate through the wider Platau borders may orientate more fibres into the direction of drainage. We will explore the effect of ϕ_i on the orientation distribution of the fibres in chapter 6.

We found that sample density scaled linearly with fibre concentration and compressive modulus. We showed both scalings to be highly sensitive to the initial liquid fractions of the foam-fibre dispersions. Compression along the z-direction required a continual increase in stress through the buckling regime, indicative of the fibre length distributions within the samples. Longer fibres buckle first followed by the shorter fibres which require additional levels of stress to buckle.

The samples are highly anisotropic in their response to uniaxial compression. A higher level of stress is required when the sample is compressed along the x or y-direction to reach the same strain as when compressed along the z-direction. The contrasting buckling regimes exhibited by the samples, being dependent on the direction of compression, suggests the fibres within the samples have a preferred orientation. The buckling regime of the x and y-directions features a plateau where the stress increases much slower with strain than in the first regime before transitioning into densification. We offer an explanation to this in the next chapter where we explore the orientation distributions of the fibres through μCT scanning of the four samples presented above.

Chapter 6

X-ray Tomography and Analysis of Lightweight Fibrous Material

6.1 X-ray Tomography

We have imaged the four same density fibrous samples presented in the previous chapter, where we investigated their mechanical strength, and subsequently performed a fibre orientation analysis. μCT scanning was used to probe the internal structure non-invasively. X-ray image acquisition was performed with a Nikon XTH 225 ST device, fitted with a reflection target. Our initial scans revealed that our samples had low X-ray attenuation due to the high porosity/ low density of the material. To obtain high contrast images, we used Molybdenum as the target material, along with a low electron beam energy (45kV) and a beam current of 200mA. Molybdenum produces low energy X-rays resulting in greater beam attenuation.

Prior to imaging, the fibrous samples were placed in sealed glass containers with a small quantity of iodine crystals. At room temperature, the iodine crystals sublimate and after approximately four to five days, the iodine vapour that penetrated throughout the porous fibre network leaves an iodine coating on the fibres. This increases the atomic density of the fibres, vastly

increasing beam attenuation [94]. The broader spread in the X-rays having passed through the sample gives rise to higher contrast images, allowing for the detection of individual fibres.

Samples were placed onto a stage located between the target material and a flat panel detector (Varex 1620). The ratio of the distance between the detector and the source, and the source to the sample gave a geometric magnification of 19.7. The resulting effective pixel size determined by the actual pixel size/ geometric magnification was 10μm. Pixel size of the detector was 200μm set in a 2000 x 2000 pixel matrix. The flat panel detector consisted of a layer of scintillator on top of an array of photosensitive diodes. As the X-ray energies are absorbed by the scintillator they are then re-emitted as visible light, which is detected by the photo-diodes and converted into greyscale images. The sample stage rotates in increments (dependent on the number of X-ray images required) through 360 degrees while X-ray images are obtained, an example is shown in figure 6.1.

For our scans, the sample stage was rotated in 0.115 degree increments in a stop-start fashion. 3,141 X-ray images of each sample were obtained, with an exposure time of 500 milliseconds per image projection and 4 frames per projection, resulting in a total acquisition time of around 90 minutes.

After acquiring the X-ray images, the files were then reconstructed into a volume with Nikon's CT Pro 3D software using a back-filtered projection algorithm, with a voxel resolution of 10 μm (fibre diameter of approximately 35 μm). The files were then imported into the visualisation and analysis software, Volume Graphics Studio Max [95].

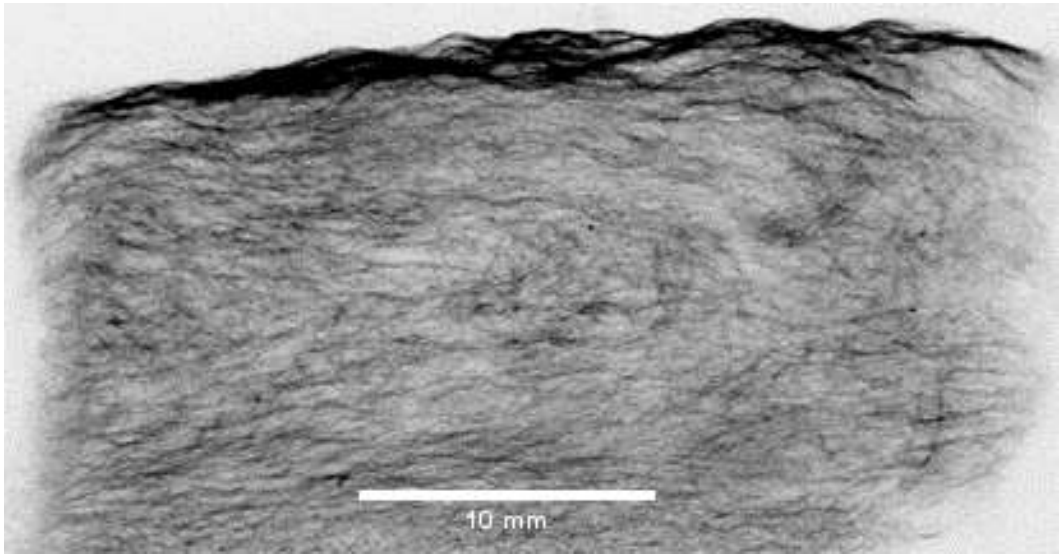

Fig 6.1: One of 3,141 X-ray images used to reconstruct three orthogonal image stacks, as well as three dimensional renderings of the samples. The low beam attenuation of the samples was increased prior to any imaging by coating the individual fibres using an iodine sublimation process.

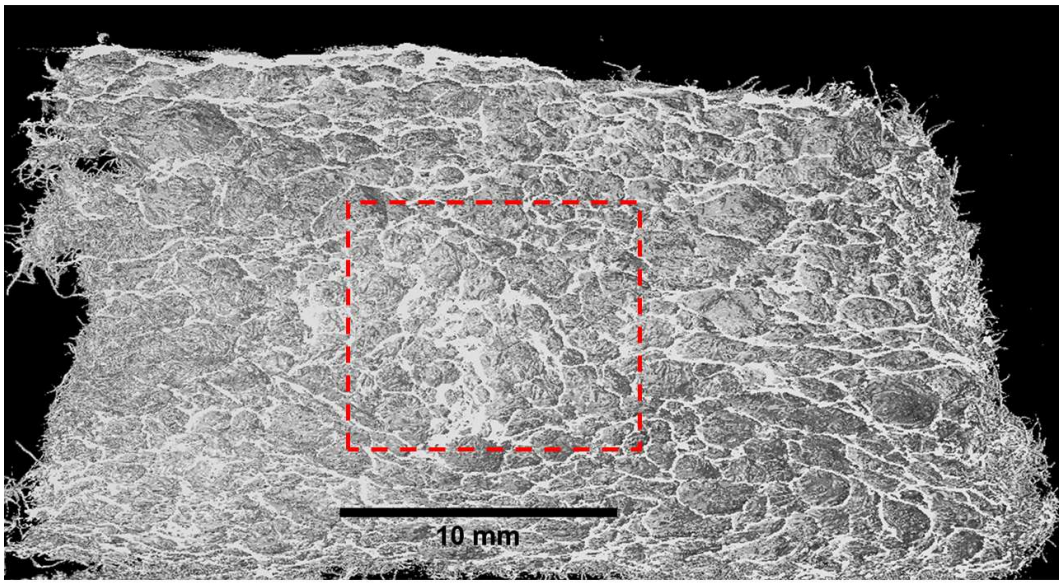

Fig 6.2: A reconstructed rendering of one of the lightweight foam-formed fibrous materials. The red-dashed square represents the cube size our analysis was performed on ($10mm$ edge length). The front half of the structure has been removed using software manipulation, revealing the internal fibre network and void spacing of the material.

The software allows a visualisation of the volume in three dimensions. Voxel grey values are presented in a histogram that displays two distinct peaks, one peak represents the background value and the other is the greyscale value of the material (fibres). Image contrast is adjusted using the opacity curve tool on the histogram, enabling the fibres to become more visible when rendering the volumes. The fibre surface was determined using Volume Graphics Surface Determination tool. First the background is defined by selecting a part of the image which is clearly the background (above the sample). Next, the material surface is determined by highlighting an area on the fibre. The software then thresholds the volume and displays a 3D rendering for visualisation. The 3D rendering is then visually inspected by rotating and zooming through (fly through) the volume to check that the thresholding has not removed any of the connecting fibres or left behind any artefacts.

Three orthogonal 2D image stacks of the volumes were then exported for analysis as Volume Graphic Studio's 3D orientation module was unavailable. The image stacks represent cross sectional images of the samples, sliced along three orthogonal axis. Before any analysis was carried out, the images were cropped to remove any edge effects that may have occurred when cutting the sample to size. We also excluded the very top and bottom of the sample. As a result, we probed a cube (10mm in length) from each sample centre (see figure 6.2).

For visualisation purposes, a three-dimensional rendered image was also obtained from the data. Figure 6.2 shows one of the samples where the front half has been removed via software manipulation. The clear visibility of the individual fibres enables us to both analyse sample porosity (section 6.3) and fibre orientation (section 6.4).

6.2 Density Profiles

Our first analysis of the orthogonal image stacks concerned the computation of the density profiles of the structure from each axial direction, e.g. the z-direction refers to the images that lie in the xy-plane. We analysed 200 regularly spaced images (spacing 0.05 mm) from each image stack. Images were cropped to size (10 x 10mm) and then binarized using the isodata method and global thresholding applied (see inset of figure 6.3), after which the fibre area fractions were obtained for each image.

The isodata method of thresholding is an iterative process whereby a greyscale image is divided into an object and background by taking an initial threshold. The average of the pixels greyscale values both above and below the threshold are computed. Then the threshold, t is incremented and the process is repeated until the threshold is larger than the composite average [96]. The threshold t is determined as:

$$t_{i+1} = \frac{A_{below}(t) + A_{above}(t)}{2} \tag{6.1}$$

A_{below} and A_{above} are the average greyscale values below and above the threshold.

In figure 6.3 the white pixels represent the fibres and the black represent the void space. The fibre area fraction, A_f, is defined as the ratio of the number of white pixels to the total pixel number.

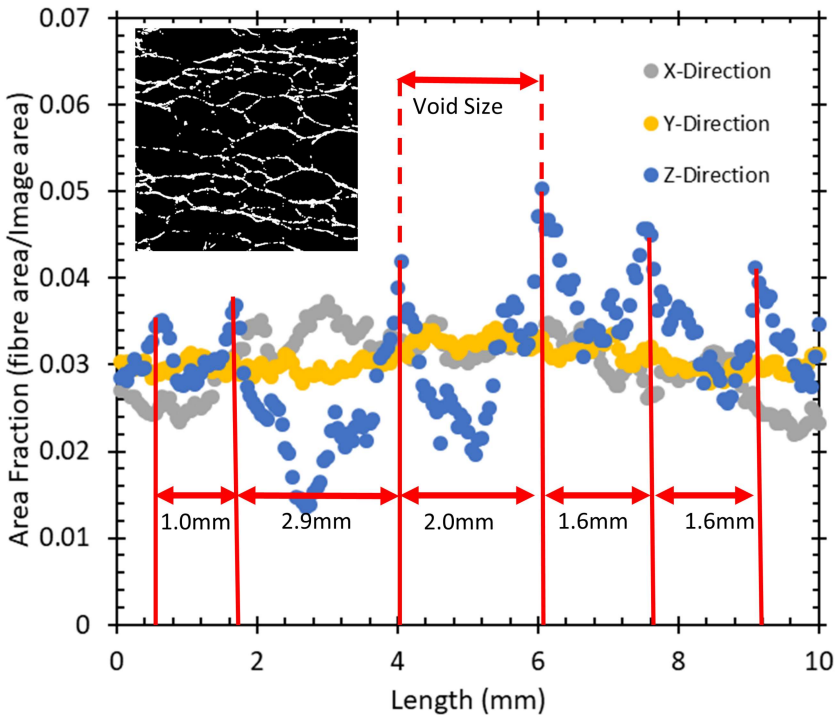

Fig 6.3: Density profiles of one of our foam-formed fibrous samples. Plotted is the fibre area fraction as a function of distance through the sample in mm. The x and y-directions display an approximately uniform density profile throughout the sample. The oscillations in the z-direction indicates layering of the fibres (see image in inset). The majority of the fibres were found to lie in the xy-plane (horizontal) with the remainder of the fibres supporting these layers. The inset shows the fibre layers in the binarized image of a vertical sample slice.

Figure 6.3 shows the fibre area fractions along a sample in the three orthogonal directions x,y,z. While the profiles along the x and y-directions appear roughly uniform, the z-direction reveals a number of sharp peaks and troughs. These are indicative of layering of fibres with a spacing of about 1.8 $\pm$ 0.2mm. We provide a reasoning for the layering in the conclusion/discussion at the end of this chapter.

6.3 Void and Bubble Size Analysis

How does the Sauter Mean bubble Radius of 0.45mm in the foam-fibre dispersion (found where coarsening has been arrested due to the presence of fibres in Chapter 4, figure 4.7) compare with the average pore size in the resulting foam-formed dried material? In order to investigate this we carried out a pore size analysis using our X-ray data of two fibrous samples (density $13kg.m^{-3}$) created from foam-fibre dispersions with initial liquid fractions of ϕ_i=0.25 and ϕ_i=0.50. To make a comparison between bubble and void size, we define void size as the radius of a sphere having the equivalent cross-sectional area, as presumably the bubbles were also deformed under the weight of the fibres and are not spherical.

The analysis was performed on twenty images, taken from the x-direction, for each sample (image spacing: 0.5 mm). Images were first binarized (isodata method with global thresholding applied). Since the fibrous material forms an open cell structure, the voids were manually closed by closing gaps in the fibres surrounding the pores with their nearest neighbours. A particle area size analysis was performed on each image using ImageJ's particle analysis function.

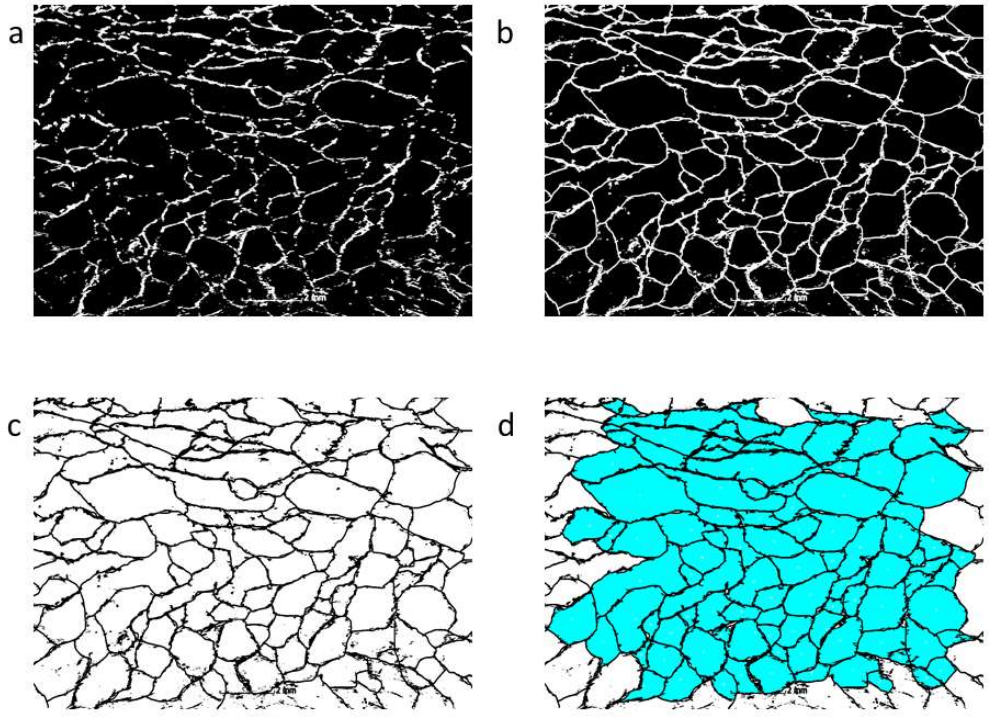

Fig 6.4: One of the images viewed from the x-direction that was used to perform a void size analysis. a) A single binarized image slice of one sample b) Pores are manually closed by connecting gaps between fibres in close contact with each other. c) Inverted image prior to performing area analysis. d) Area analysis output from the ImageJ particle analysis function. Pore area along the image edges is excluded from the analysis.

The total number of voids analysed was almost 2,000 per sample. We express the size of a void in terms of the radius of a circle with the same area as the cross-section of the void. In general the result is different from a three dimensional void size distribution. However, the 2D analysis is sufficient to compare different samples. Moreover, the average void size will be of the same order of magnitude in both 2D and 3D. Figure 6.4 shows the workflow for one image.

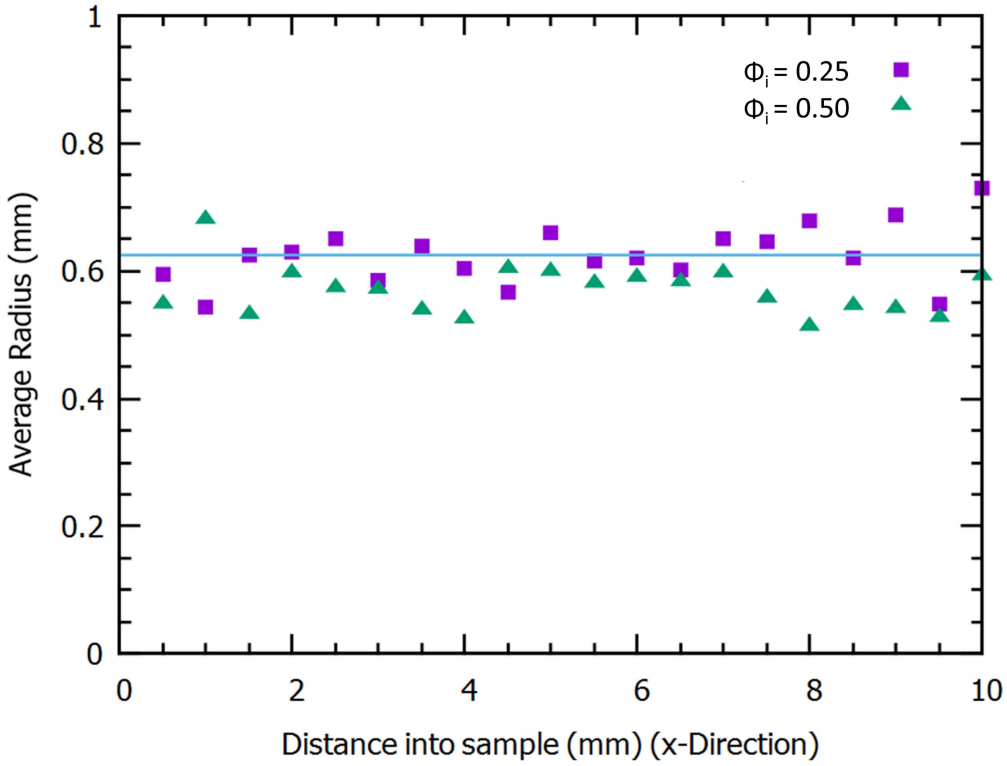

Fig 6.5: Average void radius, measured along the x-direction of two foam-formed samples produced for $\phi_i = 0.25$ and 0.50. The average void size is approximately 1.5 times larger than the average bubble size of the foam-fibre dispersion used to create the sample.

Figure 6.5 shows that the average void size, measured along the x-direction, is roughly constant. Its value (r_v=0.6±0.2 mm) is also independent of the value of initial liquid fraction. Average void size thus exceeds the average bubble size by approximately 50%, as determined in the regime where foam coarsening is arrested by the presence of fibres. Bubble coalescence during the drying process may explain the larger void size.

We also compiled the respective distributions of both void and bubble size, see figure 6.6. The bubble size distributions were obtained from the coarsening arrested regime in figure 4.7. Both are well described by log-normal distributions.

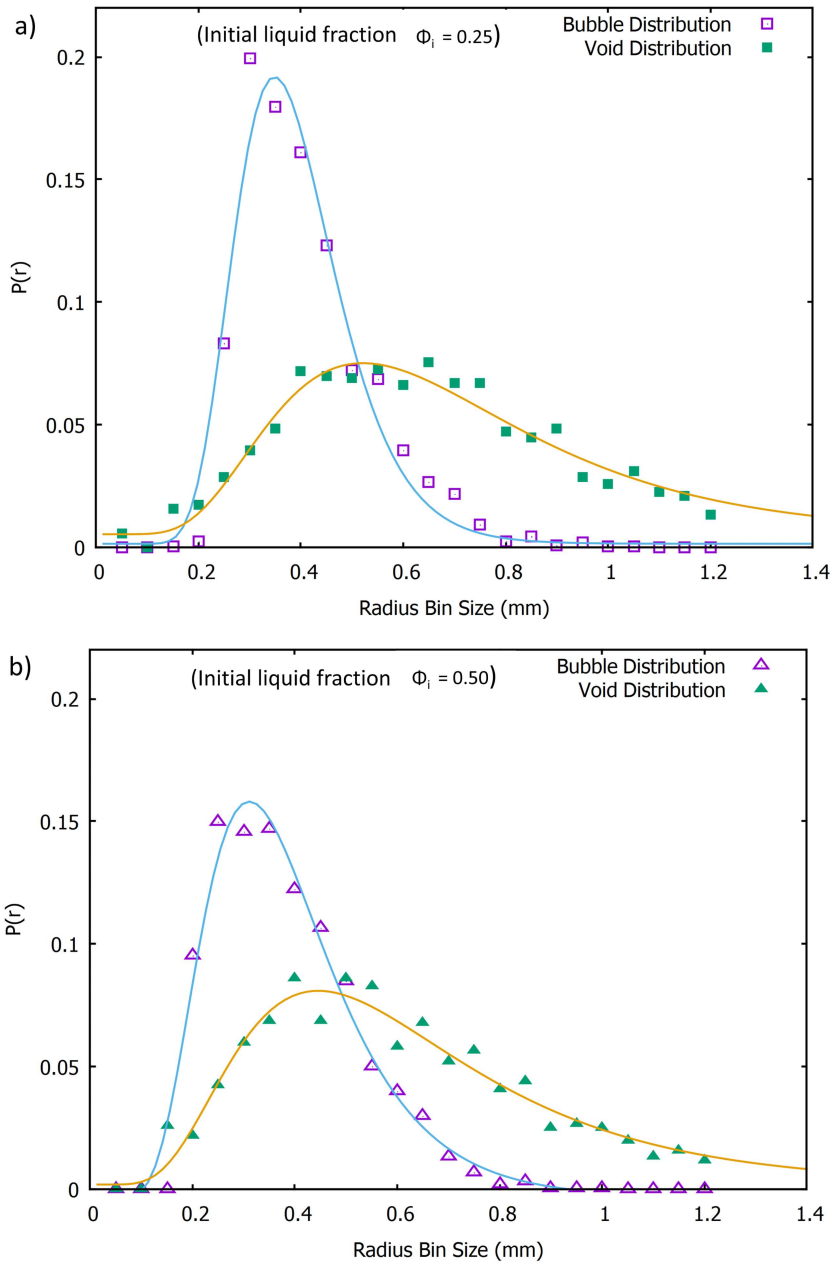

Fig 6.6: Bubble and void radii distributions for the samples made with initial liquid fraction a) $\phi_i = 0.25$. b) $\phi_i = 0.50$. Solid lines are fits to log-normal distributions.

Average bubble size in the coarsening-arrested foam-fibre dispersion (figure 4.7) has thus emerged as controlling the average pore size of the fibrous networks.

6.4 Fibre Orientation Analysis

In chapter 5 we showed that the initial liquid fraction plays a role in determining the compressive modulus of the fibre networks. Now we will demonstrate using our X-ray data, that this is due to its effect on fibre orientation. Fibre orientation analysis was carried out for four similar density samples, produced from foam-fibre dispersions with four different values for ϕ_i (0.25, 0.33, 0.42, 0.50).

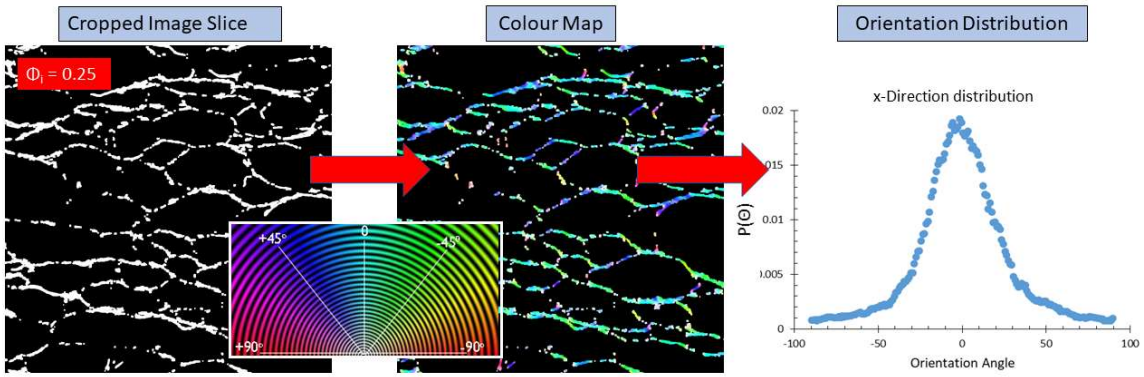

Fig 6.7: Schematic of OrientationJ's workflow for a cropped image slice obtained from a sample produced with ϕ_i=0.25. The algorithm returns a colour map, as well as an orientation distribution for each image. The colour wheel in the centre shows the colours assigned to each orientation angle in the colour maps, the 0° angle being perpendicular to the direction of gravity and drainage.

The fibre orientation analysis was performed on image stacks of the samples (obtained by CT scanning) with the ImageJ/Fiji plugin OrientationJ [97]. Each image stack contained 200 cropped images ($10x10mm$ see figure 6.2), separated by a spacing of 0.05mm. This equates to a total distance through the sample of 10mm. OrientationJ is specifically designed to analyse the isotropic and orientational properties of a 2D image. The plugin computes a histogram of orientation distributions for each image (in our case 200 images per direction per sample), see figure 6.7 for a schematic of the workflow, and Appendix C for details of the algorithm. The resultant orientation distribution $P(\theta)$ is a 2D projection of the fibre orientations.

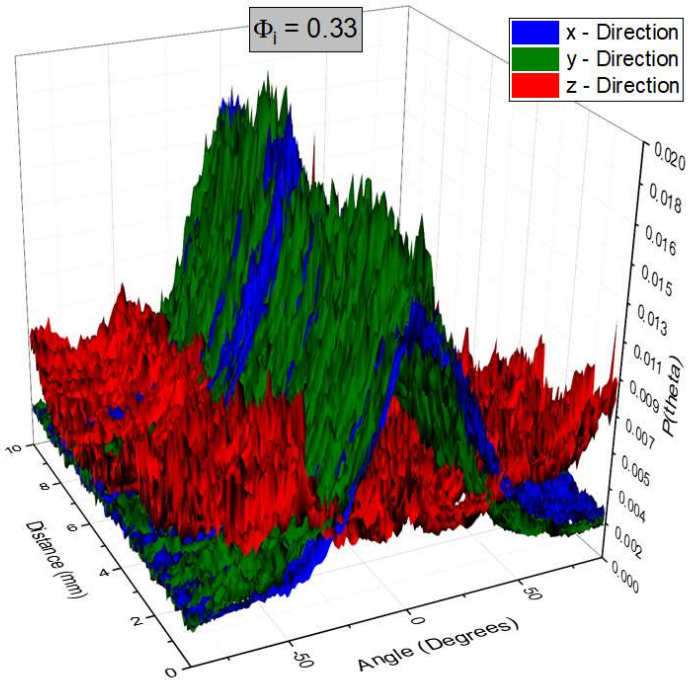

Fig 6.8: Fibre orientation distributions for a sample made from a foam-fibre dispersion with $\phi_i = 0.33$. The angle in degrees, ranging from -90° to +90°, is shown on the x-axis. Distance (depth within the sample) is shown on the y-axis. The normalised counts are represented on the z-axis. The distributions in the x and y-directions (blue and green data sets) are seen to have one dominant peak through the sample located at angle zero, indicating the layering of fibres. No dominant direction is revealed when probing from the z-direction (red data set).

Figure 6.8 shows three fibre orientation distributions (along the x, y and z-directions) for a sample produced with ϕ_i=0.33. The distributions along both the x and y-directions feature a distinct peak at angle zero throughout the sample, corresponding to a fibre orientation perpendicular to the direction of gravity. This corresponds to the majority of fibres lying in the xy-plane. The red data set represents the distributions along the z-direction (xy-plane). Unlike the x and y-directions, no single dominant direction was observed.

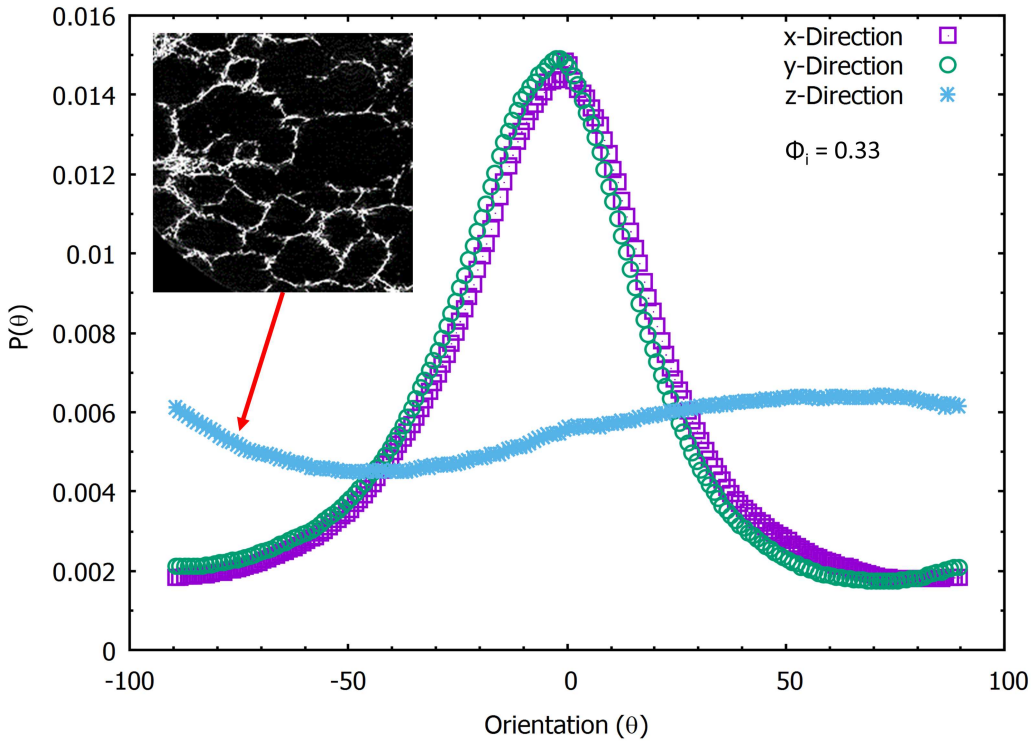

Fig 6.9: The averaged fibre orientations for the 3 directions. The views from both x and y-directions display a single dominant angle at zero degrees and very similar widths, indicating a preferred fibre alignment in the horizontal plane, perpendicular to drainage. The distribution along the z-direction is nearly flat. Any small variation with angle is due to finite size sampling. The inset shows the cell-like arrangement of the fibres in an image slice from the z-direction.

We also averaged the distributions of all the image slices in figure 6.8 along the 3 directions as shown in figure 6.9. The distributions shown from both the x and y-directions are similar due to symmetry and feature a peak at angle zero, corresponding to horizontal orientation of the fibres. Viewing the sample from the z-direction results in nearly flat distribution indicating no preferred fibre alignment in the horizontal plane.

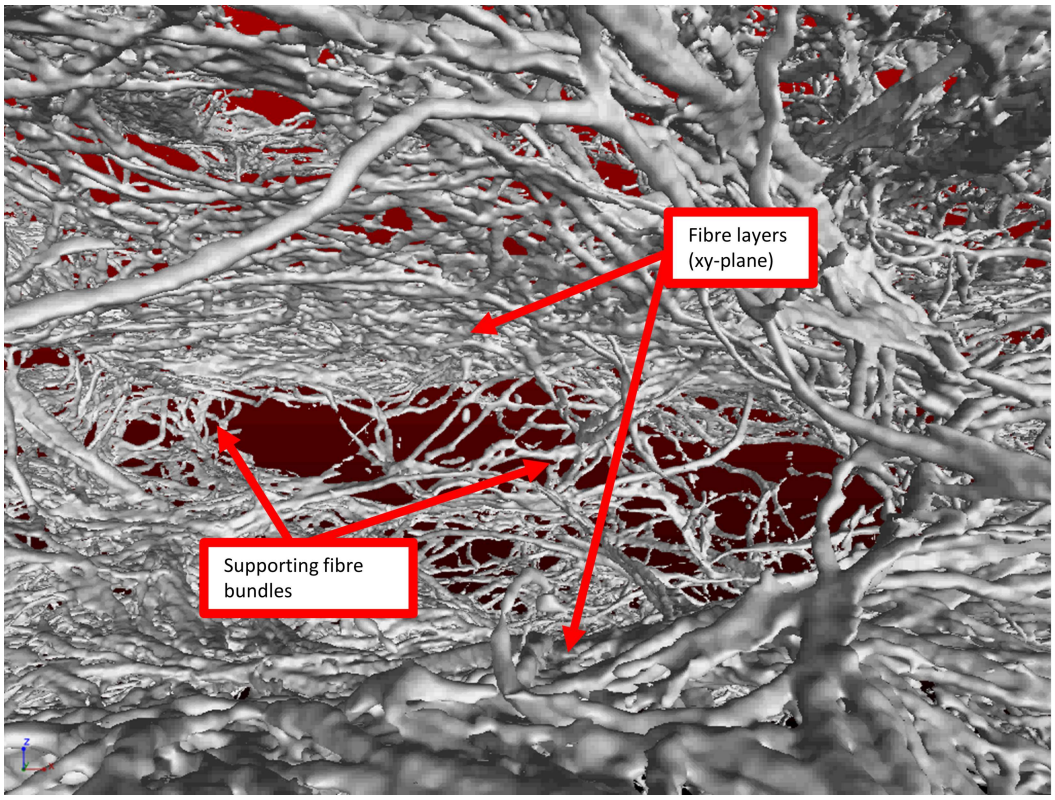

Fig 6.10: Reconstructed view from inside one of the voids within a sample. The image shows two fibre layers, orientated in the xy-plane being supported and kept apart by fibre bundles. When compressing the sample along the z-direction it is these fibre bundles which distribute the load onto the layers. The fibres have an average length of 2.0±0.1mm and diameter of 35μm.

The layering of the fibres in the xy-plane can be observed in a full 3D rendering of the X-ray data, see figure 6.10. The image was reconstructed by Volume Graphics 3D software, it gives a view from inside one of the samples. Two fibre layers can be seen to be supported by fibre bundles. During compression from the z-direction it is these fibre bundles which distribute the load onto the layers. It also indicates a flattening of the voids, following the partial sample collapse. Bundles of fibres as well as the individual fibres are clearly visible.

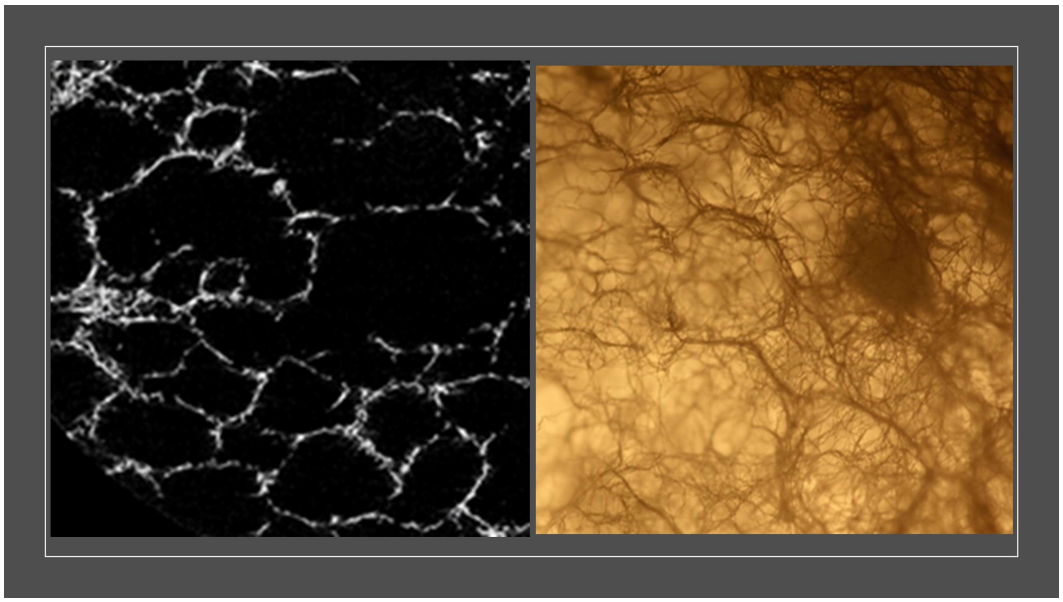

Fig 6.11: Two images of a lightweight fibrous sample. On the left is an image from the z-direction image stack, obtained by CT scanning. The image on the right is a photograph taken from the z-direction with a backlight applied to the sample. The fibre network can be seen to resemble the structure of a dry foam.

On the left of figure 6.11 is a CT image slice of a lightweight fibrous sample, taken from the z-direction (xy plane). The fibres form a cellular-like pattern similar to a dry polydisperse foam. On the right of the figure is a photograph of a sample with backlighting applied. The image was also taken from the z-direction. A similar cell-like pattern is observed in the photograph, presumably due to the fibres being orientated by the bubbles while in the foam. The cellular-like arrangement of the fibres as well as no apparent fibre layers in this plane (xy-plane), results in the fibre orientations displaying an almost flat distribution with no apparent dominant direction.

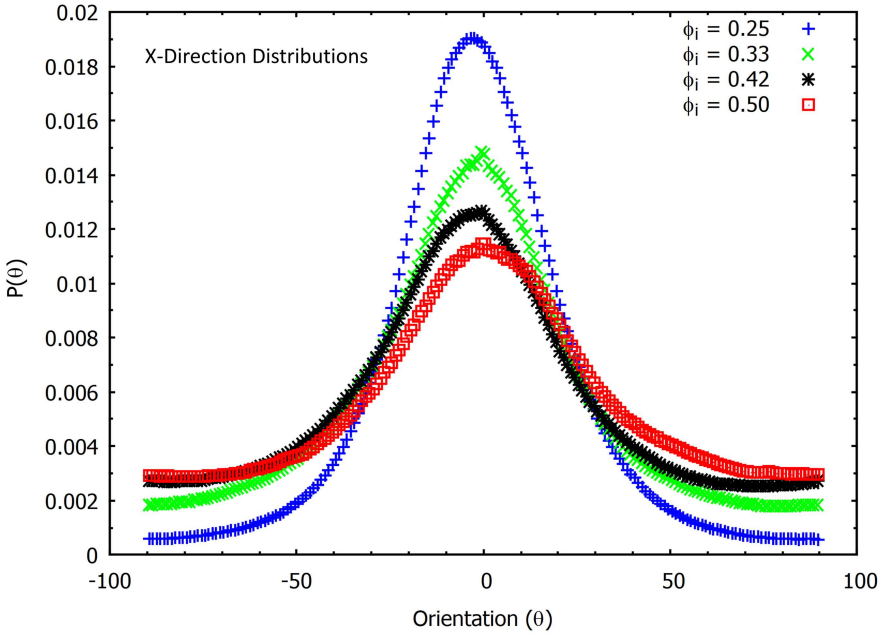

Fig 6.12: A two dimensional projection of the distributions along the x-direction for samples produced using four different values of initial liquid fraction ϕ_i. The width of the distributions increases with ϕ_i.

Since the orientation distributions, as obtained from scanning the sample in both x and y-directions, are very similar (as expected by symmetry) we will only consider distributions from the x-direction. Figure 6.12 shows the projected distributions for all our four samples, produced with different values of initial liquid fraction, but having the same material density.

While the maxima of the four distributions are all at angle zero (i.e. a preferred fibre orientation in the xy-plane), the distributions broaden with increasing ϕ_i. Figure 6.12 shows $P(\theta)$ as a function of ϕ_i. The symmetry of the distributions allow us to combine the data for positive and negative angles. The bins in figure 6.13a were computed by integrating over the corresponding ranges of angles.

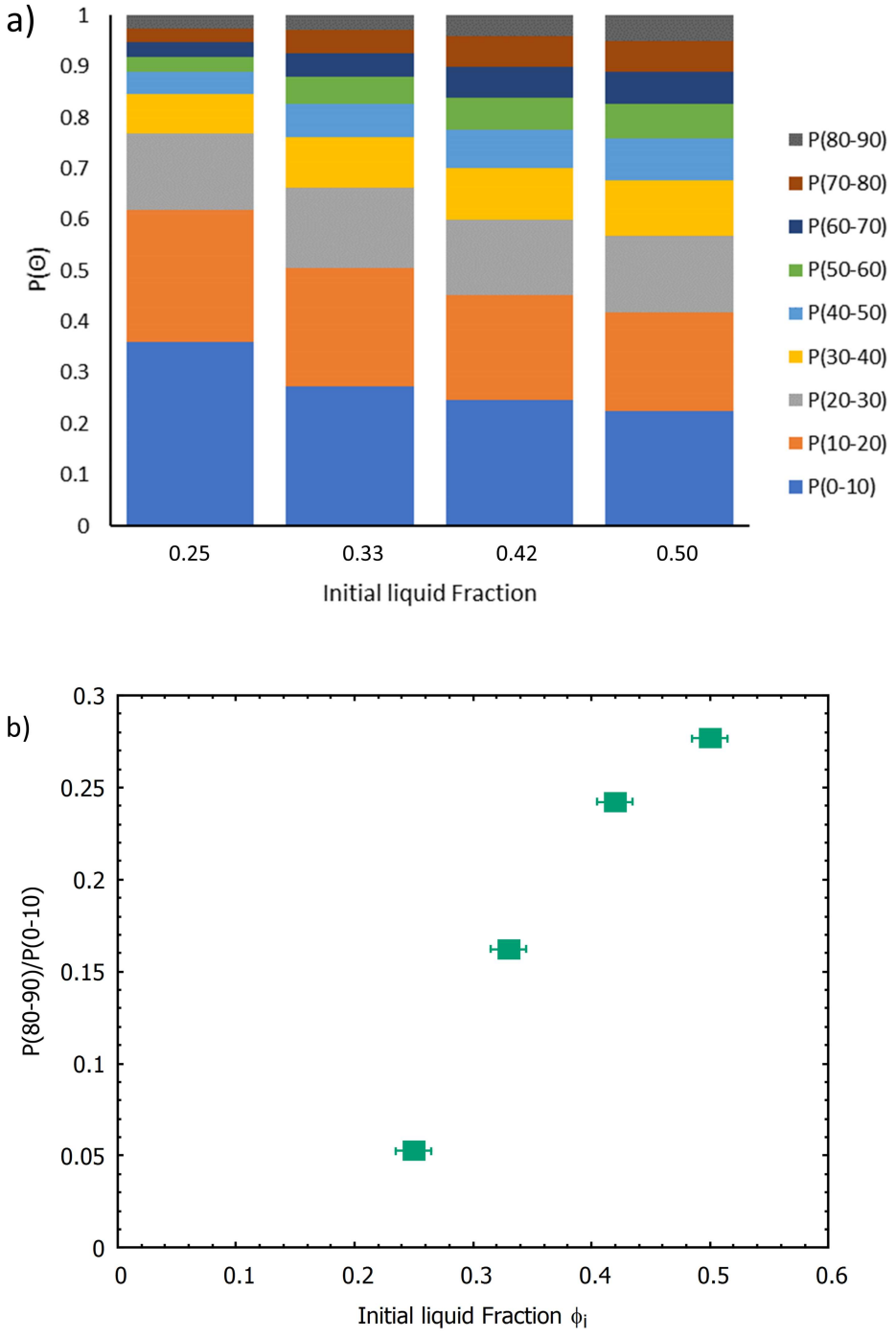

Fig 6.13: a) Fibre orientation probabilities for a range of bin sizes as a function of the initial liquid fraction. The bins represent the fraction of fibres orientated with angles 0° to 10°, 10° to 20°, 20° to 30 ° etc. Increasing the initial liquid fraction ϕ_i leads to more fibres aligning out of the xy-plane ($P(0-10)$). b) Probability ratio of $P(80-90)/P(0-10)$ as a function of ϕ_i. An increase in initial liquid fraction results in more fibres aligning in the direction of gravity (i.e out of the xy-plane).

The $P(0-10)$ bin size shows while the majority of fibres are orientated in this range, the fraction decreases with an increase in ϕ_i. Similar trends are seen for the $P(10-20)$ and $P(20-30)$ bins, after which the trend is reversed, i.e. we have an increasing probability of fibres being orientated towards the z-direction (direction of gravity). This is illustrated in figure 6.13b, which shows the ratio of fibres orientating at the two extremes, $P(80-90)/P(0-10)$, as a function of the initial liquid fraction. This ratio is a simple measure to quantify the horizontal and vertical alignment of the fibres which is sensitive to the compressive modulus.

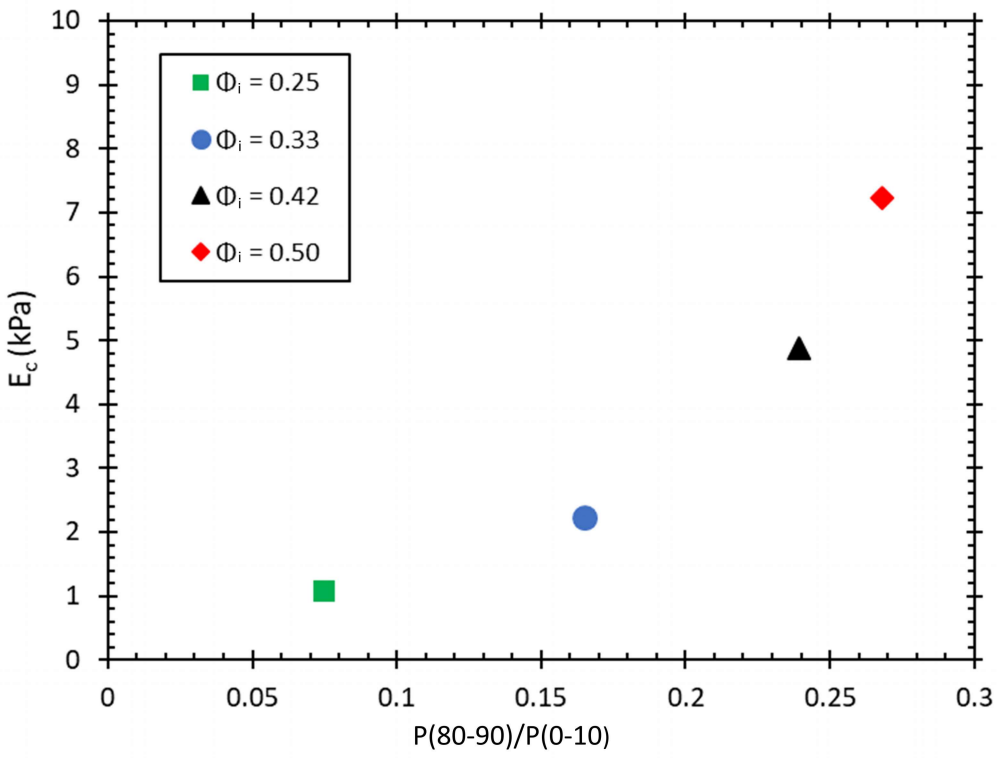

Fig 6.14: The dependence of the compressive modulus on the orientation probability ratio $P(80-90)/P(0-10)$. An increasing ratio results in samples with increasing compressive strength. E_c was obtained by compressing the samples in the z-direction.

Figure 6.14 shows a seven-fold increase of the compressive modulus, as measured along the z-direction. This is solely due to changes in the structure of

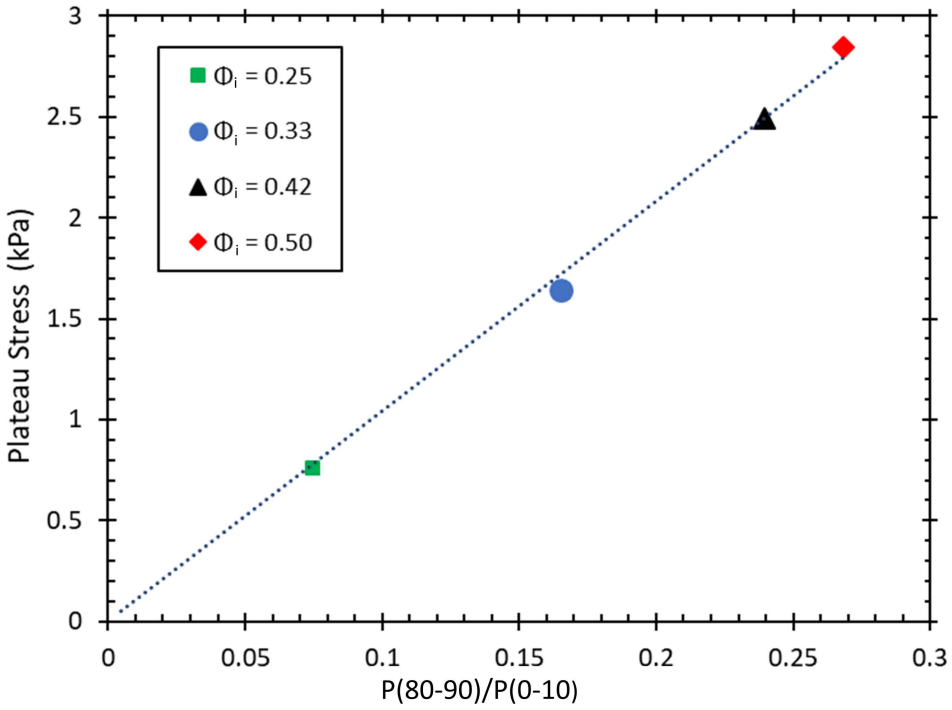

Fig 6.15: The plateau stress varies linearly with the fibre orientation factor $P(80-90)/P(0-10)$, a measure of the fraction of fibres aligned towards the z-direction, and which is controlled via the initial liquid fraction of the precursor foam-fibre dispersion.

the fibre network as reflected in the ratio $P(80-90)/P(0-10)$. An increase of this ratio means that fibres are increasingly aligned along the z-direction. This demonstrates the role that the initial liquid fraction plays in the formation of the fibre network structure; increased drainage leads to fibre alignment along the z-direction (direction of gravity). This in turn has a large effect on the compressive modulus while the density of the structure remains the same.

The level of stress require to initiate the buckling of the layers (plateau stress in figure 5.10b) is plotted as a function of the probability ratio $P(80-90)/P(0-10)$ in figure 6.15. The trend is linear, with an increase in the plateau stress as the $P(80-90)/P(0-10)$ ratio increases.

These distributions show why an increased force is required to initiate the

buckling behaviour we find in figure 5.10b, where the samples are compressed from the x-direction. We offer an explanation as to why there is an increase in the compressive strength of the samples in all three axial directions in the conclusion/discussion section below.

6.5 Discussion and Conclusion

Increasing ϕ_i leads to an increased volume of liquid draining through the dispersion in the initial stage of sample preparation, with the effect of aligning more of the fibres into the direction of drainage (z-direction). The effect of this alignment on the mechanical properties of the material can be seen in chapter 5. We have shown the compressive strength to increase in all three axial directions. However, the stress-strain response is different, depending on whether compression is applied along the z-direction or the x or y-direction.

To lend an explanation as to why this occurs, we first recap on some of the similarities and differences between the samples. The average void size has been shown to be roughly constant and independent of the liquid fraction of the foam-fibre dispersions. The average void radius of the samples made with the two extremes of ϕ_i (0.25 and 0.50) were almost identical, both being $\approx$ 0.6mm. Fibre orientation distributions show that as we increase ϕ_i, we have an increasing probability of fibres being orientated in the z-direction.

Our density profiles, fibre orientation distributions and the three dimensional rendered image from within one of the samples all indicate to a layering of the fibres. A schematic of two structures is shown in figure 6.16. The samples are orientated with the fibre layers (xy-planes) in the vertical position as if the samples are being compressed from the x-direction. Structure A is assumed to be made with a low value of ϕ_i, while structure B is made with a much higher value of ϕ_i.

Structure A has thicker layers due to an increased number of fibres orien-

tating in the xy-planes, at the expense of less fibres bundles aligning between the layers (support fibres).

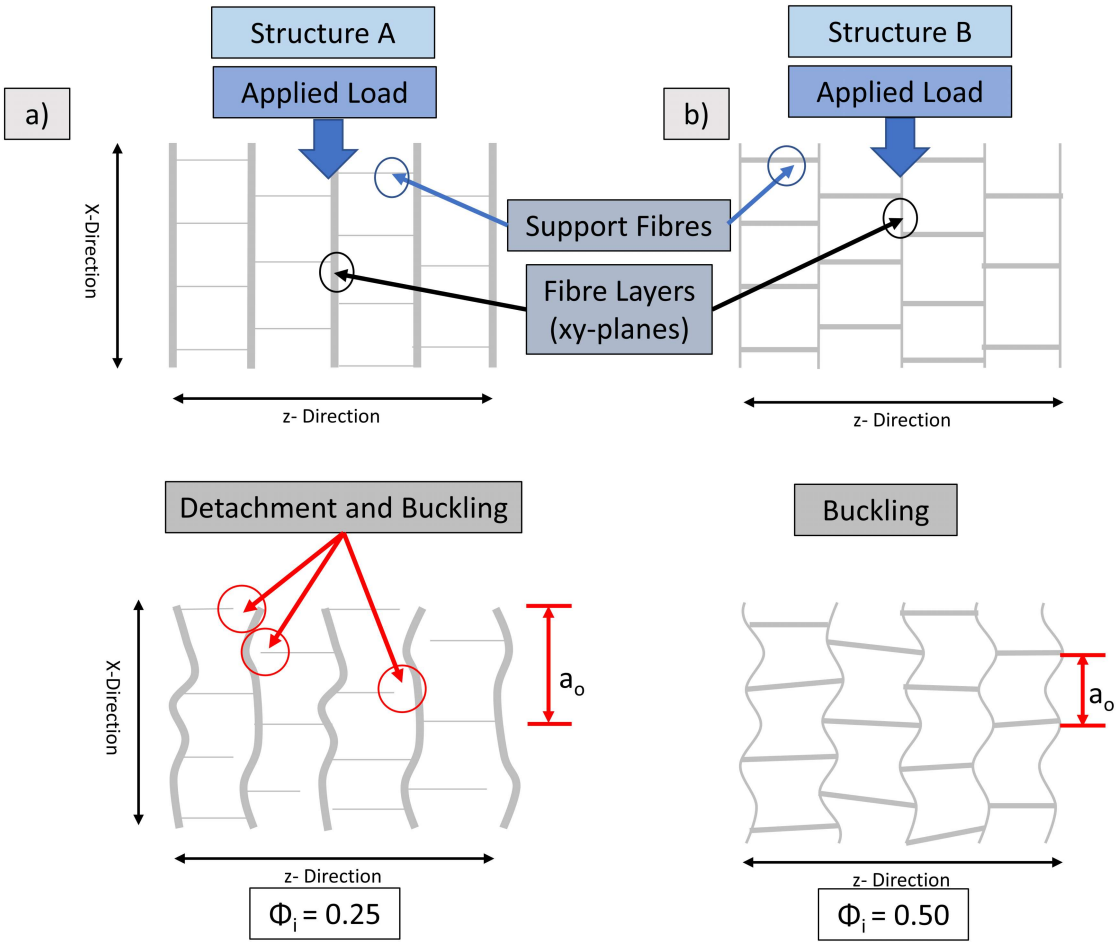

Fig 6.16: Schematics showing the layering and support fibres within the lightweight samples. The schematic on the left represents a sample made with a lower value of ϕ_i (Structure A), while the right schematic represents a sample made with a higher value of ϕ_i (Structure B).

The variation in the initial behaviour (elastic regime), when compressed from the x-direction (figure 5.10b) can be attributed to the supporting fibre bundles between the layers. Initially, as the sample is compressed, the fibre layers begin to elastically bend in the linear regime. The bending of these fibre layers distributes transverse tensional loading onto the fibres connecting the layers. Having fewer connecting fibres (due to a lower ϕ_i) results in fibre

detachments occurring at a lower level of stress during the compression.

These fibre detachments have the effect of increasing the mean free span of the network a_0, and subsequently require less force to initiate buckling, as described by Euler's formula for the critical buckling force (equation 5.4). Therefore, samples made with a lower ϕ_i support less of a load before the layers buckle, even though these layers contain more fibres.

At the other end of the scale, where the sample is made with a higher initial liquid fraction, the layers are thinner and have an increased number of support fibres attached between. Either these support fibres detach, requiring an increased level of stress to do so, or the shorter free span length of the layers buckle, again requiring an increased level of stress.

The plateaus in figure 5.10b, are indicative of columnar buckling [98]. The almost continuous level of stress at the buckling plateaus indicates to a constant mean free span of the network in this regime. The samples with the greater number of fibres in the layers buckle first due to an increase in their mean free span as the support fibres detach.

Chapter 7

Case Study: Foam-Formed Beer Coasters

The brewing industry is important both in Ireland and worldwide. Beer is a significant component of the alcoholic beverage market; Irish companies produce 760 million litres of beer per annum, contributing to 40,000 jobs in the Irish economy [99]. The production process generates 250,000 tonnes of waste by-product annually, of which 85% is in the form of spent grain. Spent grain is often disposed of, used as animal feed or processed to extract nutrients for human consumption [100, 101].

The aim of this study was to produce a product made from recycled or recyclable materials using the foam-forming technique that has properties that match those of similar commercially produced products. We produced beer coasters using brewers spent grain (BSG) and Kraft fibres. The coasters are functional, visually pleasing and have the aroma of the specific brew, giving them a novelty factor (see figure 7.1). This means that aside from effectively repurposing a waste by-product into a higher-value product, the production process also creates a unique beer coaster that is specific to the particular brew.

Fig 7.1: A beer coaster produced using the foam forming technique. The coaster was produced in our laboratory in Trinity College Dublin using brewers spent grain obtained from the Guinness Brewery in Dublin. The Teelings Whiskey Distillery logo was laser-etched on to its surface and some of the coasters were used by Teelings, who are based in Dublin, for marketing purposes. The coaster can be seen to comprise of a wide range of particle sizes, including large grains.

Commercially produced beer coasters are made from refined wood pulp using traditional water-forming techniques. The foam-forming technique is an ideal method to produce beer coasters from fibrous waste material as a wide range of particle sizes and fibre lengths can be distributed in a foam-fibre dispersion. In contrast, sedimentation may occur in water-formed techniques, due to the varying size and density distributions of fibres and particles within BSG, when compared to refined wood pulp.

From an environmental and cost-saving perspective, the foam-forming technique requires lower energy and less wastewater is produced than traditional techniques. Using foam in the process can reduce energy costs by up to 20% during the drying phase, as foam contains up to 50% less water when

compared to traditional techniques [102].

7.1 Spent Grain Composition and Particle Size Analysis

BSG is a lignocellulosic material with a fibre content of around 70%. Its main constituents are lignin, cellulose, hemicellulose, lipids and proteins [103, 104]. There have been many studies on the refinement of BSG to extract key components to be used for human foodstuff and supplements [105–107]. The phenolic acids found in BSG are antioxidant, anticarcinogenic and anti-inflammatory [108–110] . For the purposes of this study, we utilised BSG in its natural form, without any fractionation or grinding.

Components on (g/kg) dry weight basis						
			Cellulose	Hemicellulose		
Proteins	Ashes	Lignin	(glucose)	(Xyl)	(Ara)	Study conducted
153	46	278	168	199	85	(Mussatto and Roberto 2006)
240	24	119	254	NR	NR	(Kanauchi and others 2001)
246	12	217	219	206	90	(Carvalheiro and others 2004)
NR	46	169	253	NR	NR	(Silva and others 2004)
247	42	194	217	136	56	(Moreira and others 2013)

Table 7.1: Composition of brewers spent grain (BSG) according to several different studies, referenced in the table. The high cellulose and hemicellulose content, found in all the studies, make BSG suitable for use in the production of paper/hardboard-like products. Data source [111].

Table 7.1 shows the composition of BSG according to several different studies. BSG contains a high cellulose and hemicellulose content, making it suitable for use in the production of paper/hardboard-like products.

A particle size distribution analysis for BSG was carried out by Alonso-Riano *et al.* [112]. The BSG was of similar type to what we used to produce the beer coasters described in this chapter. Table 7.2 shows that the length of 84.5% of the particles were in the 2 - 4mm range. When producing the beer coasters, we mixed BSG with Kraft fibres. The length of the Kraft fibres used to produce our beer coasters was 2.0±0.1mm with a diameter of 35μm±5μm.

Original BSG		Ground BSG	
Size, mm	**Mass percentage, %**	**Size, mm**	**Mass percentage, %**
>4	4.4	>1	2.9
2–4	84.5	0.5–1	31.3
1–2	10.3	0.25–0.50	34.8
0.5–1	0.71	0.125–0.25	24.6
0.25–0.50	0.06	<0.125	6.5

Table 7.2: The distribution of particle sizes of both non-ground and ground BSG. The BSG used to make the beer coasters for this study was not ground. Data source [112].

7.2 Method to Produce Beer Coasters

To produce the beer coasters, we prepared a foam-fibre dispersion as described in chapter 3 using BSG and Kraft fibres. During the shearing process, we also added 5% weight:weight ratio of Polyvinyl acetate (PVA) to the aqueous dispersion to bond the resulting structure together and increase its stiffness. The foam-fibre dispersion was poured into the drainage vessel and a vacuum was applied to the underside of the gauze at the base of the vessel during the drainage phase (see figure 7.2a). The vacuum collapsed the foam-fibre dispersion, removing most of the liquid, leaving behind a flat fibrous sheet. The sheet was removed from the gauze and then compressed to increase its density. This was achieved by placing it between two aluminium plates and compressing the plates together with four clamps. Spacers (1.5mm thick) were

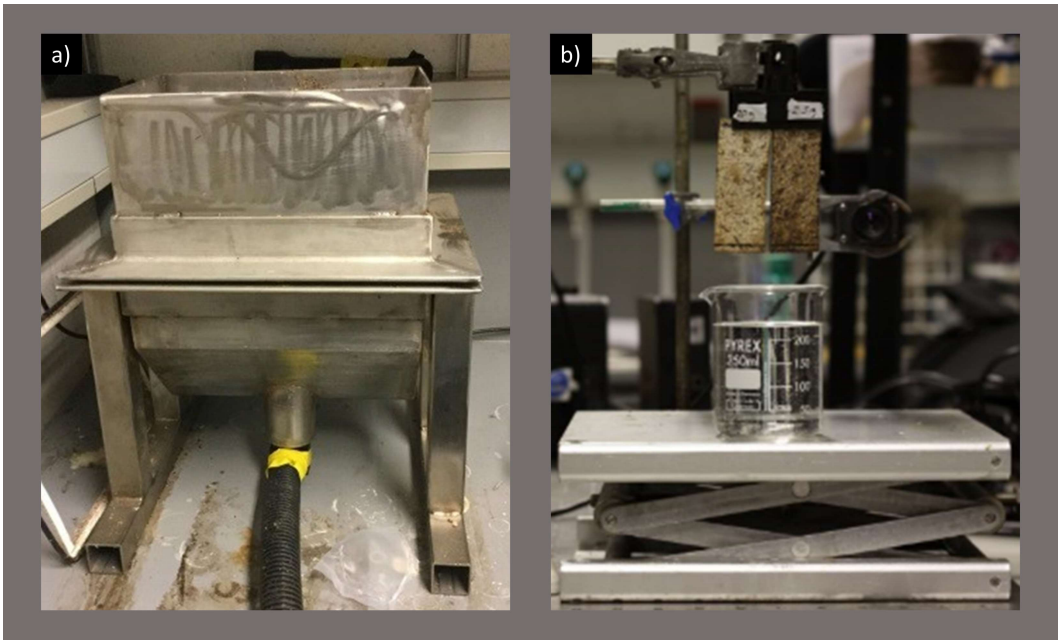

Fig 7.2: a) The drainage vessel used to extract the foam from the dispersion by applying a vacuum to the underside of the wire gauze. A vacuum was applied through the black tubing. b) The imbibition experimental set up. Two samples are suspended from a retort stand over a beaker of water. The beaker is raised to the point at which 5mm of the sample is immersed in the water.

placed between the metal plates thereby compressing all sheets to the same thickness. The sheet was removed from the plates and allowed to air dry in the lab for several days before testing was carried out.

During preliminary experiments, we found the Kraft fibres helped to bind the material together. When we tried to create a sheet of BSG and PVA only, the material was difficult to remove from the gauze and tore very easily. Therefore all BSG coasters produced contained some Kraft fibres.

7.3 Material Characteristics of BSG Coasters

In the following subsections, we investigate the key functional properties of the BSG beer coasters: density, quantity of water absorbed, rate of absorption and tensile strength. We then make comparisons to that of a standard, commercially produced beer coaster.

7.3.1 Density Measurements

We obtained the density of three commercially produced beer coasters by measuring their weight and dimensions. Micrometer readings were used to measure their thickness. The density of the commercially produced beer coasters was found to range from 400-450$kg.m^{-3}$. The density of each BSG coaster was calculated and compared to the commercially produced beer coasters.

Kraft:BSG	Thickness (mm)	Density (kg.m^{-3})
Commercial Coaster	1.15	425
50:50	1.83	434
30:70	1.98	482
20:80	1.66	468
10:90	1.75	363
Total Sample Mass: 50g		

Table 7.3: Composition of the BSG beer coasters and a standard beer coaster. Column 1 shows the ratio of Kraft fibres to BSG used when producing the beer coasters. Sample density was very similar to that of the commercially produced beer coasters. The total sample mass refers to the total mass of fibres used to produce one A4 sized sheet.

Table 7.3 shows the density and thickness of the BSG coasters as the ratio of Kraft fibre to BSG was varied. The averaged values for the commercially produced beer coasters are also included. The total combined mass (50g) refers to the total mass of Kraft fibres and BSG used in the production of one sheet (A4 size), from which six coasters were made.

7.3.2 Imbibition of Spent Grain Coasters

An important property of a beer coaster is its ability to absorb liquid. In this section we report on the rise of the wetted front as each sample absorbs water, see figure 7.2b.

The time dependency of the imbibition of a material can be described by the Lucas-Washburn equation [113, 114]. This equation relates the position of the wetted front, H(t) in a capillary tube to time, t. In its standard form,

$$H(t) = Ct^{\frac{1}{2}} \tag{7.1}$$

With

$$C = \sqrt{\frac{\sigma r \cos(\theta)}{2\eta}} \tag{7.2}$$

Where σ is the surface tension, r is the radius of the tube, θ is the contact angle between the liquid and the tube and η is the dynamic viscosity of the liquid. If the tube is vertical, the rise of the wetted front will reach an equilibrium height, H_0 [115]:

$$H_0 = \frac{\sigma \cos\theta}{r\rho g} \tag{7.3}$$

Where ρ is the density of the fluid and g is the gravitational constant. The capillary rise may be captured by the following empirical formula:

$$H(t) = H_0(1 - exp(-\frac{C}{H_0}t^{\frac{1}{2}})) \tag{7.4}$$

Where

$$\frac{C}{H_0} = \frac{r^{\frac{3}{2}}\rho g}{\sqrt{2\eta\sigma cos\theta}} \tag{7.5}$$

As t $\rightarrow \infty$

$$H(t) \rightarrow H_0 \tag{7.6}$$

For small t,

$$H(t) = Ct^{\frac{1}{2}} \tag{7.7}$$

i.e. it approximates to the Lucas-Washburn equation.

This discussion so far assumes the capillary tubes all have the same radius. However, in porous materials there can be a broad pore size distribution. Using the Lucas-Washburn equation, Cummins *et al.* developed a model which incorporates a range of pore sizes to predict the capillary transport of fluid in porous materials [116]. This replaces the constant C in equation 7.1 by $\frac{8PC}{\omega}$. P is the material's permeability coefficient, a measure of how easily fluid can flow through the material. ω is the material's porosity, measured as the ratio of the volume of pores in the material to the total volume of the material.

Samples were cut from each of the BSG sheets and a 5mm mark was placed at one end. The sample was then clamped onto a retort stand. A beaker of water was placed on a lift-stand underneath the sample. The stand was raised until the water level reached the 5mm mark, at this point $t = 0$. Images of the wetted front were taken at regular intervals with a Canon 50D camera.

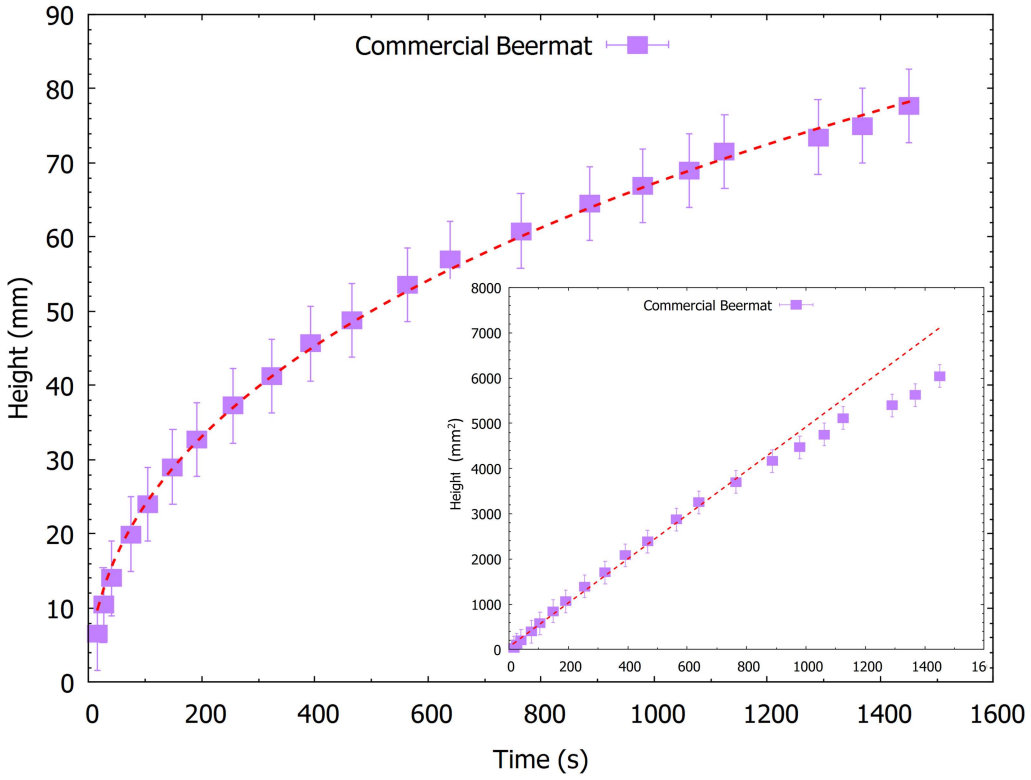

Fig 7.3: The height of the wetted front of a commercially produced beer coaster as a function of time. The data in the main figure has been fitted to equation 7.4. The inset shows H^2 as a function of time, resulting in an asymptotic value for the slope of $4.8mm^2.s^{-1}$.

Figure 7.3 shows the imbibition data for a commercially produced beer coaster. In the main figure the data has been fitted to equation 7.4. There is an initial rapid rise in the height of the wetted front, followed by a slowdown. The inset shows a linear fit to the data with H^2 as a function of time (i.e equation 7.1), resulting in an asymptotic value for the slope of $4.8mm^2.s^{-1}$.

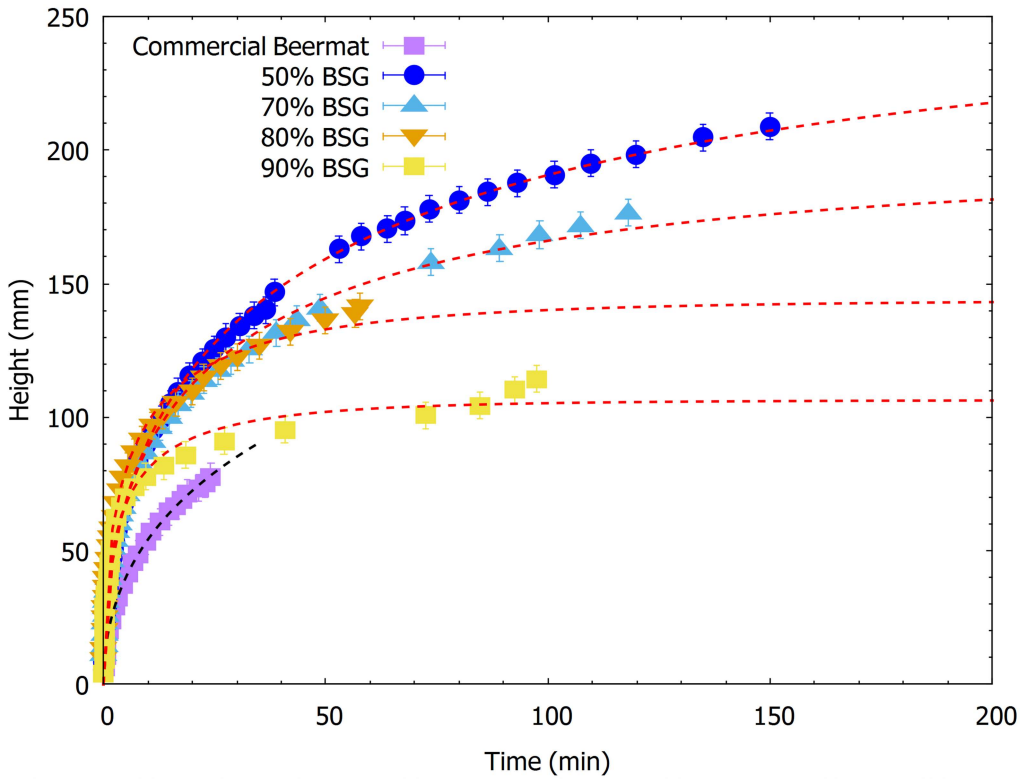

Fig 7.4: Four samples produced from a mixture of BSG and Kraft fibres. Equation 7.4 was fitted to each data set (red dashed lines). As the percentage of Kraft fibres was increased, the equilibrium height of the wetted front increased.

The imbibition data for our samples over a long timescale is presented in figure 7.4. The data shows that as the percentage of Kraft fibres was increased, the equilibrium height of the wetted front increased. The commercial beer coaster never plateaued as it was not large enough: the size of a standard coaster is approximately 100 x 100mm, with 5mm initially submerged in the liquid and 10mm being held by the clamp. The initial transition into the plateau regime is however apparent. The expression adapted by Cummins, suggests that the porosity of the samples may be responsible for the observed increase of H_0 for decreased percentage of BSG.

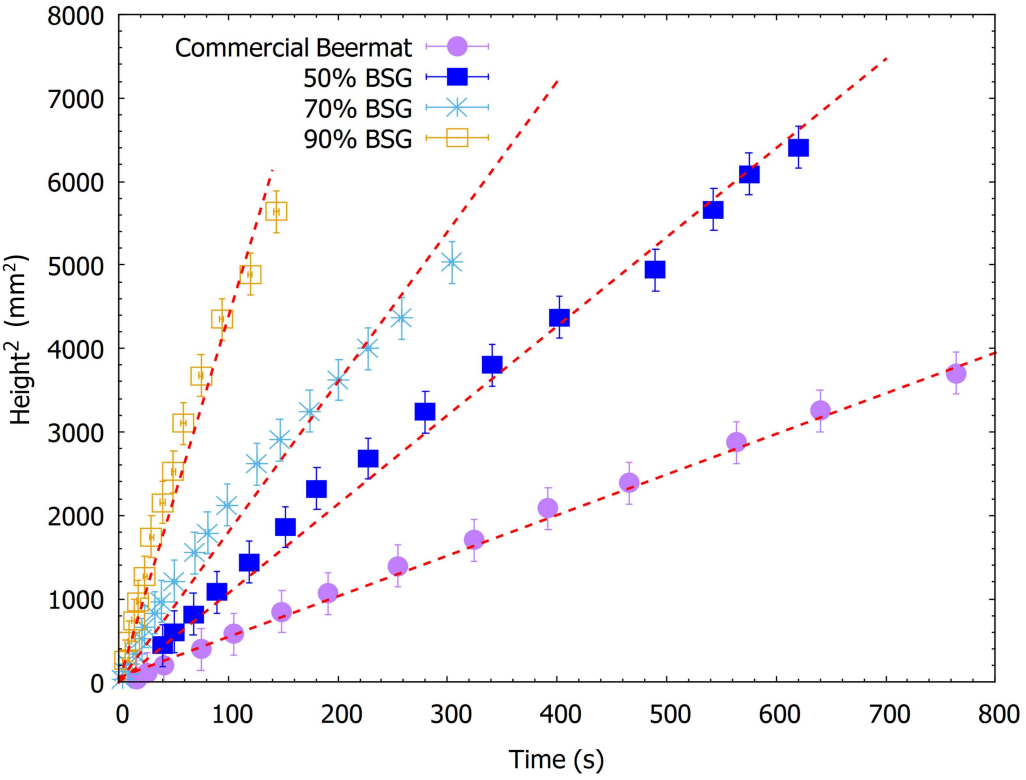

Fig 7.5: The height of the wetted front squared as a function of time for the BSG coasters and a commercially produced coaster. The slope of the linear regime increased as the percentage of BSG was increased.

Figure 7.5 shows the initial linear regimes of several BSG coasters and one commercially produced coaster. The slope of the linear regimes increased as the percentage of BSG was increased, demonstrating that the wetted front rises more rapidly when the percentage of BSG is higher.

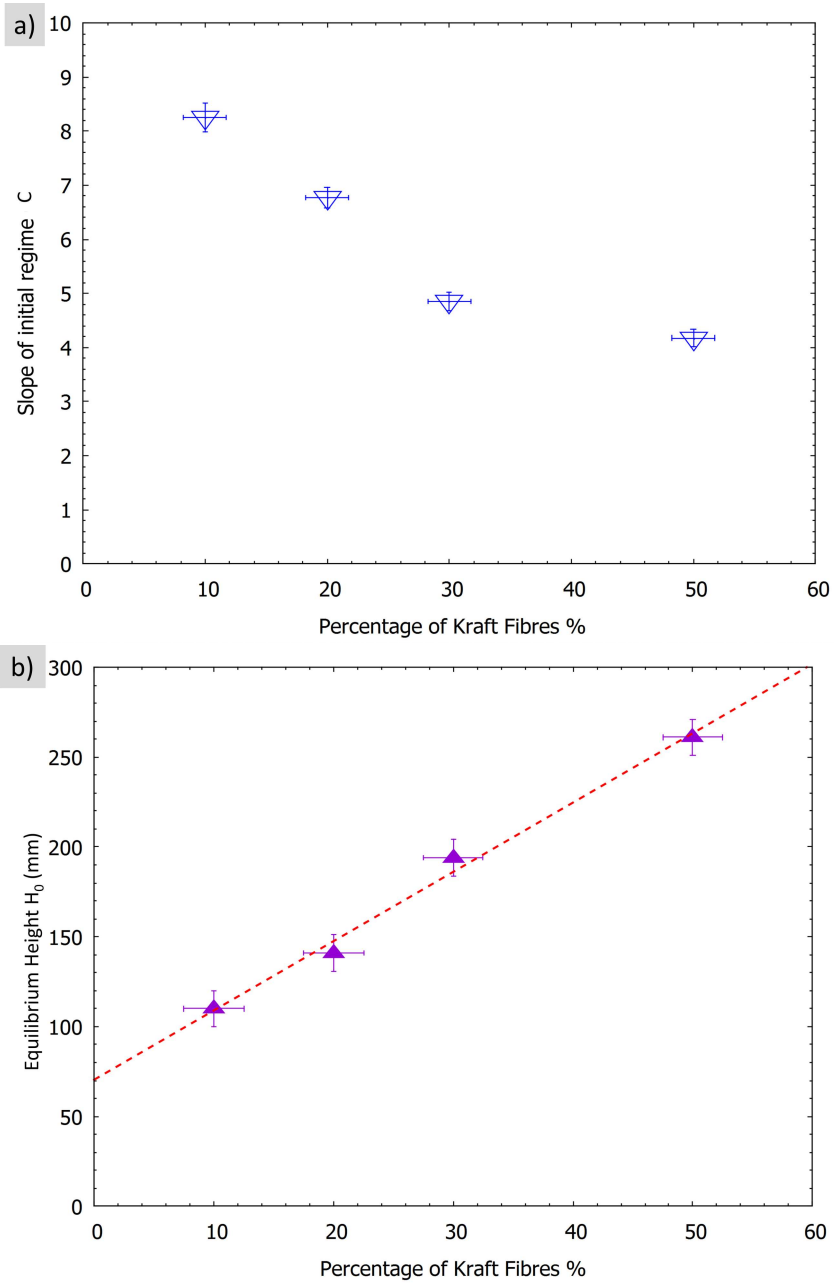

Fig 7.6: a) The coefficient C as a function of the percentage of Kraft fibres contained in the beer coasters. As the percentage of Kraft fibres increases, the rate of increase of the wetted front reduces. b) Equilibrium height H_0 of the wetted front as a function of Kraft fibre percentage. Increasing the percentage of Kraft fibres can be seen to lead to a linear increase in the equilibrium height of the wetted front.

The equilibrium height H_0 and the linear coefficient C was determined for each data set by fitting equation 7.4. H_0 and C as a function of Kraft fibre percentage is plotted in figure 7.6, a and b. As the percentage of Kraft fibres increases, the rate of increase of the wetted front reduces. H_0 increases linearly with the percentage of Kraft fibres.

The imbibition experiments have shown the BSG beer coasters absorb liquid at a faster rate than the commercial beer coaster. The rate at which the liquid is absorbed is dependent on the ratio of BSG to Kraft fibres. As the percentage of BSG is increased, the rate of absorption increases. The equilibrium height the wetted front reaches is dependent on the percentage of Kraft fibres contained in the coasters. Increasing the percentage of Kraft fibres increases the equilibrium height of the wetted front.

7.3.3 Cobb's Experiment

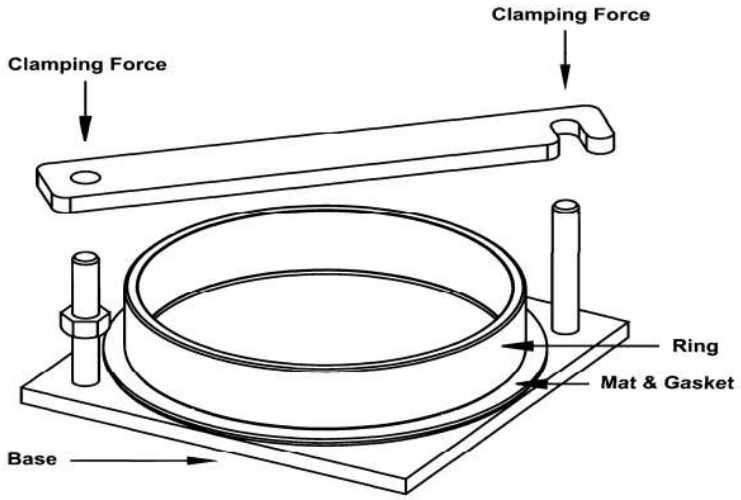

Fig. 1. Specimen holder.

Fig 7.7: Experimental set up used to measure the quantity of water absorbed per unit surface area by the beer coasters. Each sample was allowed to absorb a quantity of water over a time period of 30 seconds. The wet and dry samples were weighed, and the quantity of absorbed water was then determined. Image source [117].

An important property of a beer coaster is how much liquid it can absorb over a short period of time. The Cobb's experiment is an industry standard used to quantify the mass of liquid a porous medium can absorb [117]. We utilised this method to compare the absorption of the BSG beer coasters to commercially produced coasters. Samples were cut from each BSG sheet (6cm x 6cm) and then weighed to establish their dry weight. Next, the sample was clamped between a ring and a metal base, with a rubber gasket under the ring to make a watertight seal (see figure 7.7). 50ml of water was poured onto the sample, covering the exposed sample to a depth of 1cm. The sample was left for 30 seconds after which the excess water was removed, and the sample weighed again. The difference between the before and after weight was the amount of liquid absorbed for a given time. Each measurement was repeated a total of three times per sample and the results averaged.

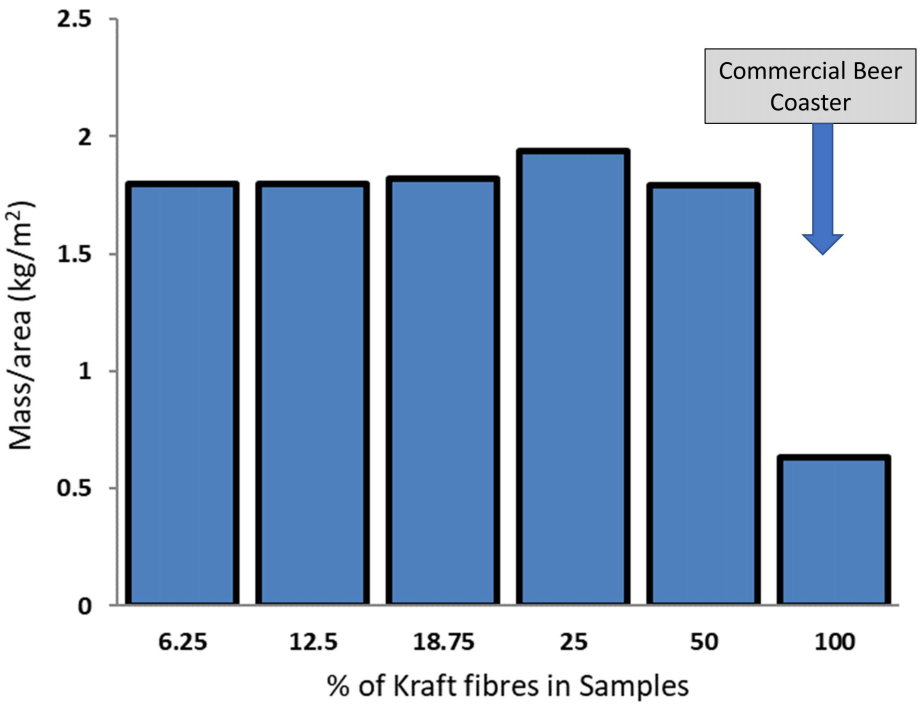

Fig 7.8: Mass of water absorbed per cross sectional area as a function of Kraft fibre percentage by way of the Cobb's experiment. The BSG beer coasters absorbed three times the mass of water as the standard beer coasters after 30 seconds. The commercially produced beer coaster is denoted as 100% Kraft in the histogram above.

Figure 7.8 shows the mass of water per cross sectional area absorbed as a function of Kraft fibre percentage over a period of 30 seconds. The results show the sheets made from BSG can absorb over three times that of the commercially produced beer coaster within a 30 second period. The ratio of BSG to Kraft fibre appears to make little difference to the total amount of liquid the BSG coasters can absorb.

7.3.4 Tensile Testing

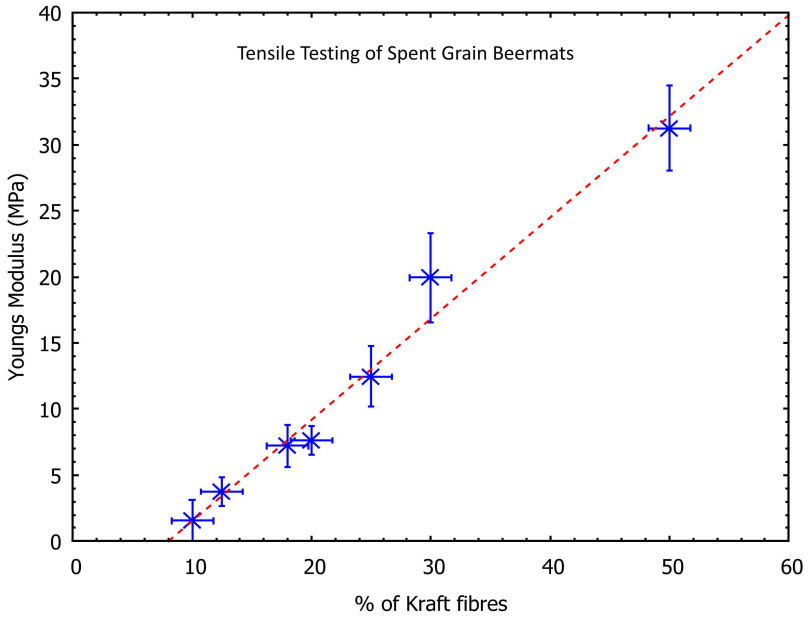

Fig 7.9: Young's modulus as a function of the percentage of Kraft fibres in the BSG beer coasters. Young's modulus increases linearly as the percentage of Kraft fibres increases. The error bars are the standard deviation of five experimental runs per data point.

Tensile testing was carried out with a Zwick/Roell Z005 tensiometer. Five test pieces from each of the BSG coasters were made using a cutting tool to the required size for the tensiometer. The dimensions of each sample were then measured (width and thickness). Each sample was placed between the clamps of the tensiometer and a force applied along the length of the sample. All samples were tested beyond their elastic and plastic regimes, up to the point of total failure (breakage). Young's modulus for each sample was obtained from the initial linear regime of the stress-strain curves. The value obtained for the standard beer coaster was found to be 460MPa, far in excess of the BSG coasters, which showed a maximum of approximately 32 MPa. Figure 7.9 shows the average Young's modulus of five samples per data point as a function of Kraft fibre percentage. The data shows an increasing linear trend to Kraft fibre percentage.

7.4 Conclusion

The foam-forming technique can be successfully used to produce products made from a waste by-product, BSG. The BSG was used in its raw form, the grains were not fractionated or ground. As such, the fibre lengths, particle sizes and density ranges of the particles have wide distributions. The ability of a foam to trap and hold a wide variety of fibres and particles in suspension allows us to use the foam-forming method to disperse the BSG and Kraft fibres evenly, something that may be difficult if a water-borne method was to be used, due to particle sedimentation.

The BSG coasters match, and in some cases, improve on the properties of similar commercially produced beer coasters. The rate of water absorption and the volume of liquid absorbed exceeded that of the standard beer coaster. However, improvements may need to be made to the tensile strength of the material, if this is important to industry.

Increased tensile strength could be achieved by increasing the amount of bonding agent in the foam-fibre dispersions, as the majority of the 5% PVA used was removed during the drainage phase. It might also be worth investigating other types of bonding agents or whether a bonding agent can be applied after the sample has been compressed. Compressing the samples further during the preparation stage with a hydraulic press could also be used to increase tensile strength. However, this could impact on their imbibition and absorption properties as the material's average pore size would change.

VARA Marketing Consultants carried out a marketing analysis on this case study. According to VARA, there are 5-7 million coasters produced every day by the Katz Group in Germany. This equates to 75% of the global market. Coasters made using the foam-forming technique use less water and less energy than traditional water-forming techniques. This could therefore be important from an economic perspective given the scale of production. However, any

change in existing production techniques would require new machinery (or retrofitting existing machinery) at significant cost.

BSG might offer a suitable alternative to wood pulp when producing beer coasters, given its superior rate of liquid absorption and the volume of liquid it can absorb. The benefits of using BSG to produce coasters may also depend on the large-scale availability of BSG to manufacturers of beer coasters such as the Katz Group, the cost of BSG as a raw ingredient and its comparative value if it used for other purposes, such as extracting nutrients for human consumption.

Chapter 8

Conclusions and Outlook

8.1 Conclusions

The aim of the work presented in this thesis was to gain an understanding of how the properties of a foam in which fibres are dispersed can influence the material and mechanical properties of foam-formed lightweight fibrous structures. Our work has extended the field of research concerning foam-fibre dispersions, primarily by providing a greater understanding of the role of the initial liquid fraction of the foam-fibre dispersion used to create the structure. We are now able to incorporate the liquid fraction as a control parameter over material density and compressive strength. This may be important in a wide range of industry applications, such as building materials and protective packaging.

Fibre-laden foam dispersions were prepared by axially shearing an aqueous solution to which fibres and surfactant were added. The majority of the foam-fibre dispersions were created using Kraft fibres. We also used CTMP, viscose rayon, peat and brewers spent grain in our work. We designed and built an apparatus that enabled us to produce lightweight fibrous materials from these dispersions. The design allowed the liquid from the dispersions to drain, while retaining the network of fibres, resulting in the formation of lightweight fibrous

material. When designing the apparatus, we also included the option to apply a vacuum to the dispersions for the production of sheet-like materials, such as in our case study (Chapter 7).

We began our investigations with an extensive set of experiments on the foam-formed fibrous structures. We determined the relationship between sample density, fibre concentration and the initial liquid fraction, ϕ_i of the foam-fibre dispersions used to create the structures. We showed that sample density, ρ scales linearly with fibre concentration, c for all values of ϕ_i investigated in this thesis. We also demonstrated that if c is held constant, ρ can be controlled by ϕ_i.

We then explored the mechanical strength of the samples by way of uniaxial compression testing. We produced four fibrous samples. All samples had the same density, but were made from dispersions with different values of ϕ_i. We measured the compressive strength of each of these samples and found that we could increase E_c by a factor of 7 simply by changing the initial liquid fraction from 0.25 to 0.50. The compressive modulus, E_c scaled linearly with sample density. Increasing ϕ_i was shown to increase this scaling. The results of these experiments demonstrated that we could vary the compressive strength of similar density samples by changing ϕ_i. The results also suggested that the range over which we could vary E_c with ϕ_i increased with sample density. For instance, based on a sample density of $40kg.m^{-3}$, and again changing ϕ_i from 0.25 to 0.50, we could vary the compressive strength by a factor of 20.

We eliminated sample density as a variable in our experiments, focusing on understanding how the liquid content of the dispersions can influence the compressive strength of the resulting material. Through a modified forced drainage experiment, we revealed that it is the rate of liquid draining through the dispersions rather than the volume of liquid which has the larger influence on E_c. The E_c for a sample made using the forced drainage experiment was 1.5kPa. This compared to an E_c of almost 8kPa for a higher ϕ_i (ϕ_i=0.5), but

with the same volume of liquid draining through the sample. This suggested that the width of the Plateau borders in the dispersion (wider when ϕ_i is increased) contributes to more fibres orientating in the direction of drainage, increasing the material's E_c.

Our samples displayed different stress-strain responses when compressed from the z or x and y-directions. When the samples were compressed from the z-direction (direction of drainage), they required an increasing stress throughout the compression cycle. When compressed from the x or y-direction (orthogonal to the direction of drainage), after an initial linear elastic regime, very little stress was required to compress the sample. To investigate this, we imaged the samples by way of μCT scanning and performed further analysis to understand the anisotropic response and why E_c varied with ϕ_i. Our imaging and analysis showed the void size distributions of the fibrous samples to be very similar, even when ϕ_i was varied. However, a fibre orientation analysis showed that ϕ_i greatly influenced the fibre orientation distributions.

Fibre orientation analysis showed that fibres form layers in the xy plane. As ϕ_i is increased, more fibres orientate in the z-direction (direction of drainage). As the sample is compressed in the x or y-direction, the fibre layers begin to bend. This distributes the transverse tensional loading onto the fibres connecting the layers. When ϕ_i is lower, there are fewer connecting fibres, resulting in fibre detachments occurring at a lower level of stress during compression. These detachments increase the mean free span of the network, subsequently requiring less force to initiate buckling. Therefore samples made with a lower ϕ_i support less of a load, when compressed in the x or y-direction, before the layers buckle than samples made with higher ϕ_i, even though these samples contain more fibres orientated in the xy plane.

We found that as the average fibre length was increased, E_c decreased, the trend of the decrease is described by an exponential decay function. This could be due to larger bubbles (as a consequence of longer fibres) reducing

the mean free span of the network, decreasing the structure's compressive strength.

We investigated the effect of fibre concentration on the typical behaviour of a foam. We found that the addition of fibres to a foam significantly extends its lifetime. This could be due to an increase in liquid being retained by the fibres as c is increased, keeping the bubbles wetted for longer, thus extending their lifetimes. The fibre concentration also influenced the coarsening behaviour of the dispersions. The Sauter Mean Radius of the bubbles in a pure foam were seen to scale to $t^{\frac{1}{2}}$ as the average bubble size continually increased. However when fibres were added, this had the effect of arresting coarsening after approximately 30-40 minutes. ϕ_i appeared to play no role in this observed behaviour, suggesting that it is the fibre content rather than the liquid fraction that determines the size at which bubble growth terminates.

We reported on the minimum fibre concentration required for a dispersion to create a stable structure after the foam has decayed and the structure dried. When $\phi_i = 0.25$, fibre concentrations of $c = 0.25\%$ or less led to structural collapse, due to an insufficient number of fibre-fibre contacts being made. We found that when $c<1\%$, structure height was dependent on fibre concentration, above this concentration, the final sample height was independent of c.

8.2 Outlook

We began this thesis by observing that there has been a global shift towards using sustainable materials as well as developing more environmentally friendly production methods. This is not just important from an environmental perspective; industry is increasingly acknowledging that such materials and methods can add value and reduce costs. We noted however that for industry to take an interest, the properties of the sustainable alternative should perform the same or better than its non-sustainable counterpart, all at the same or

lower cost.

The foam-forming method is an ideal process given that it uses less water and energy than other methods, such as water forming. Arising from our research, we now understand the fundamentals of how the foam-forming method can be used to create lightweight fibrous materials and how the properties of a dispersion can control the material properties. To develop our work further, I believe that we need to focus on non-sustainable materials in widespread use, such as expanded polystyrene (EPS) and probe our samples for the key requirements, using the work presented in this thesis as a starting point.

EPS has a density in the same range as our lightweight fibrous samples and is often used as thermal insulation and/or protective packaging. One of the main challenges associated with this petrochemically-derived material is the prohibitively high costs associated with recycling EPS into a monomer styrene so that it can be re-used. The process of recycling EPS requires a high heat (430°C) and pressure to break the chemical bonds between the styrene molecules, therefore involving significant energy and cost. Often, EPS is not recycled and ends up in landfill or littering our oceans. In Ireland, very little EPS is recycled [118]. The key properties of EPS are its thermal conductivity, compressive strength and recovery.

In the following sections we have considered the direction the project could take, taking account of our focus.

8.2.1 Controlling Compressive Strength and Recovery

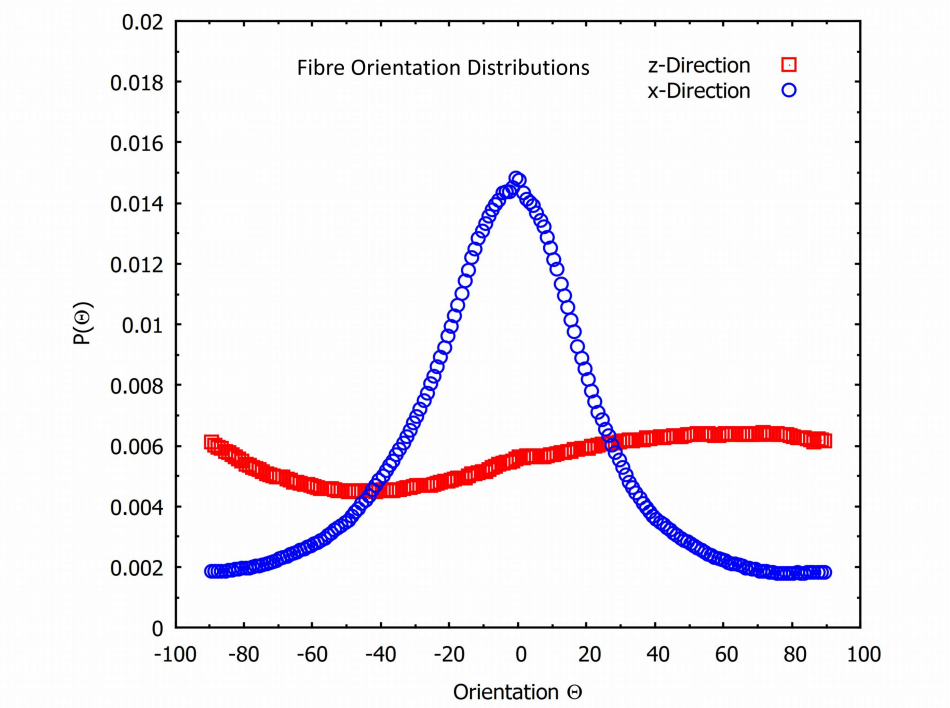

Fig 8.1: Fibre orientation distribution from the x and z-directions. The sample was made of Kraft fibres by way of foam-forming. The x-distribution shows the majority of the fibres are orientated at zero degrees (orthogonal to drainage).

We showed earlier that the liquid fraction of a dispersion can control the sample compressive strength, however varying the liquid fraction may not be practical from an industrial perspective. We addressed this by carrying out forced drainage experiments in which the liquid fraction was held constant, but the duration of drainage was increased. We showed that this approach can also vary the material compressive strength, but not to the same extent as varying the liquid fraction. Our approach was rudimentary: we simply extended the duration of liquid drainage by adding a pure foam (no fibres added) on top of a foam-fibre dispersion. While this approach allows for an even dispersal of the liquid over the area of the foam, it does not allow us to control the flow rate, extend the duration of drainage for any meaningful

length of time or provide much control over the fibre orientation (see figure 8.1 which shows the majority of fibres lie in the xy-plane). If we can orientate more fibres out of the xy-plane, we can increase the compressive strength.

An apparatus could be designed to pump a fine mist over the foam-fibre dispersion from a reservoir. This would allow us to control both the rate of liquid drainage and the total liquid volume passing through the dispersion. By doing this, we may be able to identify an optimum liquid fraction at which the plateau borders are large enough to allow greater control over the fibre orientations through the use of forced drainage. This would mean we could eliminate the liquid fraction of the foam as a control parameter and instead have the drainage rate as the control parameter.

8.2.2 Consideration of Fibre Length and Fibre Stiffness

We have shown how fibre length affects the material compressive strength, with shorter fibres requiring an increased load to reach the same level of strain as longer fibres (see section 5.7). Therefore, to increase a fibrous material's compressive strength, shorter or stiffer fibres could be incorporated into the material. There are numerous fibre types which may be relevant for this particular investigation. Recycled newspaper or cardboard is one example. The average fibre length of recycled fibres is reduced due to the recycling process, with a large number of fines included [119]. Coir fibres, extracted from the outer husk of the coconut may also be interesting to study. Coir is already used to produce floor mats and brushes due to the stiff nature of the fibre.

8.2.3 Increasing the Compressive Strength by Adding a Bonding Agent or Incorporating Other Fibre Types

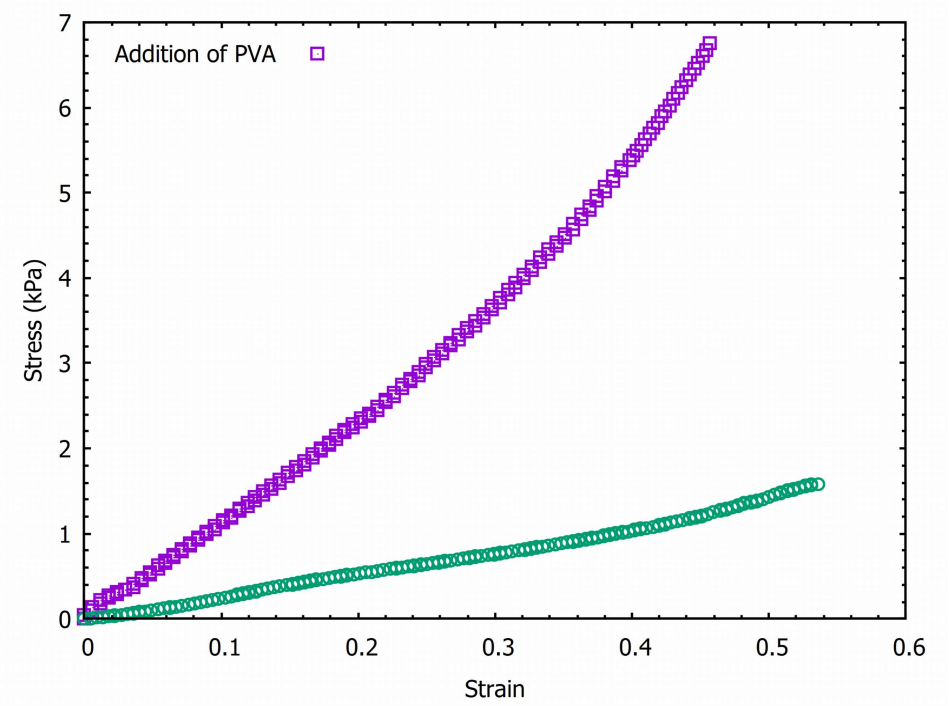

Fig 8.2: The addition of the bonding agent PVA can be seen to have a dramatic effect on the stress-strain behaviour of the sample (purple data set). The green data set contained no bonding agent. Both samples contained the same mass of Kraft fibres.

Compressive strength can be significantly increased by the use of bonding agents. We have already carried out some preliminary experiments in this regard, see Appendix B for full details. We found that the addition of the bonding agent PVA to a sample made of Kraft fibres can increase the compressive modulus by almost a factor of 4. We also carried out several tests on foam-formed fibrous structures made from CTMP, spent grain and peat fibres to establish how their compressive strengths compare to Kraft fibres. Samples made from these natural fibres were seen to have a larger compressive modulus than a sample made from just Kraft fibres, see figure 8.3.

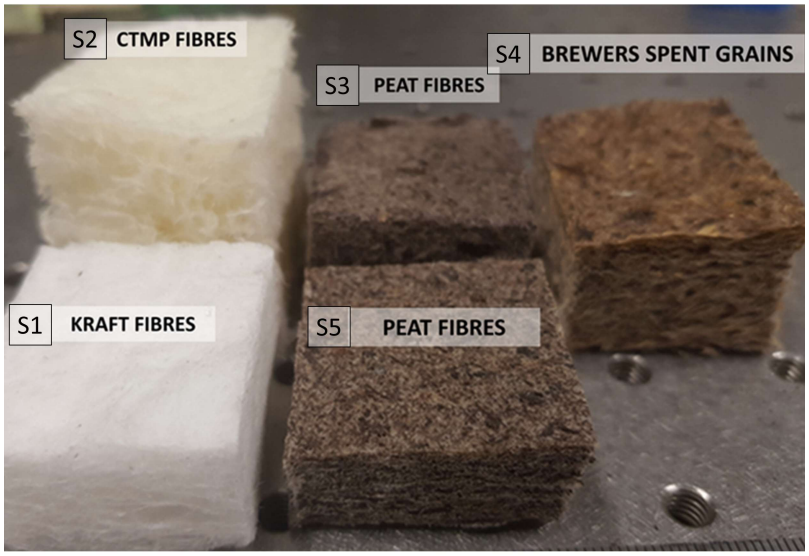

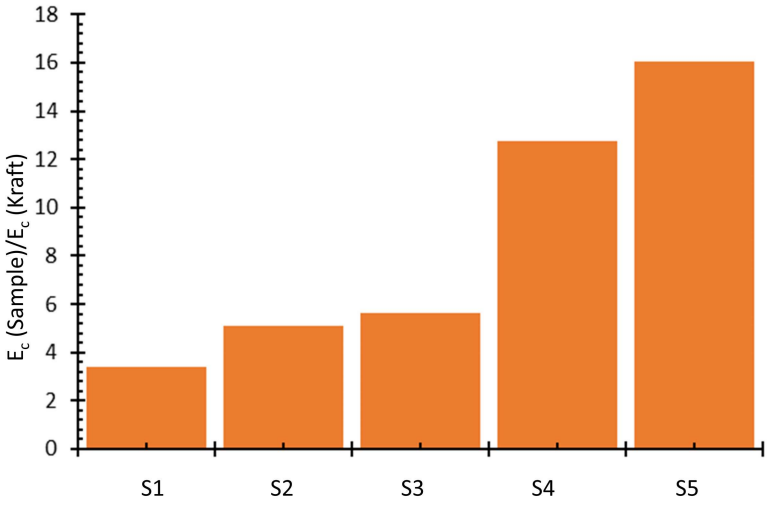

Fig 8.3: Top: A range of samples made of recycled and recyclable fibres. All samples include the addition of the bonding agent PVA. Bottom: A comparison between the compressive moduli of a number of different fibre type samples to that of same density samples made of only Kraft fibre (no PVA). The addition of PVA is seen to increase the compressive strength of the Kraft sample (S1) by almost a factor of 4. The samples made of other natural fibres are also seen to have a larger compressive modulus than a pure Kraft sample.

Taking account of this preliminary work, a study could be carried out to test other bonding agents and fibres, particularly those that are considered environmentally friendly. Carrageen moss is one such material that could merit further investigation as a bonding agent and to aid compression recovery. It is a type of seaweed (algae) that has traditionally been used as a food supplement and as a skin cleanser but is reported to have strong bonding characteristics when bonding with food proteins [120].

This idea arose following a collaborative project between our group and a group of final-year undergraduate students from the National College of Art and Design in Dublin. The students were asked to suggest novel uses for foam-formed natural fibres. One student made a foam-formed paper sheet using Carrageen moss and Kraft fibres. The paper produced using the moss appeared very stiff (plastic-like), with a good recovery when crumpled in the hand. Although the collaboration was primarily focussed on the design of foam-formed natural materials, this sparked the idea to investigate the bonding and recovery properties of the moss.

To test the moss's influence on compressive strength and material recovery, it could be incorporated into the dispersion during the production stage. A series of experiments would begin with Kraft fibres only (as we already know how they perform) and then investigate the compressive strength and hysteresis of a variety of samples made with different concentrations of moss. As density is also important, the samples could be made with a density similar to commercially available EPS.

8.2.4 Thermal Conductivity

A low value for thermal conductivity means that a material is a better insulator. Dominguez-Munoz *et al.* reported that thermal conductivity for low density samples (8-45 kg.m^{-3}) decreases with increasing sample density. Both EPS and our lightweight fibrous materials are in this density range.

We did not have the opportunity to carry out thermal conductivity tests, so the starting point would be to carry out these tests, then identify how to reduce the thermal conductivity values of our samples further. This could be achieved by increasing the void size of the fibrous material. We showed earlier that the void size is related to the dispersion bubble size. To gain control over bubble size, we would need to rethink our approach to fibre dispersal, as axially shearing at high rates produces very small bubble sizes. We could potentially reduce the shear rate while also increasing the foam's viscosity (by adding glycerol for example) thereby increasing the average void size. We could also consider foam-fibre coarsening to identify how the mass of fibres place an upper limit on bubble growth in the coarsening-arrested regime. (However, this may be a trivial matter due to the structures being open-cell: the void sizes may not matter as much as in a closed-cell material.)

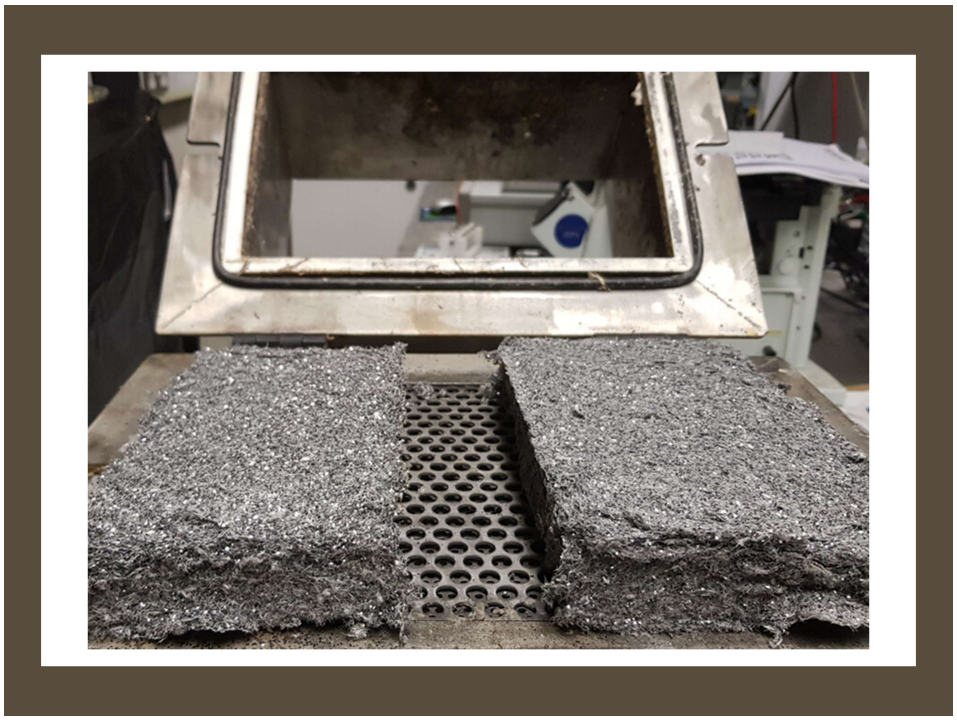

Fig 8.4: Two samples made by foam-forming. Both contained a quantity of graphene flakes and Kraft fibres. The samples were made to determine if the higher density graphene would sediment from the dispersions. No sedimentation occurred.

The material conductivity value may be reduced by the addition of other materials. Graphene may offer promise in this regard [121]. Preliminary experiments demonstrated that foam-formed samples could be made using Kraft fibres and graphene flakes, see figure 8.4. The higher density of the graphene did not sediment out of solution when preparing the sample. A visual inspection showed that the flakes appeared to be evenly distributed throughout the sample (to be confirmed by μCT scans). This could be developed in a systematic manner to identify an optimum concentration of graphene to minimise thermal conductivity value.

8.2.5 Thickness of Foam-Formed Lightweight Materials-

We have set out several suggested experiments to analyse and improve on the material compressive strength and thermal conductivity value. However, from a practical perspective, it is important to understand the limitations of the samples produced for our experimental analysis.

All of the dispersions in this thesis were made from the same volume of foam and poured into the same drainage vessel. This meant that the initial heights of all the foam-fibre dispersions were the same. To make a thicker sample we would have to increase the initial height of a dispersion by increasing its volume. However, as we increase the height of a dispersion, there will be additional liquid drainage through the foam. This may affect the fibre density profile as well as the fibre distribution profile of the resulting structure, as the bottom of the dispersion will have significantly more liquid draining through than the top or middle portions. Therefore, it would be worthwhile exploring the maximum foam height (and liquid fraction value) before the resulting structure displays a non-uniform fibre density or fibre orientation profile.

8.2.6 Vibrational Technique to Measure Bubble Size

Lastly, we considered the efficacy of some of our experimental methods. For example, we used the microscope slide method to identify bubble sizes for the experiments discussed in this thesis. This approach is somewhat invasive as a sample of foam is extracted each time a measurement is required. To overcome this, we carried out preliminary investigations into an alternative technique in which we analysed the vibrational response emitted from a bursting bubble. This technique could be used to monitor bubble size during coarsening and may be more effective than other methods (for example, optical measurements are difficult when fibres are dispersed in a foam).

We began by looking at the vibrational response emitted from single bubbles as they their rupture. There have already been numerous studies into the acoustic emissions from bubbles as they rupture, with one suggesting there is a precursor signal emitted before the rupture takes place. We detected a similar signal using the vibrational technique. However, using high-speed photography, we believe this is the vibrational signal of the rupture propagating along the bubble's film. We also showed that the bubble size can be inferred from the duration of the initial vibrational emitted during rupture.

This technique could be developed in a future project to accurately ascertain when bubble growth has ceased or when all the bubbles within a dispersion have ruptured. This means that, for example, in an industry setting, the earliest time at which impingement drying can be effectively implemented can be identified.

Appendix A

A.1 Vibrational Technique to Monitor Foam-Fibre Coarsening

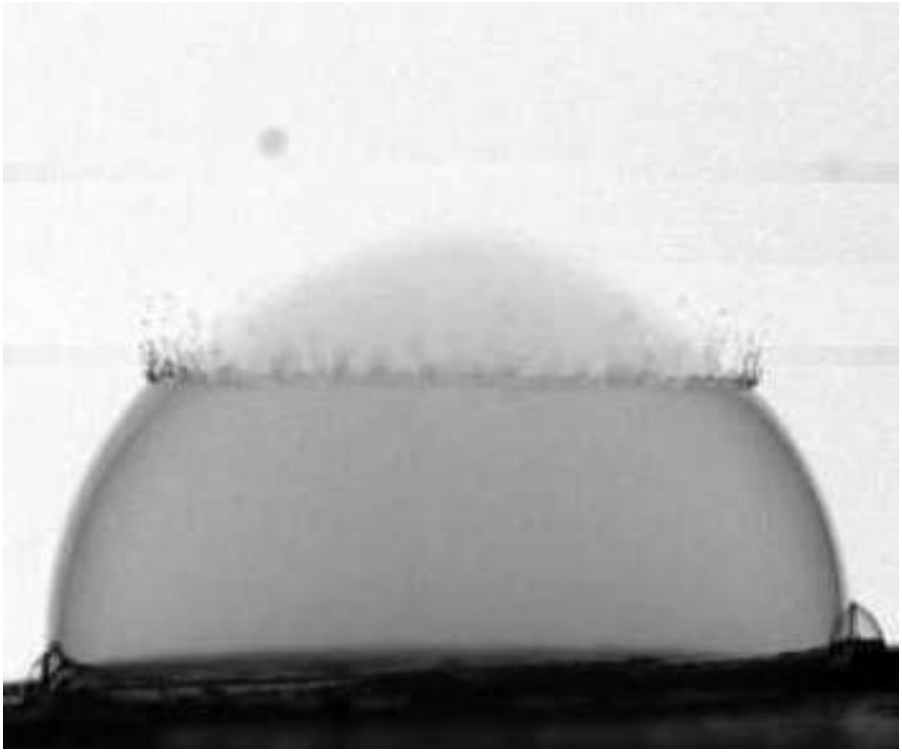

Fig A.1: Image of a rupturing bubble, captured using high-speed video at a frame rate of 67k fps. Glycerol vapour contained within bubble is revealed as the film ruptures.

We developed a non-invasive technique for measuring coarsening of foams and foam-fibre dispersions using the vibrational signal emitted by a bubble as it ruptures, see figure A.1. An advantage of this technique is that it can enable us to determine the optimal time to begin the drying process when producing lightweight fibrous materials. Impingement drying is a good example of a method that might benefit from this technique. It involves circulating warm air through a damp porous fibre network. Starting this process too soon, when bubbles are still present within the dispersion, can result in the structure collapsing (as some bubbles may still be supporting the fibres).

A.2 Background

If left undisturbed, most liquid films rupture as a result of the film thinning due to liquid drainage and/or evaporation [87, 122]. As the film becomes thinner, it is more prone to thermal fluctuations which can trigger its rupture [123]. The surface tension of a bubble's film is dynamic [124, 125]. The thinnest area of the film has a higher surface tension than other areas of the firm as the surfactant molecules try to restore the imbalance in the film's thickness. As a consequence, film rupture normally occurs at the point where the film is at its thinnest [126].

The rupture of a bubble film is a complex phenomenon, outside the scope of this thesis. Here, we are interested in the characteristic vibrational signal emitted by a bubble as it ruptures and how this can be related to the size of the bubble. There have been numerous studies which have analysed the acoustic emissions from bursting events [127–130]. The majority of these studies involved recording the pressure wave that propagates from the bubble as higher-pressure gas is released from the bubble as it ruptures. In one such study, Ding *et al.* reported detecting a precursor signal to the main bursting event (see figure A.2 h) [129]. They hypothesized that the signal

is the film oscillating prior to rupture as it becomes thinner. The increasing amplitude of the oscillations sets up an instability mechanism, triggering the bubble to eventually rupture. We observed a similar low amplitude signal while recording the bursting of liquid bubbles, however, we have attributed this to the tearing of the film as the tear propagates along the bubble's surface.

A.3 Method

The vibrational technique involves inserting a piezo electric pad (contact microphone) into a foam or foam-fibre dispersion, or placing an individual bubble onto the microphone's surface, depending on whether we are recording coarsening or a single rupture event (see figure A.2). The microphone is connected to a preamp (Art Dual tube preamp) to amplify the signal, created as a bubble ruptures. Using a laptop, the signal is then recorded at a sample rate of 48k per second using the audio analysis software, Audacity. Simultaneously, the rupture event is recorded using a high speed camera (Phantom vision v2010) at a frame rate of 67k fps. The signal and the high speed video are then analysed side by side.

A.4 Inferring a Bubble Size from the Vibrational Signature

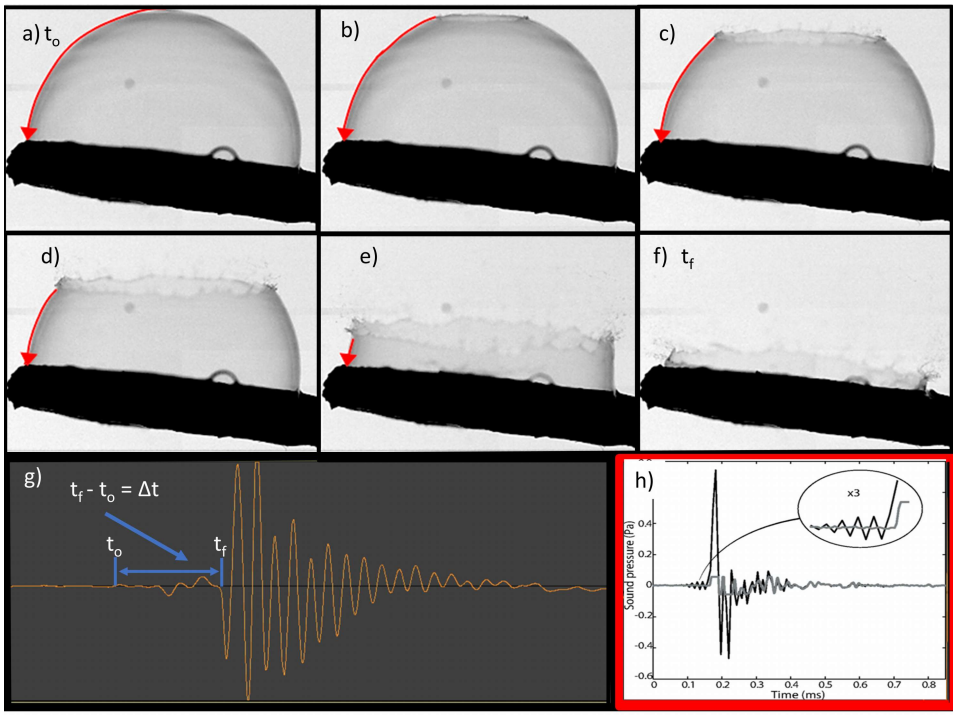

Fig A.2: (a to f) Image sequence from high speed camera of a bubble rupture. g) Δt shows the the low amplitude element of a bubble rupture that we have associated with film tearing. h) Acoustic burst signal captured by Ding *et al.*

Figure A.2 a to f shows a sequence of images of a single bubble as it ruptures. The bubble was placed on top of the microphone. The surfactant solution used to make the bubbles contained 1g of sodium dodecyl sulfite (SDS) per 100ml of water (above the CMC for SDS). The tear can be seen to propagate towards the microphone (direction of gravity). Figure A.2 g shows the typical signal associated with the rupture. The initial low amplitude part of the signal coincides with the tearing of the film as it propagates down towards the microphone. Δt is the time corresponding to the duration of the rupture. Figure A.2 h, shows the acoustic emission detected by Ding *et al.*, who reported it to be a precursor to the rupture of the film. Note the similarities between

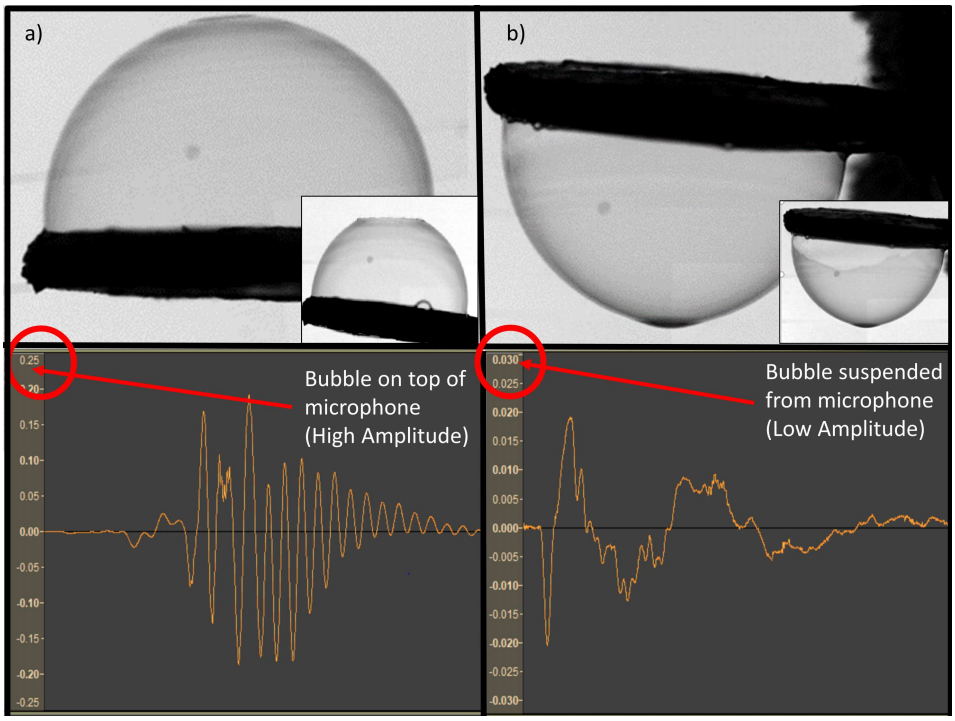

Fig A.3: a) bubble on top of contact microphone. b) bubble suspended from microphone. Both insets show the beginning of the ruptures. When placed on top of the microphone the rupture begins at the top of the bubble. When the bubble is suspended from the microphone, the rupture begins around the circumference of the bubble. The trace of the signal in (b) is completely different to (a) as no large droplets hit the microphone when the suspended bubble ruptures. The amplitude difference between (a) and (b) is an order of magnitude.

this acoustic signal obtained by Ding *et al.* and the vibrational signal that we captured.

The higher amplitude peaks (observed after Δt) are caused by water droplets, emitted from the rim of the bubble, hitting the microphone with enough momentum to trigger the piezo element. This was confirmed by analysing the high speed video recording of the rupture and comparing it to the microphone signal. We also carried out the same experiment, but with the bubble suspended from the underside of the microphone, see figure A.3. When the suspended bubble burst, there was no pattern of higher amplitude peaks observed. This is because the larger droplets fell away from the microphone,

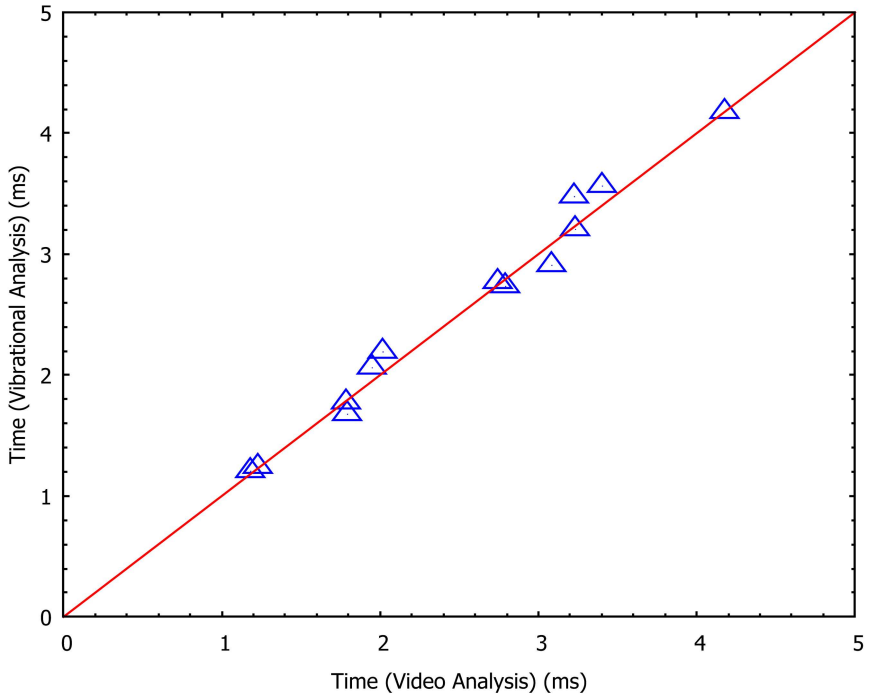

Fig A.4: The duration of 13 rupture events obtained using the audio software Audacity (y-axis) and taken from the high speed image analysis of the rupture (x-axis). This demonstrates that we can match the duration of the low amplitude response to the duration of the rupture obtained by video imaging.

rather than hitting it. The amplitude difference between figure A.3 a and b is an order of magnitude.

Figure A.4 shows the duration of thirteen rupture events captured by both high speed imaging and by recording the low amplitude response using the audio software Audacity. The durations of the initial low amplitude part of the vibrational signal are shown on the y-axis, while the x-axis shows the duration of the rupture obtained by counting the number of high speed camera images from the start of the rupture until it reached the microphone, then converting the frames to time. The linear slope is unity, showing that both methods give the same duration, demonstrating that the duration of the low amplitude response is equivalent to the rupture duration. We found the duration of the ruptures ranged from 1.2 to 4.2ms, while the bubble radius ranged from 7 to

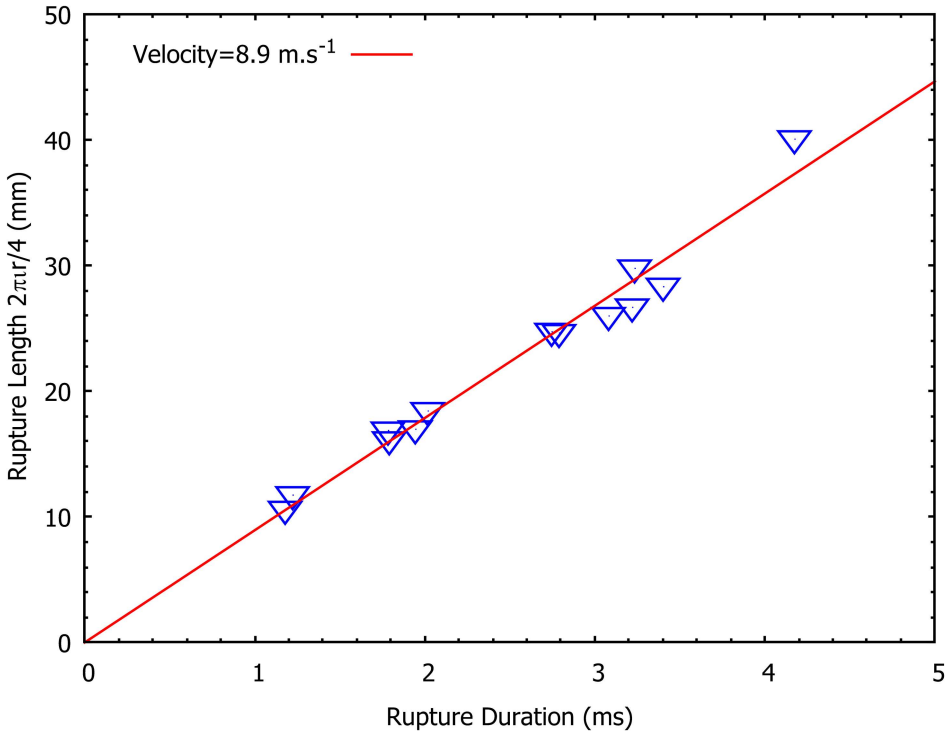

Fig A.5: Rupture length inferred from the images of the bubbles as a function of duration. The velocity of the ruptures were independent of bubble size and was calculated to be 8.9 $m.s^{-1}$.

$18mm$. The larger bubbles had the longest rupture duration.

Figure A.5 shows the velocity of the thirteen rupture events obtained by measuring the arc length of the bubble using the images from the high speed camera. We equated this distance to $\frac{1}{4}$ the circumference of the bubble (as the majority of the bubbles ruptured from the top towards the direction of the microphone). The duration of each event was obtained using the audio software, taken as the duration of the low amplitude response. The velocity of the ruptures, calculated as 8.9 $m.s^{-1}$, appeared to be independent of bubble size. We observed that it was almost constant, based on a range of different bubble sizes investigated.

Taylor and Cullick showed that the velocity U_v, of a thin liquid soap film during rupture is constant and can be expressed by [131, 132]

$$U_v = \sqrt{2\sigma/\rho h} \tag{A.1}$$

Where σ is the surface tension of the liquid, ρ is its density and h is the film's thickness.

The expression for the Taylor-Cullick velocity indicates that that the film's surface tension plays an important role in the velocity of the rupture. As the surface tension is increased, the velocity of the film rupture increases. We found this to hold true when we lowered the surfactant concentration and therefore increased the surface tension. The velocity of the ruptures shown in figure A.6 was $11.5 m.s^{-1}$, where the surfactant concentration was below the CMC.

To infer a bubble size from the duration of its low amplitude signal, we require the rupture velocity. While the high-speed camera works very well for single rupture events, it is not a practical solution to monitor foam-fibre dispersions over their long lifetimes. If the technique is to be utilized in a commercial or industrial application, then a better way to identify the velocity of the burst is required. A proposed solution to this problem is to first determine the average velocity of several individual bubble ruptures, made using the same surfactant solution, prior to generating the foam-fibre dispersion. A single image is all that is required to measure the radius of the bubble and infer the distance the rupture travels. The duration can be obtained (as before) using the vibrational technique. The velocity of several ruptures can now be averaged and used to determine the size of the bubbles from their vibrational responses.

To test our proposed solution, we made a comparison between the measured bubble size and the size inferred from the duration of individual rupture events. This time the surfactant concentration was *below* the CMC, at

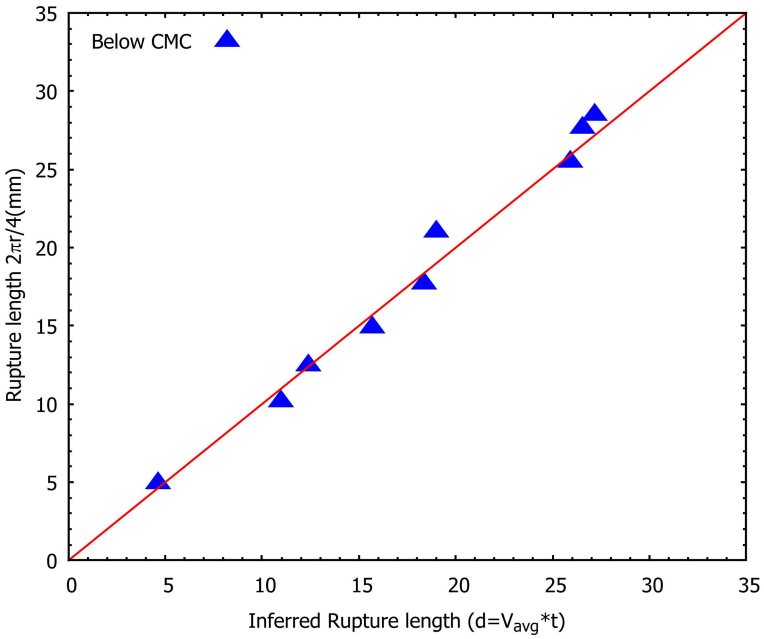

Fig A.6: The rupture length of the bubbles determined from high speed imaging is shown on the y-axis. The rupture length inferred from the duration of the vibrational response is shown on the x-axis. The surfactant solution of SDS was below the CMC at 0.1g/100ml.

0.1g/100ml. We placed the individual bubbles onto the microphone, taking a photograph of each and determined the radius of each bubble. Next, we calculated the average velocity of three ruptures using the duration of their respective vibrational responses, from which we inferred the radius of the remaining bubbles. Figure A.6 shows the measured rupture length (assuming all bubbles ruptured at the top of the hemisphere) on the y-axis, with the inferred rupture length on the x-axis. The inferred rupture length L, is given by

$$L = t_{rup}.V_{avg} \tag{A.2}$$

Where $V_{avg} = 11.5\ m.s^{-1}$, obtained from the first three bursts. t_{rup} is the duration of the low amplitude response. The higher velocity (compared to the bubbles in figure A.5) can be attributed to a higher surface tension as the bubbles were made using a surfactant solution below the CMC.

A.5 Monitoring the Coarsening Behaviour of Foam-fibre Dispersions

The microscope slide method (See Chapter 2) used to measure foam coarsening is an invasive one. Each time a measurement is required, a sample must be taken from within the dispersion. As foam-fibre dispersions have such long lifetimes, a large portion of the dispersion can end up being extracted for sampling. This is not ideal, particularly if we also want to create a fibrous structure from the dispersion.

Capturing the vibrational response of bubble ruptures within a dispersion offers a new and far less invasive way to monitor the coarsening behaviour of a foam or foam-fibre dispersion. We used our vibrational technique to capture the coarsening behaviour by monitoring the rupture events of a pure foam and two foam-fibre dispersions, where $\phi_i = 0.25$ and c= 0.5% and 2.5% respectively. The microphone was first suspended in the drainage vessel. We then poured the foam into the vessel, encompassing the piezo element. We recorded the full lifetime of the pure foam and for up to two hours for the foam-fibre dispersions. We measured the full duration of the bursts, and then took a moving average over 10% of each data set. This allowed us to smooth the data, as the polydispersity of the foam foam-fibre dispersions influenced the duration of their rupture lengths.

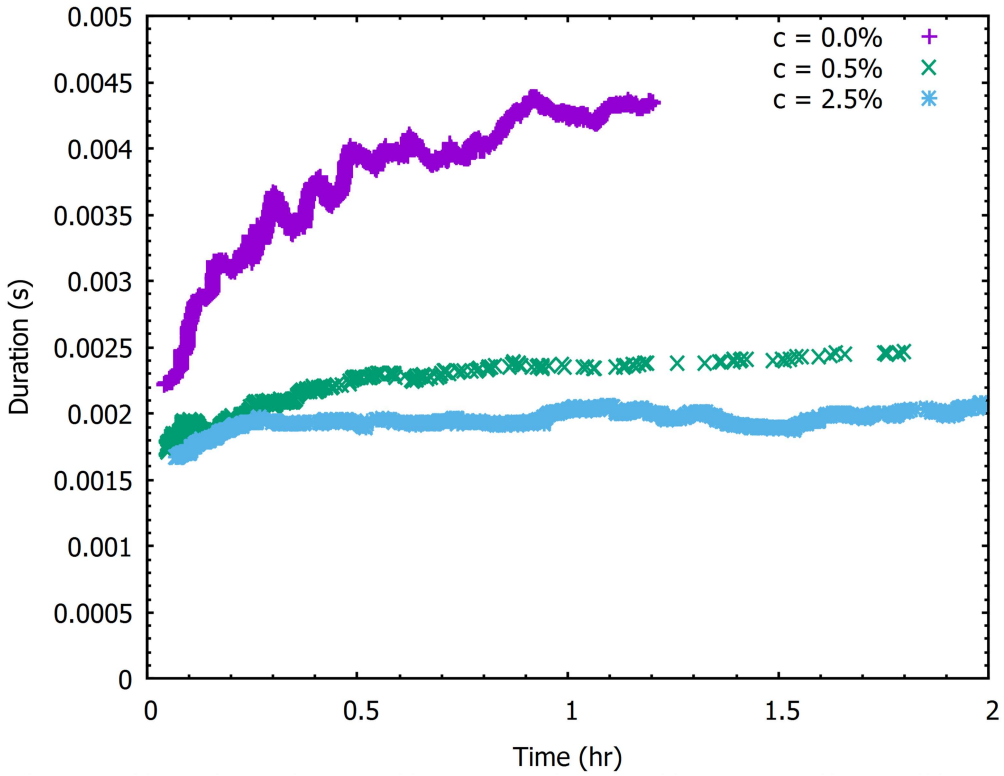

Fig A.7: The coarsening behaviour of a pure foam and two foam-fibre dispersions obtained by measuring the duration of the vibrational signatures of the ruptures as the microphone was suspended in the foam/foam-fibre dispersion. For the pure foam, the duration of the ruptures are seen to increase with time, reflecting the typical coarsening growth of the bubbles. The durations of the ruptures for the foam-fibre dispersions both feature a plateau, where bubble growth and hence duration of the bursts, are arrested by the presence of the fibres.

Figure A.7 shows the results of our coarsening experiment. For the pure foam, the duration of the ruptures increased with time, reflecting typical coarsening growth of bubbles in a pure foam. The durations of the ruptures for the foam-fibre dispersions both featured a plateau, where bubble growth and hence duration of the bursts, are arrested by the presence of the fibres.

A.6 Conclusion

We have presented a new technique, called the 'vibrational technique' to infer the size of a bubble using the vibrational signal emitted by a bubble as it ruptures. The technique can also be employed to monitor the coarsening behaviour of foams. It is particularly suited to monitor the coarsening of foam-fibre dispersions, where the acoustic emissions may be dampened by the presence of fibres. Unlike acoustic measurements, it allows us to detect the ruptures occurring within the dispersion and not just at the surface. Using this technique, we can determine when the bubbles within a dispersion have ceased rupturing. This can be used to identify the optimum time to begin the drying process. For instance, drying methods that circulate air through a porous structure, may cause the fibre network to collapse if the network is still being supported by the bubbles. Therefore, knowing when all the bubbles have ruptured will allow us to begin the drying process at the earliest possible time without collapsing the structure.

Appendix B

B.1 Impact of Bonding Agent and other Fibre Types

We made a number of lightweight samples using the foam-forming technique. To increase the mechanical strength of the material we added the bonding agent polyvinyl acetate (PVA) to the foam-fibre dispersions. We dissolved 15% PVA in a weight:weight ratio to the aqueous fibre dispersion, after the fibres had been dispersed. The percentage of PVA retained on the fibres was 20%, the remainder drained from the dispersion during the drainage phase. For comparison, we also made a sample with no PVA added (see figure 8.3). All foam-fibre dispersions had initial liquid fractions of 0.25 and each contained 3% Kraft fibres.

The addition of the bonding agent was seen to significantly increase the stress required to reach the same level of strain, where no bonding agent was present (see figure 8.2). The compressive modulus of the sample with the addition of PVA was 11.5kPa. This compared to 3.4kPa where no bonding agent was used.

We also carried out several tests on foam-formed fibrous structures made from CTMP, spent grain and peat fibres to establish how their compressive strengths compare to Kraft fibres.

We made samples from spent grain, a by-product of the brewing process. The spent grains came from the Guinness brewery in Dublin. We also used peat fibres, given to us by Bord na Mona, the state owned company set up to develop Irish peatlands. The peat fibres are a waste by-product from the production of their grow bags.

	Kraft	Peat f1	Peat f3	BSG	CTMP	PVA	Density ($kg.m^{-3}$)	E_c (kPa)
S1	10g					✓	34	11.5
S2					30g	✓	22	26
S3	10g	10g	10g			✓	76	40.5
S4	10g			30g		✓	69	42
S5	10g	30g				✓	77	130

Fig B.1: Composition of the five samples presented in figure 8.3. All samples contained polyvinyl acetate as a bonding agent. f1 and f3 are the fractions of peat contained within the samples, f1 being the smallest fractionation (fibres and particles with a width below 0.56mm) and f3 being the largest fraction (0.88-1.8mm).

The peat was fractionated by passing it through three sieves, having hole sizes of 0.56mm, 0.88mm and 1.8mm (corresponding to the edge length of the square holes in the sieves). Aside from the CTMP sample, we added 10g of Kraft fibres as well as PVA (15% PVA in the aqueous dispersions) to bond the materials together. Figure B.1 shows the composition of each sample, the samples are labeled S1 to S5. The addition of other fibre types increases E_c (compared to Kraft samples). Note the particularly high value of E_c (130kPa) for the sample including the smallest fraction of peat fibres.

Appendix C

C.1 OrientationJ analysis

The OrientationJ plugin computes the orientation, coherency and energy levels for each pixel within an image. The user specifies a window size, typically the width of the fibre or filament. A structure tensor for each pixel is built, from which the orientation, coherency and energy level of each pixel in the window are calculated. The structure tensor is a 2 x 2 matrix comprising of positive partial spatial derivatives of the image f(x,y). This is given by

$$J =< \nabla f, \nabla f^T >_w = \begin{bmatrix} < f_x, f_x >_w & < f_x, f_y >_w \\ < f_x, f_y >_w & < f_y, f_y >_w \end{bmatrix} \tag{C.1}$$

The energy level, E, is defined as the trace of the matrix.

$$E^2 = | < f_x, f_x >_w |^2 + | < f_y, f_y >_w |^2 \tag{C.2}$$

Coherency, C, is the ratio between the difference and the sum of the maximum and minimum eigenvalues, λ within the analysis window and is given by

$$C = \frac{\lambda_{max} - \lambda_{min}}{\lambda_{max} + \lambda_{min}} = \frac{\sqrt{(< f_y, f_y >_w - < f_x, f_x >_w)^2 + 4 < f_x, f_y >_w}}{< f_x, f_x >_w + < f_y, f_y >_w} \tag{C.3}$$

The plugin also computes a histogram of pixel orientations for the entire

image. The orientation θ of each pixel is calculated as

$$\theta = \frac{1}{2} arctan \left(2 \frac{< f_x, f_y >_w}{< f_y, f_y >_w - < f_x, f_x >_w} \right) \tag{C.4}$$

The energy level is used to identify image gradients. Low energy levels imply that there is little or no change in the gradient between the adjacent pixels, represented by the directional derivatives having constant values (such as the pixels on the fibre surface and not at the edge). To give a true representation of the distribution of fibre orientations, our analysis only included the orientation of pixels at edge of the fibres (higher energy levels). The lower energy pixels were excluded from the distributions by setting the minimum energy level at 3%, the same level as Rezakhaniha *et al.* in their analysis of the orientation distribution of collagen fibres [97].

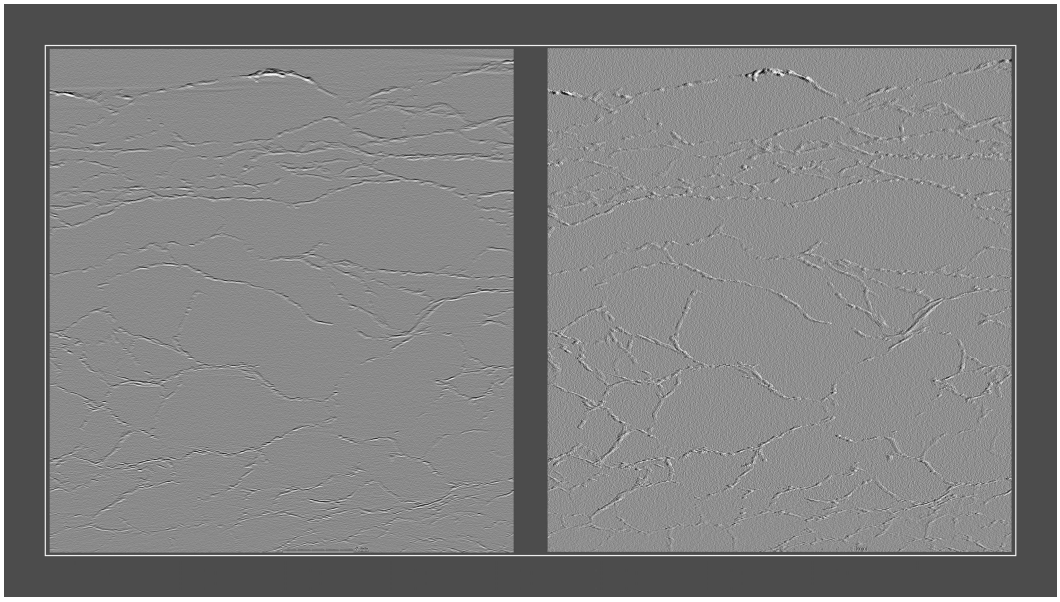

Fig C.1: OrientationJ's edge detection output of one of the images from the x-direction image stack. Each image represents a change in the gradients of the partial spatial derivates in both the x (left image) and y-directions (right image).

The analysed images also contained fibres orientating out of the image plane (appearing as small clusters of white pixels against a black background). Fibres projecting out of the plane have a low coherency level. We excluded

these fibres, and any noise present in the images from the analysis, by setting the minimum coherency level at 10%.

Bibliography

[1] B. Haffner, F. F. Dunne, S. R. Burke, and S Hutzler, *Ageing of fibre-laden aqueous foams*, Cellulose **24**, 231–239 (2016).

[2] S. Burke, M. Möbius, T. Hjelt, and S. Hutzler, *Properties of lightweight fibrous structures made by a novel foam forming technique*, Cellulose. **26**, 2529–2539 (2019).

[3] S. Burke, M. Möbius, T. Hjelt, J. Ketoja, and S. Hutzler, *Analysis of the foam-forming of non-woven lightweight fibrous materials using x-ray tomography*, SN Applied Sciences **192**, 10.1007/s42452-021-04172-9 (2021).

[4] A. Mughal, S. Cox, D Weaire, S. Burke, and S. Hutzler, *Demonstration and interpretation of 'scutoid' cells formed in a quasi-2d soap froth*, Philosophical Magazine Letters **98**, 358–364 (2018).

[5] D. Attenborough, *Blue planet ii, episode 7* (BBC, 2017).

[6] H. Chesbrough, M. Bogers, R. Strand, and E. Whalen, *Sustainability through open innovation: carlsberg and the green fiber bottle.* In SAGE Business Cases, 10.4135/9781526491268 (2020).

[7] *Edible six-pack rings*, (2018) https://packagingeurope.com/corona/.

[8] *Cnn buisness news*, (2020) https://edition.cnn.com/2019/10/10/business/carlsbergpaperbeerbottles/index.html.

[9] *Saltwater brewery*, (2019) https://www.theguardian.com/sustainable-business/2016/may/29/florida-brewery/creates/edible/beer/holders/save/marine/life/saltwater.

[10] B. Radvan and A. Gatward, *The formation of wet-laid webs by a foaming process*, Tappi **55**, 748–751 (1972).

[11] T. Lappalainen, K. Salminen, K. Kinnunen, M. Järvinen, I. Mira, and M. Andersson, *Foam forming revisited. part ii. effect of surfactant on the properties of foam-formed paper products*, Nordic Pulp and Paper Research Journal **29**, 689–699 (2014).

[12] J. Lehmonen, P. Jetsu, K. Kinnunen, and T. Hjelt, *Potential of foam-laid forming technology in paper applications*, Nordic Pulp and Paper Research Journal **28**, 392–398 (2013).

[13] K. Kinnunen, J. Lehmonen, N. Beletski, P. Jetsu, and T. Hjelt., *Benefits of foam forming technology and its application in high mfc addition structures.* Advances in Pulp and Paper Research, 837–850 (2013).

[14] M. Lecourt, T. Pöhler, J. Hornatowska, L. Salmén, and P. Jetsu, *Density profiles of novel kraft pulp and tmp based foam formed thermal insulation materials observed by x-ray tomography and densitometry*, Holzforschung **72**, 397–403 (2018).

[15] A. Madani, S. Zeinoddini, S. Varahmi, H. Turnbull, A. B. Phillion, J. A. Olson, and D. M. Martinez, *Ultra-lightweight paper foams: processing and properties*, Cellulose. **21**, 2023–2031 (2014).

[16] J. Ketoja, S. Paunonen, P. Jetsu, and E. Pääkkönen, *Compression strength mechanisms of low-density fibrous materials*, Materials. **12**, 10.3390/ma12030384 (2019).

[17] T. Pöhler, P. Jetsu, A. Fougerón, and V. Barraud, *Use of papermaking pulps in foam-formed thermal insulation materials*, Nordic Pulp and Paper Research Journal **32**, 367–374 (2017).

[18] F. Domínguez-Muñoz, B. Anderson, J. M. Cejudo-López, and A Carrillo-Andrés, *Uncertainty in the thermal conductivity of insulation materials*, Energy and Buildings **42**, 2159–2168 (2010).

[19] J. Francl and W. Kingery, *Thermal conductivity: ix, experimental investigation of effect of porosity on thermal conductivity.* Journal of the American Ceramic Society **37**, 99–107 (1954).

[20] T. Pöhler, J. A. Ketoja, T. Lappalainen, V. Luukkainen, I. Nurminen, P. Lahtinen, and K. Torvinen, *On the strength improvement of lightweight fibre networks by polymers, fibrils and fines*, Cellulose, `10.1007/s10570-020-03263-x` (2020).

[21] S. Paunonen, O. Timofeev, K. Torvinen, T. Turpeinen, and J. A. Ketoja, *Improving compression recovery of foam-formed fiber materials*, BioRes. **13**, 4058–4074 (2018).

[22] E. 13501-1, *Fire classification of construction products*, 2018.

[23] O. Köklükaya, F. Carosio, J. C. Grunlan, and L. Wågberg, *Flame-retardant paper from wood fibers functionalized via layer-by-layer assembly*, ACS Applied Materials and Interfaces **7**, 23750–23759 (2015).

[24] A. Ottenhall, J. Illergård, and M. Ek, *Water purification using functionalized cellulosic fibers with nonleaching bacteria adsorbing properties.* Environmental Science and Technology **51**, 7616–7623 (2017).

[25] K. C. Payne, C. D. Jackson, C. E. Aizpurua, O. J. Rojas, and M. A Hubbe, *Oil spills abatement: factors affecting oil uptake by cellulosic fibers.* Environmental Science and Technology. **46**, 7725–7730 (2012).

[26] S. Cao, T. Dong, G. Xu, and F Wang, *Oil spills abatement: factors affecting oil uptake by cellulosic fibers.* Journal of Natural Fibers **14**, 727–735 (2017).

[27] D. Weaire and S. Hutzler, *The physics of foams* (Clarendon press, Oxford, 1999).

[28] I. Cantat, S. Cohen-Addad, F. Elias, F. Graner, R. Ho¨hler, R. Flatman, O. Pitois, F. Rouyer, and A Saint-Jalmes, *Foams:structure and dynamics* (Oxford University Press, Oxford, 2013).

[29] R. Shih, D. Bardin, T. D. Martz, P. S. Sheeran, P. A. Dayton, and A. P Lee, *Flow-focusing regimes for accelerated production of monodisperse drug-loadable microbubbles toward clinical-scale applications*, Lab Chip **13**, 4816 (2013).

[30] W. Hanselmann and E. Windhab, *Flow characteristics and modelling of foam generation in a continuous rotor/stator mixer*, Journal of Food Engineering **38**, 393–405 (1998).

[31] K. I. Khristov, D. R. Exerowa, and P. M. Krugljakov, *Influence of the type of foam films and the type of surfactant on foam stability.* Colloid and Polymer Science **261**, 265–270 (1983).

[32] M. Rosen and J. Kunjappu, *Surfactants and interfacial phenomena* (Wiley, 2012).

[33] T. Tadros, *Critical micelle concentration.* Encyclopedia of Colloid and Interface Science, 209–210 (2013).

[34] P. Walstra, *Principles of foam formation and stability*, Springer Series in Applied Biology., 1–15 (1989).

[35] J. S. Lioumbas, E. Georgiou, M. Kostoglou, and T. D. Karapantsios, *Foam free drainage and bubbles size for surfactant concentrations below*

the cmc, Colloids and Surfaces A: Physicochemical and Engineering Aspects **487**, 92–103 (2015).

[36] N. Denkov, S. Tcholakova, K. Golemanov, K. Ananthpadmanabhan, and A. Lips, *The role of surfactant type and bubble surface mobility in foam rheology*, Soft Matter **5**, 3389–3408 (2009).

[37] W. Drenckhan and S. Hutzler, *Structure and energy of liquid foams.* Advances in Colloid and Interface Science **224**, 1–16 (2015).

[38] L. L. Schramm and F. Wassmuth, "Foams: basic principles", in *Foams: fundamentals and applications in the petroleum industry* () Chap. 1, pp. 3–45.

[39] R. Farajzadeh, S. Vincent-Bonnieu, and N. Bourada Bourada, *Effect of gas permeability and solubility on foam*, Journal of Soft Matter, 1–7 (2014).

[40] D. Langevin, *Aqueous foams and foam films stabilised by surfactants. gravity-free studies*, Comptes Rendus Mécanique **345**, 47 –55 (2017).

[41] M. Vera and D. Durian, *Enhanced drainage and coarsening in aqueous foams.* Phys Rev Lett. **88**, 10.1103/PhysRevLett.88.088304 (2002).

[42] J. Glazier and D. Weaire, *The kinetics of cellular patterns*, Journal of Physics: Condensed Matter **4**, 1867 (1999).

[43] S. A. Magrabi, B. Z. Dlugogorski, and G. J. Jameson, *Bubble size distribution and coarsening of aqueous foams*, Chemical Engineering Science **58**, 4007–4022 (1999).

[44] B. S. Gardiner, B. Z. Dlugogorski, and G. J. Jameson, *Coarsening of two- and three-dimensional wet polydisperse foams*, Philosophical Magazine A **80**, 981–1000 (2000).

[45] K. Giribabu and P. Ghosh, *Binary coalescence of air bubbles in viscous liquids in presence of non-ionic surfactant*, The Canadian Journal of Chemical Engineering **86**, 643–650 (2008).

[46] P. Ghosh and V. A. Juvekar, *Analysis of the drop rest phenomenon.* Chemical Engineering Research and Design **7**, 715–728 (2002).

[47] F. Garcı´a-Moreno, S. Tobin, M. Mukherjee, C. Jime´nez, E. Solo´rzano, G. Kumar, S. Hutzler, and J Banhart, *Analysis of liquid metal foams through x-ray radioscopy and microgravity experiments.* Soft Matter **10**, 6955–6962 (2014).

[48] K. A. Verbist G Weaire D, *The foam drainage equation.* Condensed Matter **8**, 3715 (1996).

[49] G. Verbist, D. Weaire, and A. Kraynik, *The foam drainage equation*, Journal of Physics: Condensed Matter. **8**, 3715–3731 (1996).

[50] I Cantat, N Kern, and R Delannay, *Dissipation in foam flowing through narrow channels*, Europhysics Letters (EPL) **65**, 726–732 (2004).

[51] I. I. processing and analysis in Java, (2019) `https://imagej.nih.gov/ij/`.

[52] W. Drenckhan and S. Hutzler, *Structure and energy of liquid foams.* Advances in Colloid and Interface Science, 224 (2015).

[53] H. J. O. Pinho, D. M. R. Mateus, and S. S. Alves, *Probability density functions for bubble size distribution in air–water systems in stirred tanks*, Chemical Engineering Communications **205**, 1105–1118 (2018).

[54] R. Parthasarathy and N. Ahmed, *Size distribution of bubbles generated by fine-pore spargers*, Journal of Chemical Engineering of Japan **29**, 1030–1034 (1996).

[55] A. M. Al-Qararah, T. Hjelt, A. Koponen, A. Harlin, and J. A. Ketoja, *Bubble size and air content of wet fibre foams in axial mixing with macro-instabilities*, Colloids and Surfaces A: Physicochemical and Engineering Aspects **436**, 1130–1139 (2013).

[56] A. M Al-Qararah, T Hjelt, A Koponen, A Harlin, and J. A Ketoja, *Bubble size and air content of wet fibre foams in axial mixing with macro-instabilities*, Colloids and Surfaces A: Physicochemical and Engineering Aspects **436**, 1130–1139 (2013).

[57] S. Cohen-Addad, R. Höhler, and O. Pitois, *Flow in foams and flowing foams.* Annual Review of Fluid Mechanics **45**, 241–267 (2013).

[58] M. E. Möbius, G. Katgert, and M. van Hecke, *Relaxation and flow in linearly sheared two-dimensional foams.* Europhysics Letters **90**, 44003 (2010).

[59] M. Bobert, H. Persson, and B. Persson, *Foam concentrates: viscosity and flow characteristics.* Fire Technology **33**, 336–355 (1997).

[60] M. B. Sexton, M. E. Möbius, and S. Hutzler, *Bubble dynamics and rheology in sheared two-dimensional foams.* Soft Matter **7**, 11252 (2011).

[61] P. Saramito, *A new elastoviscoplastic model based on the herschel–bulkley viscoplastic model*, Journal of Non-Newtonian Fluid Mechanics **158**, 154–161 (2009).

[62] U. Hirn and R Schennach, *Comprehensive analysis of individual pulp fiber bonds quantifies the mechanisms of fiber bonding in paper.* Sci Rep . **5** (2015).

[63] Y. Gao, Q. Li, Y. Shi, and R. Cha, *Preparation and application of cationic modified cellulose fibrils as a papermaking additive*, International Journal of Polymer Science, 1–8 (2016).

[64] C. J Biermann, *Handbook of pulping and papermaking*, Academic Press **San Diego** (1996).

[65] K. K. Pandey, *A study of chemical structure of soft and hardwood and wood polymers by ftir spectroscopy*, Journal of Applied Polymer Science. **71**, 1969–1975 (1999).

[66] E. Sjostrom., *Wood chemistry*, (2013).

[67] J. E Winandy and R. M Rowell, *The chemistry of wood strength*, Advances in Chemistry **207**, 211–255 (1984).

[68] Z Shao and K Li, *The effect of fiber surface lignin on interfiber bonding*, Journal of Wood Chemistry and Technology **26**, 231–244 (2006).

[69] E Afra, H Yousefi, M. M Hadilam, and T. Nishino, *Comparative effect of mechanical beating and nanofibrillation of cellulose on paper properties made from bagasse and softwood pulps.* Carbohydrate Polymers **97**, 725–730 (2013).

[70] F. J Schmied, C Teichert, L Kappel, U Hirn, W Bauer, and R Schennach, *What holds paper together: nanometre scale exploration of bonding between paper fibres*, Scientific Reports **3**, 10.1038/srep02432 (2013).

[71] A Robertson, *The physical properties of wet webs*, TAPPI **42**, 969–978 (1959).

[72] D. Williams, *A fiber network model theory for the wet web strength of paper*, TAPPI **66**, 159–162 (1983).

[73] A Tejado and T. G. M van de Ven, *Why does paper get stronger as it dries?*, Materials Today **13**, 42–49 (2010).

[74] N Klinga, H. Hoeglund, and C Sandberg, *Energy efficient high quality ctmp for paperboard*, Materials Science (2007).

[75] C Sandberg, J Hill, and M Jackson, *On the development of the refiner mechanical pulping process – a review*, Nordic Pulp and Paper Research Journal, 10.1515/npprj-2019-0083 (2020).

[76] H. R Motamedian, A. E Halilovic, and A Kulachenko, *Mechanisms of strength and stiffness improvement of paper after pfi refining with a focus on the effect of fines*, Cellulose **26**, 4099–4124 (2019).

[77] Y Li and X.-Q. Dai, *Biomechanical engineering of textiles and clothing* (Woodhead Publishing, 2006).

[78] A Madani, S Zeinoddini, S Varahmi, H Turnbull, A Phillion, J Olson, and D Martinez, *Ultra-lightweight paper foams: processing and properties*, Cellulose **21**, 2023–2031 (2014).

[79] T Mäkinen, J Koivisto, E Pääkkönen, J. A Ketoja, and M. J Alava, *Crossover from mean-field compression to collective phenomena in low-density foam-formed fiber material*, Soft Matter, 10.1039/d0sm00286k (2020).

[80] A. M AlQararah, A Ekman, T Hjelt, H Kiiskinen, J Timonen, and J. A Ketoja, *Porous structure of fibre networks formed by a foaming process: a comparative study of different characterization techniques*, Journal of Microscopy **264**, 88–101 (2016).

[81] I Mira, M Andersson, L Boge, I Blute, G Carlsson, K Salminen, T Lappalainen, and K Kinnunen, *Foam forming revisited part i. foaming behaviour of fibre-surfactant systems*, Nordic Pulp and Paper Research Journal **29**, 679–688 (2014).

[82] A. M Al-Qararah, T Hjelt, K Kinnunen, N Beletski, and J Ketoja, *Exceptional pore size distribution in foam-formed fibre networks*, Nordic Pulp and Paper Research Journal **27**, 226–230 (2012).

[83] T Lappalainen, K Salminen, K Kinnunen, M Järvinen, I Mira, and M Andersson, *Foam forming revisited. part ii. effect of surfactant on the properties of foam-formed paper products*, Nordic Pulp and Paper Research Journal **29**, 689–699 (2014).

[84] A. Jäsberg, P. Selenius, and A Koponen, *Experimental results on the flow rheology of fiber-laden aqueous foams*, Colloids and Surfaces A: Physicochemical and Engineering Aspects **473**, 147–155 (2015).

[85] A Jäsberg, P Selenius, and A Koponen, *The effect of fibrous materials on the rheology of aqueous foams*, Advances in Pulp and Paper Research, 159–173 (2018).

[86] Q Hou and X Wang, *Effect of fiber surface characteristics on foam properties*, Cellulose **26**, 3315–3325 (2018).

[87] D Weaire and S Hutzler, *Foam as a complex system*, Journal of Physics: Condensed Matter **21** (2009).

[88] O Timofeev, P Jetsu, H Kiiskinen, and J. T Keränen, *Drying of foam-formed mats from virgin pine fibers*, Drying Technology **34**, 1210–1218 (2015).

[89] K. O and S. J, *Coarsening of two-dimensional soap froths in the presence of pinning centers.* Phys Rev B **46**, 10579–10582 (1992).

[90] J. A Ketoja, S Paunonen, P Jetsu, and E Pääkkönen, *Compression strength mechanisms of low-density fibrous materials*, Materials (Basel, Switzerland) **12**, 384 (2019).

[91] C. M. van Wyk, *20—note on the compressibility of wool*, Journal of the Textile Institute Transactions **37**, T285–T292 (1946).

[92] T. Komori and K. Makishima, *Numbers of fiber-to-fiber contacts in general fiber assemblies*, Textile Research Journal **47**, 13–17 (1977).

[93] A Garner and T. Heindel, *The effect of fibre type on bubble size*, pulp and paper science **26** (2000).

[94] A Boyde, F. McCorkell, G. Taylor, R. Bomphrey, and M Doube, *Iodine vapor staining for atomic number contrast in backscattered electron and x-ray imaging*, Microsc. Res Tech **77**, 1044–1051 (2014).

[95] R. manual, *Volume graphics gmbh, vg studio max 2.2*, Heidelberg (2013).

[96] T. Ridler and S. Calvard, *Picture thresholding using an iterative selection method*, IEEE Transactions on Systems, Man, and Cybernetics **8**, 630–632 (1978).

[97] R. Rezakhaniha, A. Agianniotis, J. Schrauwen, A. Griffa, D. Sage, C. Bouten, F. van de Vosse, M. Unser, and N Stergiopulos, *Experimental investigation of collagen waviness and orientation in the arterial adventitia using confocal laser scanning microscop*, Biomechanics and Modeling in Mechanobiology **11**, 461–473 (2011).

[98] X Liang, J Shin, D Magagnosc, Y Jiang, S. Park, J. A Hart, K Turner, D. Gianola, and P. Purohit, *Compression and recovery of carbon nanotube forests described as a phase transition*, International Journal of Solids and Structures **122-123**, 196–209 (2017).

[99] *Irsih brewers association*, (2019) `http://www.abfi.ie/iba`.

[100] D. I. IBEC, (2019) `https://www.abfi.ie/Sectors`.

[101] P. Forssell, H. Kontkanen, H. Schols, S. Hinz, V. Eijsink, J. Treimo, J. Robertson, K. Waldron, C. Faulds, and J. Buchert, *Hydrolysis of brewers' spent grain by carbohydrate degrading enzymes*, J I Brewing **114**, 306–314 (2008).

[102] A. M. Al-Qararah, T. Hjelt, A. Koponen, A. Harlin, and J. A. Ketoja, *Response of wet foam to fibre mixing.* Colloids and Surfaces A: Physicochemical and Engineering Aspects **467**, 97–106 (2015).

[103] S. Aliyu and M. Bala, *Brewer's spent grain: a review of its potentials and applications*, African Journal of Biotechnology **10**, 324–331 (2011).

[104] S. I. Mussatto, G. Dragone, and I. C. Roberto, *Brewers' spent grain: generation, characteristics and potential applications.* Journal of Cereal Science **43**, 1–14 (2006).

[105] G. Mandalari, C. B. Faulds, A. I. Sancho, A. Saija, G. Bisignano, R. LoCurto, and K. W. Waldron, *Fractionation and characterisation of arabinoxylans from brewers' spent grain and wheat bran*, Journal of Cereal Science **42**, 205 –212 (2005).

[106] C. D. Stalikas, *Extraction, separation, and detection methods for phenolic acids and flavonoids*, Journal of Separation Science **30**, 3268–3295 (2007).

[107] M. Bonoli, E. Marconi, and M. F. Caboni, *Free and bound phenolic compounds in barley (hordeum vulgare l.) flours: evaluation of the extraction capability of different solvent mixtures and pressurized liquid methods by micellar electrokinetic chromatography and spectrophotometry*, Journal of Chromatography A **1057**, 1 –12 (2004).

[108] A. McCarthy, Y. O'Callaghan, C. A., C. Piggott, R. Fitzgerald, and O. N.M., *Phenolic extracts of brewers' spent grain (bsg) as functional ingredients - assessment of their dna protective effect against oxidant-induced dna single strand breaks in u937 cells.* Food Chem. **134**, 641–646 (2012).

[109] W. Chang, C. Hsieh, M. Hsiao, W. Lin, Y. Hung, and J. Ye, *Caffeic acid induces apoptosis in human cervical cancer cells through the mitochondrial pathway*, Taiwan J Obstet Gynecol **49**, 419–424 (2010).

[110] S. Sakai, H. Ochiai, K. Nakajima, and K. Terasawa, *Inhibitory effect of ferulic acid on macrophage inflammatory protein-2 production in a murine macrophage cell line*, Cytokinel **9**, 242–248 (1997).

[111] S. Ikram, L. Huang, H. Zhang, J. Wang, and M. Yin, *Composition and nutrient value proposition of brewers spent grain.* Journal of Food Science **82**, 2232–3342 (2017).

[112] P. Alonso-Riano, M. Sanz Diez, B. Blanco, S. Beltran, E. Trigueros, and O Benito-Roman, *Water ultrasound-assisted extraction of polyphenol compounds from brewer's spent grain: kinetic study, extract characterization, and concentration*, Antioxidants (Basel) **9**, 265 (2020).

[113] R Lucs, *Ueber das zeitgesetz des kapillaren aufstiegs von flussigkeitenr*, Kolloid Z. **23**, 10.1007/bf01461107. (1918).

[114] E. Washburn, *The dynamics of capillary flow*, Physical Reviewr **17**, 273 (1921).

[115] A. Hamraoui and T. Nylander, *Analytical approach for the lucas–washburn equation*, Journal of Colloid and Interface Science **250**, 415–421 (2002).

[116] B. M. Cummins, R. Chinthapatla, F. S. Ligler, and G. M Walker, *Time-dependent model for fluid flow in porous materials with multiple pore sizes*, Analytical Chemistry **89**, 4377–4381 (2017).

[117] *Tappi t 441 cobb test*, (2013) https://ipstesting.com/find-a-test/tappi-test-methods/tappi-t-441-cobb-test/.

[118] P. Recycling, (2020) http://wastematters.ie/polystyrene-recycling/.

[119] J. Y. Keränen and E. Retulainen, *Changing quality of recycled fiber material. part 1. factors affecting the quality and an approach for characterisation of the strength potential*, BioRes **11**, 10404–10418 (2016).

[120] J. Necas and L. Bartosikova, *Carrageenan: a review*, Veterinarni Medicina **58**, 187–205 (2013).

[121] T. Rydzkowski, K. Reszka, M. Szczypiński, M. M. Szczypiński, E. Kopczyńska, and V. K. Thakur, *Manufacturing and evaluation of mechanical, morphological, and thermal properties of reduced graphene oxide-reinforced expanded polystyrene (eps) nanocomposites.* Advances in Polymer Technology, 1–9 (2020).

[122] L Champougny, J Miguet, R Henaff, F Restagno, F Boulogne, and E Rio, *Influence of evaporation on soap film rupture*, Langmuir. **34**, 3221–3227 (2018).

[123] J Rijnbout, W Donners, and A. Vrij, *Light scattering from soap films*, Nature **249**, 10.1038/249242b0 (1974).

[124] E. I Franses, O. A Basaran, and C.-H Chang, *Techniques to measure dynamic surface tension*, Colloid and Interface Science **1**, 296–303 (1996).

[125] R Defay and G Petre, *Dynamic surface tension*, Surface and Colloid Science **3**, 25–81 (1971).

[126] V. V Yaminsky, S Ohnishi, E. A Vogler, and R. G Horn, *Stability of aqueous films between bubbles. part 1. the effect of speed on bubble coalescence in purified water and simple electrolyte solutions*, Langmuir **26**, 8061–8074 (2010).

[127] V Vidal, J.-C Géminard, T Divoux, and F Melo, *Acoustic signal associated with the bursting of a soap film which initially closes an overpressurized cavity*, The European Physical Journal B **54**, 321–339 (2006).

[128] G. B Deane and H Czerski, *A mechanism stimulating sound production from air bubbles released from a nozzle*, The Journal of the Acoustical Society of America. **123**, 126–132 (2008).

[129] J Ding, F. W Tsaur, A Lips, and A Akay, *Acoustical observation of bubble oscillations induced by bubble popping*, Physical Review E **75**, 10.1103/physreve.75.041601 (2007).

[130] T Divoux, V Vidal, F Melo, and J.-C Géminard, *Acoustic emission associated with the bursting of a gas bubble at the free surface of a non-newtonian fluid*, Physical Review E **77**, doi:10.1103/physreve.77.056310 (2008).

[131] G. I. Taylor, *The dynamics of thin sheets of fluid iii. disintegration of fluid sheet*, Proc. Roy. Soc. London A **253**, 313 (1959).

[132] F. E. C. Cullick, *Comments on a ruptured soap film*, Journal of Applied Physics. **31**, 1128 (1960).